STRUCTURAL DESIGN OPTIMIZATION OF ELECTRIC MOTORS TO IMPROVE TORQUE PERFORMANCE

by

Jaewook Lee

A dissertation submitted in partial fulfillment
of the requirements for the degree of
Doctor of Philosophy
(Mechanical Engineering)
in The University of Michigan
2010

Doctoral Committee:

Professor Noboru Kikuchi, Chair
Professor Kamal Sarabandi
Associate Professor Kazuhiro Saitou
Research Scientist Zheng-Dong Ma

To my wife, son, and family

ACKNOWLEDGEMENTS

I would like to express the deepest appreciation to my advisor, Professor Noboru Kikuchi for his kind guidance and encouragement during my doctoral studies at the University of Michigan. He has given me priceless opportunity and directed me for a better way. I also would like to sincerely acknowledge the helpful suggestions and criticisms made by my doctoral committee members, Professor Kamal Sarabandi, Professor Kazu Saitou and Dr. Zheng-Dong Ma.

I would like to express my gratitude to Professor Yoon Young Kim, Professor Jeonghoon Yoo, and Professor Seungjae Min, for their guidance and advice in my research.

I wish to express my special thanks to Dr. Jeong Hun Seo, who introduced me to Prof. Kikuchi, for his kindness and friendship. I am also indebted to my colleagues at the Computational Mechanics Laboratory, Kyungjun Lee, Dr. Youngwon Hahn, Dr. Geunsoo Ryu, Dr. Ikjoong Lee, Dr. Jangho Shin, and Dr. Tsuyoshi Higo.

I also would like to thank to my colleagues and friends at the University of Michigan: Dr. Se-hyun Ahn, Dr. Jong-hyun Park, Jaewook Oh, Dae-hyun Kim, Dr. Taemin Earmme, Joong-han Shin, Chan Yoon, Seung-jun Lee, Jae-won Lee, Dr. Jong-hun Lee, You-keun

Oh, Gi-suk Hwang, Kwan-chul Lee, Dong-jin Hyun, Hong-rae Park, Dr. Sun Yi, Dr. Il Yeo, Dr. Myoung-do Chung, Seung-hwan Lee, Seung-chul Yang, Ayoung Kim

My special thanks are expressed to Dr. Peter Nagourney and Dr. Roann Altman for their tutoring in writing.

Finally, I am very grateful to my parents, and brother, and also my wife Jinah for their continuous patience, support and encouragement during my doctoral studies at the University of Michigan.

TABLE OF CONTENTS

LIST OF FIGURES

LIST OF TABLES

ABSTRACT

The goal of this research is to investigate an approach to find the optimal geometry of electric motors for the enhancement of force/torque performance. To predict the magnetic force/torque of electric motors having complex structure, the finite element method for magnetostatic analysis is extensively investigated. The finite element formulations for two/three dimensional problems using nodal/edge elements and for non-linear problems with Newton-Raphson iteration, are described in detail. Numerical examples show that the finite element method yields reasonable magnetic field solutions in all situations. From the obtained magnetic field, the magnetic force/torque can be calculated using various methods: Maxwell stress tensor method, virtual work method, equivalent source method, body force calculation method using the virtual air-gap scheme. Their formulations are briefly derived for both linear and non-linear problems. The observation of force calculation results confirms that total magnetic force is consistent regardless of calculation methods, but local force distribution depends on calculation methods.

The structural topology optimization approach is applied to find optimal geometries in magnetic field problems. As a basic study, two optimization examples are presented. The first example aims to examine the properties of a magnetic circuit with respect to the

force/torque performance. The design results show that non-linear permeability makes the optimal structure simple and concentrated. In addition, the effect of mass on the total force/torque is also discussed. In the second example, the structural topology optimization is employed in a coupled magneto-structural problem. The mechanical compliance caused by the distributed local magnetic force is minimized when maximizing the global magnetic force. The design results reveal that different force distributions, depending on calculation method, result in the completely different optimal geometry in the magneto-structural problem.

As a practical application, switched reluctance motors are designed using structural topology optimization. The design goal is to minimize torque ripple under the constrained current. To represent motor performance in a steady-state operation explicitly, the mathematical analysis model is newly developed. Magnetic characteristics are modeled using the finite element method and interpolation functions. Then, the current curve is calculated by solving the circuit equation, and the torque profile is obtained from the global virtual work method. Using the sequential linear programming method, the rotor/stator shape and voltage on-off angles are designed to improve torque performance. Two/three dimensional designs in the linear **B-H** relation and the design considering the nonlinearity due to magnetic saturation are presented.

CHAPTER 1
INTRODUCTION

1.1. Motivation and goal

Electric motors are a fundamental component in almost all industries. It is known that electric motors consume about 60% of the electrical energy produced in industrialize nations [1]. Recently, electric motors have attracted more attention as automakers prepare for the mass production of electric vehicles. Despite a long history of research on electric motors, there still remains room to enhance the motor performance. As noted by Mitsuhiko Yamashita, Executive Vice President of Nissan Motor Co., Ltd [2] , "Motor technology is very old. There has been no big progress recently because people didn't pay much attention to motor technology".

This research presents an approach to find the optimal geometry for improving performance of electric motors. The performance of electric motors can be improved by two ways: a) by changing their geometry, and/or b) by modifying their control scheme. Contrary to a vigorous research effort on control optimization, more research to find the optimal geometry remains. In this research, we aim to fully investigate a structural topology optimization approach to magnetic fields, which can identify ways to change

the geometry of high performance electric motors. Among various motor performances, we mainly focus on the force/torque density which can be enhanced by maximizing the force/torque with the minimum amount of mass. The magnetic force/toque is calculated numerically using the finite element method with various calculation methods. To investigate the characteristics of magnetic force/torque with respect to its geometry or material property, the magnetic actuator is optimized as a basic study. By examining optimization results, the properties of magnetic circuit parameters such as nonlinear permeability, geometry, and mass are investigated. From this basic study, we seek a guideline to design the magnetic circuit of electric motors that improve the force/torque performance.

Switched reluctance mot ors are chosen as a practical application of the structural topology optimization. These motors are gaining much interest due to a number of their advantages. Their structure is simple, robust, and reliable even at very high speeds. In addition, they have high torque/weight ratio and high efficiency. Thus, switched reluctance motors are suitable for a variety of industrial applications including electric vehicles. For electric vehicle propulsion systems, three types of electric motors are considered as potential candidates [3]: permanent magnet brushless DC motors, induction motors, and switched reluctance motors. Figure 1.1.1 shows the two dimensional schematic view of three motors. Among these motors, we choose switched reluctance motors for the structural topology optimization due to the following reasons. Permanent magnet brushless DC motors are less attractive than other motors due to the high price of permanent magnets. Next, induction motors have only a small possibility of changing their geometry, and consequently their research has been focused on optimal control. In

contrast, the geometry of switched reluctance motors highly affects the motor performance. Therefore, considerable performance improvement of switched reluctance motors can be expected using structural topology optimization.

In this research, switched reluctance motors are designed using the structural topology optimization method. The main optimization goal is minimizing torque ripple without losing average torque, which is one of the biggest issues in these motors. As an additional goal, the mass of the motor is minimized for improving torque density. In addition, the root-mean-square value of the phase current is constrained to restrain the copper loss, which affects not only thermal stress, but also drive efficiency. To achieve these goals with the constraint, we optimize motor geometries using the mathematical programming approach, which requires sensitivity analysis of motor performance such as current curve and torque profile. For the sensitivity analysis, we newly propose the mathematical approximation model to represent the motor performance explicitly. Both two and three dimensional designs are presented with the assumption of linear permeability. In addition, the design considering nonlinearity due to magnetic saturation is presented and the effect of the nonlinearity is discussed. Through this research, we seek to find the best shape of switched reluctance motors to enhance their torque performance.

In the introduction, the literature on structural topology optimization in the magnetic field problem is summarized. Then, the literature on the analysis and design optimization of switched reluctance motors is described and the outline of the dissertation is presented.

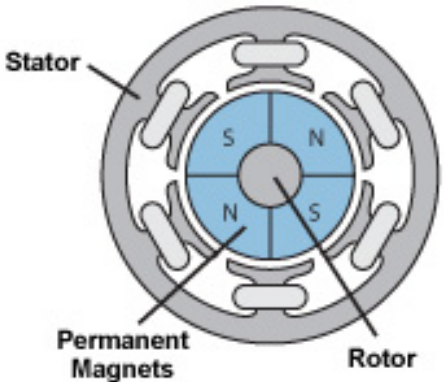

(a)

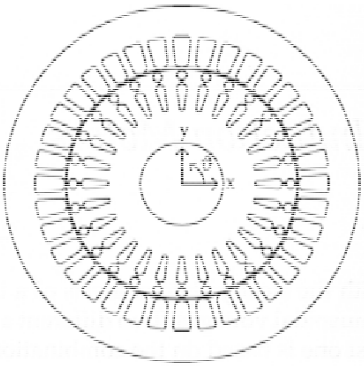

(b)

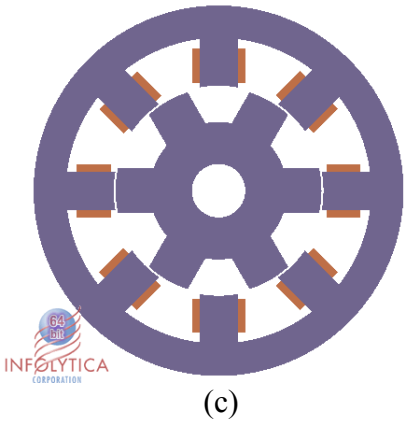

(c)

Figure 1.1.1 Electric motors for electric vehicles

(a) Permanent magnetic brushless DC motor, (b) induction motor,

(c) switched reluctance motor

1.2. Structural topology optimization in magnetic field

Since structural topology optimization was firstly introduced by Bendsøe and Kikuchi [4], it has been successfully applied to various application areas including magnetic field problems. This section reviews the structural topology optimization approaches for magnetic fields. The research before year 2000 is well documented in [5, 6], and therefore the only literatures within the last 10 years are presented here.

Many recent works on structural topology optimization dealing with magnetic fields have been conducted by Yoo and his colleagues. In his PhD work [5], the homogenization design method was first extended to the magnetic field problem. Using this method, the magnetic circuit was designed to maximize magnetic energy [7] and to minimize the frequency response caused by magnetic force [8]. In [9], the modified density approach based on the homogenization method was proposed for interpolating permeability. However, it was found that permeability interpolation causes the poor convergence history in the optimization result. To overcome this difficulty, reluctivity interpolation scheme was proposed in [10]. Then, it was shown that reluctivity interpolation gives improved performance and better robust iteration history compared to permeability interpolation. In addition, effort has been made to find a clear boundary shape which does not have intermediate densities. The clear design was obtained using parameter optimization with the response surface method, after the initial design was obtained from topology optimization [11]. The level-set method, which can represent the precise boundary shape of a structure, was first applied to the magnetic field problem [12]. The genetic algorithm, which uses only void and solid materials, was introduced to

design magnetic actuators [13]. As a practical application, perpendicular magnetic recording heads have been designed using the structural topology optimization [14, 15]. The design goals were preventing the leakage flux effect and increasing the recording flux density. Not only the yoke but also the coil shape was successfully designed for the given design goals.

Wang and his colleagues also have written many papers in this area. In [16], they first performed structural topology optimization in non-linear problems, where magnetic saturation effect was considered. They also firstly performed the optimization dealing the coupled field problems. The mechanical deformation caused by magnetic force was reduced in magneto-mechanical systems [17], and the temperature derived from eddy currents as the main heat source was minimized in magneto-thermal systems [18]. Level-set based topology optimization for the magnetic field problem was presented in [19]. In addition, they made much effort to apply structural topology optimization to practical applications. A single-phase induction motor was designed to reduce the oil circulation of a rotary compressor, and the design result is validated by experimental test [20]. A three-phase induction motor was also designed to alleviate heat load in a high-pressure scroll compressor [21].

Besides the above works, Kim and Okamoto have published on the structural optimization of magnetic fields. The characteristics of magnetic circuit design using the density method was investigated in [22], and the stacked-element connectivity parameterization approach was introduced to obtain converged material distribution in the non-linear problem [23]. Many practical applications were also designed using the structural topology optimization approach. An optical pickup actuator was designed using the coil design approach [24]. The design goal was to maximize the Lorentz force, and

coil conductivities were chosen as design variables. The optimal design of magnetostrictive sensor was presented to maximize the sensor output in both linear and non-linear problems [25], and a permanent magnetic of micro-speaker was optimized to maximize magnetic force on coils [26]. Structural topology optimization has been also applied to the design of perpendicular magnetic recording systems to decrease leakage flux [27], and to the design of three dimensional single-pole type recording heads to reduce leakage flux [28].

Many structural topology optimization approaches and their applications to practical devices have been reported. However, most of these studies have dealt with magnetic energy maximization in the linear problem. In this work, structural topology optimization to maximize magnetic force/torque is deeply investigated. In addition, optimization in the non-linear problem is presented, and the effect of nonlinearity in the magnetic field problem is investigated. A coupled magneto-structural problem is revisited using different force calculation method. As a practical application of this approach, the optimal design of switched reluctance motors are presented.

1.3. Analysis and design of switched reluctance motors

The analysis and design of a switched reluctance motor (SRM) has been extensively investigated by several researchers since SRM first became widely known in the early 1980's. The interest has been primarily due to the emerging markets for variable speed drives such as home appliances, hand tools, automotive and railway accessory drives. The electromagnetic principle of SRM is quite simple, but it is intended to operate in

deep magnetic saturation to increase the torque density. Therefore, the characteristics become highly nonlinear functions, and the nonlinearity makes it difficult to accurately predict SRM performance and to perform SRM design optimization.

Performance analysis

Many papers have been published on the static and dynamic performance analysis of SRM to predict the nonlinear inductance, electric current waveform, torque profile, and angular velocity. The basic understanding of operation and analysis of a SRM is first described in [29]. The finite element method was introduced to find nonlinear magnetic characteristics [30, 31], and the magnetic characteristics using the finite element analysis were compared with experimental test results [32]. An accurate model to describe the magnetic characteristics is extremely important in performance analysis and design optimization of SRM. A mathematical model for nonlinear magnetic characteristics has been developed via various kinds of interpolation functions: bi-cubic spline [33] , cubic-spline [34, 35], sinusoidal and arctangent functions [36], sinusoidal and polynomial functions [37-39], sinusoidal and geometry-based function [40], and only sinusoidal functions [41, 42]. However, none of these models can provide the explicit representation of SRM performance. In this work, a new mathematical model of magnetic characteristics using sinusoidal and piecewise quadratic polynomial functions is developed to obtain analytical representation of performance in a steady-state operation. In [43, 44], the steady-state operation of SRM was simulated by combining the finite element method with circuit analysis and experimentally verified. In this work, this simulation procedure is applied to the design optimization to reduce the torque ripple in a

steady-state operation. To predict the dynamic operation of SRM we need to solve a coupled set of equations: the circuit equation for torque profile and the mechanical equation for angular velocity (see reference [45, 46]). In this work, dynamic operation of SRM is not presented.

Vibration and heat analysis

The vibration and temperature rise in SRM significantly deteriorate motor performance. Therefore, vibration and thermal analysis using the finite element method has been performed. Vibration analysis in the frequency domain was first presented in [47], and the time domain analysis was first shown in [48]. Vibration analysis in the time domain was combined with the transient dynamic analysis [49]. Modal analysis was performed considering all motor components [50] and to determine the optimal radiating rib structure [51]. In this work, modal analysis of the designed stator is carried out using NASTRAN.

In the thermal analysis of electric motors, heat sources arise from motor losses which can be divided into iron loss and copper loss. The various loss models of SRM have been developed by several researchers. In contrast to the straightforward copper loss calculation using Ohm's law, iron loss calculation is not simple, and consequently there exist various iron loss models. The model using Fourier series analysis of flux waveforms was presented in [52, 53]. Three different models were compared with the experimentally measured data [54]. The iron loss model was separated into eddy-current and hysteresis losses and verified with experiments [55]. The six iron loss models were reviewed and a comprehensive model was developed in [56]. Based on the loss model, thermal analysis

has been performed using the finite element method. Transient temperature rise due to the core and copper loss of SRM was calculated and the effects of forced heat convection were examined in [57] . A transient and steady-state heat analysis of the three dimensional SRM model was introduced in [50] where a heat convection coefficient is calculated using a computational fluid dynamic analysis. Transient heat analysis with the calculated convention coefficients was presented and the effect of geometric parameters was investigated in [58]. In this work, only copper loss is considered as a heat source, and the steady-state thermal analysis of the deigned stator is performed using NASTRAN.

Design optimization

Design schemes to find optimal geometries of SRM have been reported in many papers. In [59-62], design results considering torque, heat, or vibration characteristics are presented for hybrid electric vehicle or electric vehicle applications. To improve SRM performance, the size and shape of the rotor and stator have been designed in many ways. In [63], it was found that a widened stator pole arc increases the average torque under the assumption of linear reluctivity. The optimal size of rotor and stator pole arc was obtained by examining the sensitivity of average torque with respect to arc/pole pitch ratio [64], and by checking the average torque and torque ripple curves with respect to the rotor and stator pole arc length [65]. Various optimization algorithms have been applied to find the optimal size of the rotor and stator. The first-order method of ANSYS was applied to minimize the material cost of SRM [66], and the progressive quadratic response surface method was used to minimize torque ripple and maximize the average torque [67]. The augmented Lagrangian method was used to minimize torque ripple [68],

and four optimization algorithms are applied to maximize the average torque and minimize the current supplied to SRM [69]. In addition to size optimization, the shape of the rotor and stator also has been optimized to minimize torque ripple. The degree of non-uniform airgap and the size of the pole shoe was optimized using the response surface method [70], and three rotor geometric parameters were optimized using the Pareto archived evolution strategy [71]. A notched rotor pole shape was proposed to minimize torque ripple after modified inductance curve was studied [72]. In addition, novel arrangement and shape of SRM have been proposed. A irregularly structured SRM operating in a short flux path was proposed in [73], and rotor-pole slits were proposed to enhance the output power of SRM [74]. A novel segmented SRM was proposed to improve the torque per weight ratio [75].

In this work, structural topology optimization is applied to the design of SRM for torque ripple minimization. Contrary to size or shape optimization and design depending on the designer's intuition, topology optimization does not require a fixed initial structural configuration. If the initial shape is fixed, performance improvement might be restricted depending on the chosen initial shape. The wrong decision about shape may not improve design performance at all. In contrast, structural topology optimization can represent any shape as a design result, and consequently considerable performance improvement can be expected. Structural topology optimization of SRMs have been reported in [76] and [77]. In [76], the magnetic energy profile was chosen as the objective function for the rotor design. In [77], the design objective was to minimize the mean compliance at a fixed rotor angle. These previous works, however, have not considered

the torque requirement, which is an essential goal of the motor design. In this work, structural topology optimization of SRM is presented to improve torque performance.

1.4. Outline of dissertation

The remainder of this dissertation is organized as follows:

Chapter 2 presents the finite element method for magnetostatic analysis. Two and three dimensional problems are explained, and the Newton-Raphson method to solve the non-linear problem is also described. In chapter 3, various kinds of magnetic force calculation methods are revisited and the numerical investigations are summarized. Chapter 4 presents the structural topology optimization in magnetic fields to investigate the effect of nonlinear permeability, volume, and magnetic force calculation methods. The optimization for the coupled magneto-structural problem is also presented. Chapter 5 shows the structural topology optimization of switched reluctance motors with the assumption of linear **B-H** relation. Chapter 6 presents the structural topology optimization of switched reluctance motors considering nonlinearity due to the magnetic saturation, and the effect of nonlinearity is discussed. Chapter 7 concludes the dissertation with remarks and future works.

CHAPTER 2
FINITE ELEMENT METHOD FOR MAGNETOSTATIC ANALYSIS

2.1. Introduction

The purpose of this chapter is to investigate the finite element method for the electromagnetic field analysis of electrical machinery. Figure 2.1.1 shows the division of electromagnetic analysis by its physical situation [78, 79]. Depending on the operating field frequency range of devices, the electromagnetic analysis can be divided into high and low frequency problems. Typical high frequency operating devices are waveguides, resonant cavities, and radiating devices such as antennae. Low frequency operating devices are electron devices, magnetic recording heads, and electrical machinery like electric motors. In low frequency problems, there are two static time-invariant field situations: electrostatics and magnetostatics. In electrostatics, a source charge is stationary, and an electric field around it is calculated. In magnetostatics, a moving charge, that is, electric current, generates a magnetic field. Magnetostatic analysis is suitable for electrical machinery that is activated by a current source. Because the goal of this dissertation is the design of electrical machinery such as actuators and electric motors, this chapter is mainly focused on magnetostatic analysis in the low frequency

electromagnetic problem. The magnetodynamic analysis that deals with the current induced by time-varying magnetic fields, also called as “eddy currents”, is not treated here.

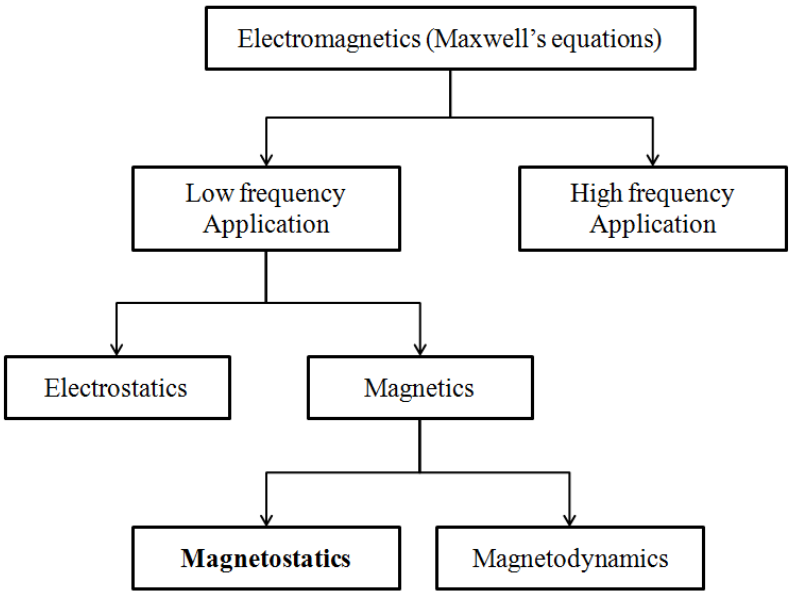

Figure 2.1.1 Electromagnetic division for physical applications [78]

The macroscopic electromagnetic field phenomenon is described by Maxwell’s equations and constitutive relations. For the magnetostatic analysis that we are focusing on, Maxwell’s equations are modified with constitutive relations. Section 2.2 explains the original Maxwell’s equation with constitutive relations and a modified equation for magnetostatic analysis [80-84]. The modified equation can be solved using the potential method with the finite element method. The finite element method is one of the most popular and reliable methods to solve magnetostatic problems in complex geometry.

Section 2.3 shows two kinds of potential methods for magnetostatic analysis, that is, scalar potential [85-92] and vector potential [78, 83, 85, 93]. Section 2.4 describes a gauge condition [80, 83] and uniqueness problem of the vector potential method. The finite element formulation is presented for the 2D linear problem in section 2.5 [78, 83, 94, 95], 3D linear problem in section 2.6 [83-85, 96, 97], and the problem for non-linear **B-H** relations in section 2.7 [78, 84, 93, 98, 99]. Section 2.8 presents numerical examples to verify the developed finite element program.

2.2. Maxwell's equation and its modification for magnetostatic analysis

A field is a spatial distribution of scalar or vector quantity, which may or may not be a function of time. There are four fundamental vector field quantities in electromagnetics: (a) Electric Field Intensity **E** (V/m), (b) Electric Flux Density D (C/m^2), (c) Magnetic Field Intensity **H** (A/m), and (d) Magnetic Flux Density **B** (T). Time-varying electric and magnetic vector fields are coupled, resulting in electromagnetic fields.

Interactions among electromagnetic fields can be described by Maxwell's equations. The differential form of Maxwell's equations is written as

$$\nabla \times \mathbf{E} = -\frac{\partial \mathbf{B}}{\partial t} \quad - \text{ Faraday's law} \tag{2.2.1}$$

$$\nabla \times \mathbf{H} = \mathbf{J} + \frac{\partial \mathbf{D}}{\partial t} \quad - \text{ Ampere's circuital law} \tag{2.2.2}$$

$$\nabla \cdot \mathbf{D} = \rho_v \quad - \text{ Gauss's law} \tag{2.2.3}$$

$$\nabla \cdot \mathbf{B} = 0 \quad - \text{ No name} \tag{2.2.4}$$

where ρ_v is volume charge density, and **J** is current density.

Maxwell's equations are in indefinite form because the number of equations is less than the number of unknowns. Maxwell's equations become definite when constitutive relations between the field quantities are specified. The constitutive relations describe the macroscopic properties of the medium and can be written as

$$\mathbf{D} = \varepsilon \mathbf{E} \tag{2.2.5}$$

$$\mathbf{B} = \mu \mathbf{H} \tag{2.2.6}$$

$$\mathbf{J} = \sigma \mathbf{E} \tag{2.2.7}$$

where ε, μ, and σ are material properties of a medium. ε is the permittivity, μ is the permeability, and σ is the conductivity of a medium. If the properties are functions of position, the medium is inhomogeneous, otherwise it is homogeneous. If properties vary with different directions, the medium is anisotropic, otherwise it is isotropic. In this dissertation, all material properties are assumed to be homogeneous and isotropic.

Maxwell's equations (2.2.1)-(2.2.4) with constitutive relations (2.2.5)-(2.2.7) can be modified for magnetostatic analysis. In a static case, all electromagnetic fields do not vary with the time. Time derivative terms in Eq. (2.2.1) and (2.2.2) are vanished, and therefore the interaction between electric and magnetic fields is broken. Therefore, Eq. (2.2.1) and (2.2.3) describe electrostatics, and Eq.(2.2.2) and (2.2.4) describe magnetostatics separately. Finally, equations for magnetostatic analysis can be written as

$$\nabla \times \mathbf{H} = \mathbf{J} \tag{2.2.8}$$

$$\nabla \cdot \mathbf{B} = 0 \tag{2.2.9}$$

To solve the above two first-order differential equations, the equations are converted into one second-order differential equation using the potential method.

2.3. Potential method for magnetostatic analysis

In magnetostatic analysis, two potential methods are available: (a) scalar potential Ω, and (b) vector potential A.

In the scalar potential method, magnetic field intensity **H** is written as

$$\mathbf{H} = \mathbf{T} + \nabla\Omega \tag{2.3.1}$$

The curl of the gradient is always zero

$$\nabla \times \left(\nabla\Omega\right) = 0 \tag{2.3.2}$$

Therefore, Eq. (2.2.8) with Eq. (2.3.1) can be written as

$$\nabla \times \mathbf{T} = \mathbf{J} \tag{2.3.3}$$

T can be any magnetic field satisfying the above equation. The magnetic field due to current in free space is chosen for **T** because this field can be calculated analytically using Biot-Savart's law [80]. After obtaining magnetic field **T**, the next step is to calculate the scalar potential Ω. Eq. (2.2.9) is modified into Poisson's equation with relation (2.2.6) and (2.3.1)

$$\nabla \cdot \left(\mu \nabla \Omega \right) = -\nabla \cdot \left(\mu \mathbf{T} \right) \tag{2.3.4}$$

By solving the above equation, scalar potential Ω is calculated, and finally the magnetic field intensity **H** can be obtained from Eq. (2.3.1).

In the vector potential method, the magnetic flux density **B** is represented as

$$\mathbf{B} = \nabla \times \mathbf{A} \tag{2.3.5}$$

The above relation automatically satisfies Eq. (2.2.9) because the gradient of curl is always zero

$$\nabla \cdot \left(\nabla \times \mathbf{A} \right) = 0 \tag{2.3.6}$$

Eq. (2.2.8) with the relation (2.2.6) and (2.3.5) is modified into the following equation

$$\nabla \times \left(\frac{1}{\mu} \nabla \times \mathbf{A} \right) = \mathbf{J} \tag{2.3.7}$$

By solving the above equation, the vector potential **A** is calculated, and finally the magnetic flux density **B** can be obtained from Eq. (2.3.5).

The advantages and shortcomings of each potential method are as follows. The vector potential method requires higher computation cost because it has three degree-of-freedom at a node while the scalar potential method has only one at a node. In addition, the vector potential method in three dimensional cases suffers from the uniqueness problem whereas the scalar potential method does not. The above is the shortcomings of the vector potential method. The shortcoming of the scalar potential method is as follows. The scalar potential method needs extra calculation to obtain magnetic field **T**, and the cancellation error can cause a severe problem in low magnetic field regions like iron objects. To avoid cancellation error, various methods [85-92] such as total, difference, general scalar potential methods are proposed depending on the source current configuration. However, extra calculation and complicated works are inevitable in the scalar potential method.

The choice of the potential method depends on the field dimensionality and domain size. In two dimensional problems, the vector potential method is preferred because degree of freedom is not a decisive factor, and there is no uniqueness problem in two dimensional problems. In three dimensional problems, both vector and scalar potential methods can be considered depending on the degree of freedom and uniqueness problem. We use the vector potential method, that is, Eq. (2.3.7), for both two dimensional and

three dimensional problems. For deriving the analytical sensitivity that is required for structural optimization, the vector potential method is preferred because of the simple calculation procedure.

2.4. Gauge condition and uniqueness problem

Eq. (2.3.7) does not determine vector potential **A** uniquely. Any vector potential function that can be written as $\mathbf{A} = \mathbf{A}' + \nabla f$ is a solution of Eq. (2.3.7) regardless of function f because the curl of the gradient is always zero. In order to fix the function f and obtain the unique vector potential **A**, we can impose a condition on the divergence of vector potential **A**. The simplest choice is zero divergence conditions. This is called a gauge condition and can be written as

$$\nabla \cdot \mathbf{A} = 0 \tag{2.4.1}$$

The function f satisfying a gauge condition is a solution of the following Poisson's equation.

$$\nabla^2 f = -\nabla \cdot \mathbf{A}' \tag{2.4.2}$$

The solution of Poisson's equation might be found uniquely. This can be the reason why a gauge condition gives a unique vector potential **A**.

A gauge condition is automatically satisfied in two dimensional problems. The detailed explanation is described in section 2.5. In three dimensional problems, it is

known that it is not necessary to impose the gauge condition if calculating **B** is the objective. Although vector potential **A** is not found uniquely without a gauge condition, the magnetic flux density **B** can be found uniquely.

2.5. 2D Finite element formulation for linear magnetostatic equation

Eq. (2.3.7) can be simplified in two dimensional problems. The current density **J** has only z-direction value, that is, $\mathbf{J} = 0 \cdot \hat{x} + 0 \cdot \hat{y} + J_z \hat{z}$. Therefore, vector potential **A** also has only z-direction value, that is, $\mathbf{A} = 0 \cdot \hat{x} + 0 \cdot \hat{y} + A_z \hat{z}$. Then, Eq. (2.3.7) in Cartesian coordinate becomes

$$-\frac{\partial}{\partial x}\left(\frac{1}{\mu}\frac{\partial A_z}{\partial x}\right)-\frac{\partial}{\partial y}\left(\frac{1}{\mu}\frac{\partial A_z}{\partial y}\right)=J_z \tag{2.5.1}$$

In this section, permeability μ is assumed to be constant, that is, it is not a function of magnetic flux density **B**. Then the above equation becomes linear with respect to vector potential **A**. In addition, permeability μ is assumed to be homogenous. Finally, the 2D linear magnetostatic equation is obtained as

$$\frac{\partial^2 A_z}{\partial x^2}+\frac{\partial^2 A_z}{\partial y^2}=-\mu J_z \tag{2.5.2}$$

We may say that the solution of Eq. (2.5.2) can be found uniquely although the solution of Eq. (2.3.7) cannot. The reasons are as follows. First, Eq. (2.5.2) is Poisson's equation having zero Dirichlet boundary conditions. The equation for heat conduction problem is exactly the same as Eq. (2.5.2), and the unique solution can be found physically in these problems. Second, vector potential **A** is restricted so that it has only z-direction value. Therefore, it is not true that any function written as $\mathbf{A} = \mathbf{A}' + \nabla f$ can be a solution of Eq. (2.5.2). Finally, if we apply a gauge condition to Eq. (2.3.7), we can also obtain Eq. (2.5.2). Therefore, the solution of Eq. (2.5.2) automatically satisfies a gauge condition. In conclusion, the vector potential method in two-dimensions does not have a uniqueness problem.

The numerical solution of Eq. (2.5.2) can be obtained using the finite element method. From the variational principle, it can be proved that the minimization of the following energy functional gives the solution of Eq. (2.5.2)

$$\mathbf{F}(A_z) = \frac{1}{2}\int_y \int_x \left[\left(\frac{\partial A_z}{\partial x} \right)^2 + \left(\frac{\partial A_z}{\partial y} \right)^2 + 2\mu J_z A_z \right] dx\, dy \tag{2.5.3}$$

The vector potential A_z in a element is approximated using shape functions **N**.

$$A_z^e = A_{zi}{}^e N_i^e(x, y) \tag{2.5.4}$$

From Eq. (2.5.4), Eq. (2.5.3) in a element becomes

$$ {}^{e}\mathbf{F}^{e}\left(A_z{}^{e}\right)=\frac{1}{2}\int_y\int_x\left[A_{zi}{}^{e}A_{zj}{}^{e}\left(\frac{\partial N_i^{e}}{\partial x}\frac{\partial N_j{}^{e}}{\partial x}+\frac{\partial N_i^{e}}{\partial y}\frac{\partial N_j{}^{e}}{\partial y}\right)+2\mu J_z{}^{e}A_{zi}{}^{e}N_i^{e}\right]dx\,dy \tag{2.5.5} $$

Minimizing Eq. (2.5.5) with respect to $A_{zk}{}^{e}$ gives

$$ \frac{\partial\mathbf{F}^{e}\left(A_z{}^{e}\right)}{\partial A_{zk}{}^{e}}=\int_y\int_x\left[A_{zj}{}^{e}\left(\frac{\partial N_i^{e}}{\partial x}\frac{\partial N_j{}^{e}}{\partial x}+\frac{\partial N_i^{e}}{\partial y}\frac{\partial N_j{}^{e}}{\partial y}\right)+\mu J_z{}^{e}N_j{}^{e}\right]dx\,dy=0 \tag{2.5.6} $$

$$ \int_y\int_x\left(\frac{\partial N_i^{e}}{\partial x}\frac{\partial N_j{}^{e}}{\partial x}+\frac{\partial N_i^{e}}{\partial y}\frac{\partial N_j{}^{e}}{\partial y}\right)dxdy\cdot A_{zj}{}^{e}=-\int_y\int_x\mu J_z{}^{e}N_i^{e}\,dxdy \tag{2.5.7} $$

$$ K_{ij}{}^{e}\cdot A_{zj}{}^{e}=f_i^{e} \tag{2.5.8} $$

Then, the element stiffness matrix and element force vector can be obtained as

$$ K_{ij}{}^{e}=\int_y\int_x\left(\frac{\partial N_i^{e}}{\partial x}\frac{\partial N_j{}^{e}}{\partial x}+\frac{\partial N_i^{e}}{\partial y}\frac{\partial N_j{}^{e}}{\partial y}\right)dxdy \tag{2.5.9} $$

$$ f_i=-\int_y\int_x\left(\mu J_z{}^{e}N_j{}^{e}\right)dxdy \tag{2.5.10} $$

The global matrix equation is obtained by summing the element stiffness matrix and element force vector. By solving the global matrix equation, the magnetic vector potential **A** at nodes can be obtained.

The magnetic flux density **B** can be determined from the calculated magnetic vector potential **A**. In two dimensional problems, Eq. (2.3.5) with Eq. (2.5.4) gives the x and y directional magnetic flux density in a element as

$$B_x^{\,e} = A_{zi}^{\,e} \frac{\partial N_i^e(x,y)}{\partial y} \tag{2.5.11}$$

$$B_y^{\,e} = -A_{zi}^{\,e} \frac{\partial N_i^e(x,y)}{\partial x} \tag{2.5.12}$$

2.6. 3D Finite element formulation for linear magnetostatic analysis

In three dimensional problems, Eq. (2.3.7) should be solved without any simplification. Any function written as $\mathbf{A} = \mathbf{A}' + \nabla f$ is the solution of Eq. (2.3.7). Therefore, a gauge condition should be considered for the uniqueness problem. There are three different variational formulations concerning a gauge condition: (a) without a gauge condition, (b) weak imposition of a gauge condition, (c) explicit imposition of a gauge condition. The first functional ignores a gauge condition and can be written as

$$\mathbf{F}_1(\mathbf{A}) = \frac{1}{2}\int_V \left[\frac{1}{\mu}(\nabla \times \mathbf{A})^2 - 2\mathbf{J}\cdot\mathbf{A} \right] dV \tag{2.6.1}$$

The second functional adds the divergence term as a penalty term and can be written as

$$\mathbf{F}_2(\mathbf{A}) = \frac{1}{2}\int_V \left[\frac{1}{\mu}(\nabla \times \mathbf{A})^2 - 2\mathbf{J}\cdot\mathbf{A} + \lambda(\nabla \cdot \mathbf{A})^2 \right] dV \tag{2.6.2}$$

The third functional imposes a gauge condition explicitly. From the vector calculus identity $\nabla \times (\nabla \times \mathbf{A}) = \nabla(\nabla \cdot \mathbf{A}) - \nabla \cdot (\nabla \mathbf{A})$, Eq. (2.3.7) can be modified as

$$-\frac{1}{\mu}\nabla \cdot (\nabla \mathbf{A}) = \mathbf{J} \tag{2.6.3}$$

Then, the functional becomes

$$\mathbf{F}_3(\mathbf{A}) = \frac{1}{2}\int_V \left[\frac{1}{\mu}(\nabla \cdot \mathbf{A})^2 - 2\mathbf{J}\cdot\mathbf{A} \right] dV \tag{2.6.4}$$

We choose the first functional $\mathbf{F}_1$ because magnetic flux density $\mathbf{B}$ is always unique although the vector potential $\mathbf{A}$ is not unique. The solution of the second functional $\mathbf{F}_2$ and third functional $\mathbf{F}_3$ do not exactly satisfy a gauge condition [83, 96], and consequently, fails to satisfy Eq. (2.3.7). The minimization of functional $\mathbf{F}_2$ and $\mathbf{F}_3$ satisfies Eq. (2.3.7) only when a gauge condition is exactly satisfied. To apply a gauge condition to the function $\mathbf{F}_1$, the tree-cotree gauge method was proposed [100]. However, it is shown that there is no computational advantage in this gauge method [97]. In conclusion, it is unnecessary to impose a gauge condition if the magnetic flux

density **B** is the quantity of primary interest [83, 97], and therefore we use the first functional $\mathbf{F}_1$, which ignores the gauge condition.

Two boundary conditions and nodal/edge element

It is well known that the magnetic flux density **B** in the normal direction and magnetic field intensity **H** in the tangential direction should be continuous at the material interface [80, 101]. These continuity requirements of the magnetic field are expressed as

$$B_{n\,m1} = B_{n\,m2} \tag{2.6.5}$$

$$H_{t\,m1} = H_{t\,m2} \tag{2.6.6}$$

where index $m1$ and $m2$ represent the different material. From Eq. (2.3.5), the above two requirements can be represented using magnetic vector potential **A** respectively as

$$\frac{\partial A_{t_2\,m1}}{\partial t_1 m1} - \frac{\partial A_{t_2\,m1}}{\partial t_1 m1} = \frac{\partial A_{t_2\,m2}}{\partial t_1 m2} - \frac{\partial A_{t_2\,m2}}{\partial t_1 m2} \tag{2.6.7}$$

$$\frac{1}{\mu_{m1}}\left(\frac{\partial A_{n\,m1}}{\partial t_2 m1} - \frac{\partial A_{t_2\,m1}}{\partial n\, m1}\right) = \frac{1}{\mu_{m2}}\left(\frac{\partial A_{n\,m2}}{\partial t_2 m2} - \frac{\partial A_{t_2\,m2}}{\partial n\, m2}\right) \tag{2.6.8}$$

where $t1$ and $t2$ are two orthogonal tangential directions at the material interface.

Although the conventional nodal element gives a reasonable overall magnetic field solution, it fails to obtain the accurate field solution at the material interfaces [102]. In

the nodal element it is assumed that not only the tangential but also the normal component of the vector potential **A** is continuous along any element interface. Then, the derivative of every component of vector potential **A** along the tangential direction is always continuous. Therefore, the first requirement Eq. (2.6.7) is automatically satisfied with the nodal vector potential method. In the second requirement two derivative terms $\frac{\partial A_n}{\partial t_2}$ and $\frac{\partial A_{t_2}}{\partial n}$ need to represent the jump due to the large difference of permeability μ between materials. However, the first derivative term $\frac{\partial A_n}{\partial t_2}$ is continuous in the nodal element because it is the tangential direction derivative. Only the second derivative term $\frac{\partial A_{t_2}}{\partial n}$ should represent the necessary jump. In some cases, the first continuous derivative term is much larger than the second discontinuous derivative term. In conclusion, the nodal vector potential method fails to satisfy the second continuity requirement Eq. (2.6.8).

To overcome this difficulty, the edge element is proposed. In this element, the degree-of-freedom is assigned to the edges rather than to the nodes. The shape function of edge element is in a vector form, and represents the direction of the vector potential **A**. The different type of approximation using the edge element allows discontinuity of the derivative term $\frac{\partial A_n}{\partial t_2}$, and therefore, the second continuity requirement is well satisfied with the edge element.

Now we move our focus back to how to solve Eq. (2.6.1) using the finite element method in both nodal and edge elements.

Finite element formulation using nodal element

In a 3D 8-node hexahedral isoparametric nodal element, the magnetic vector potential **A** is approximated as

$$\mathbf{A} = \sum_{i=1}^{8} \mathbf{A}_i N_i \tag{2.6.9}$$

It should be noted that three degree-of-freedom A_{xi}, A_{yi} and A_{zi} exist at a node, and the shape function N_i at a node is a scalar function. From the approximated vector potential Eq. (2.6.9), Eq. (2.6.1) in a element becomes

$$\begin{aligned}\mathbf{F}_1^e\left(\mathbf{A}^e\right) = \frac{1}{2\mu}\int_V & \left(\frac{\partial N_i^e}{\partial y} A_{xi}{}^e\right)^2 + \left(\frac{\partial N_i^e}{\partial z} A_{xi}{}^e\right)^2 + \left(\frac{\partial N_i^e}{\partial x} A_{yi}{}^e\right)^2 \\ & + \left(\frac{\partial N_i^e}{\partial z} A_{yi}{}^e\right)^2 + \left(\frac{\partial N_i^e}{\partial x} A_{zi}{}^e\right)^2 + \left(\frac{\partial N_i^e}{\partial y} A_{zi}{}^e\right)^2 \\ & - 2\left(\frac{\partial N_i^e}{\partial x} A_{xi}{}^e \frac{\partial N_j^e}{\partial y} A_{yj}{}^e + \frac{\partial N_i^e}{\partial x} A_{xi}{}^e \frac{\partial N_j^e}{\partial z} A_{zj}{}^e + \frac{\partial N_i^e}{\partial y} A_{yi}{}^e \frac{\partial N_j^e}{\partial z} A_{zj}{}^e\right) \\ & - 2\mu\left(N_i^e A_{xi}{}^e J_x + N_i^e A_{yi}{}^e J_y + N_i^e A_{zi}{}^e J_z\right)\ dV\end{aligned} \tag{2.6.10}$$

The minimization of Eq. (2.6.10) with respect to nodal vector potential A_{xk}, A_{yk}, and A_{zk} in a element gives

$$\frac{\partial \mathbf{F}_1^e}{\partial A_{xk}} = \sum_{j=1}^{8} \left(\int_V \frac{1}{\mu} \left(\frac{\partial N_i^e}{\partial y} \frac{\partial N_j^e}{\partial y} + \frac{\partial N_i^e}{\partial z} \frac{\partial N_j^e}{\partial z} \right) dV \right) A_{xj}^e - \left(\int_V \frac{1}{\mu} \left(\frac{\partial N_i^e}{\partial x} \frac{\partial N_j^e}{\partial y} \right) dV \right) A_{yj}^e - \left(\int_V \frac{1}{\mu} \left(\frac{\partial N_i^e}{\partial x} \frac{\partial N_j^e}{\partial z} \right) dV \right) A_{zj}^e - \int_V \left(N_i^e J_x \right) dV = 0 \tag{2.6.11}$$

$$\frac{\partial \mathbf{F}_1^e}{\partial A_{yk}} = \sum_{j=1}^{8} -\left(\int_V \frac{1}{\mu} \left(\frac{\partial N_i^e}{\partial y} \frac{\partial N_j^e}{\partial x} \right) dV \right) A_{xj}^e + \left(\int_V \frac{1}{\mu} \left(\frac{\partial N_i^e}{\partial x} \frac{\partial N_j^e}{\partial x} + \frac{\partial N_i^e}{\partial z} \frac{\partial N_j^e}{\partial z} \right) dV \right) A_{yj}^e - \left(\int_V \frac{1}{\mu} \left(\frac{\partial N_i^e}{\partial y} \frac{\partial N_j^e}{\partial z} \right) dV \right) A_{zj}^e - \int_V \left(N_i^e J_y \right) dV = 0 \tag{2.6.12}$$

$$\frac{\partial \mathbf{F}_1^e}{\partial A_{zk}} = \sum_{j=1}^{8} -\left(\int_V \frac{1}{\mu} \left(\frac{\partial N_i^e}{\partial z} \frac{\partial N_j^e}{\partial x} \right) dV \right) A_{xj}^e - \left(\int_V \frac{1}{\mu} \left(\frac{\partial N_i^e}{\partial z} \frac{\partial N_h^e}{\partial y} \right) dV \right) A_{yj}^e + \left(\int_V \frac{1}{\mu} \left(\frac{\partial N_i^e}{\partial x} \frac{\partial N_j^e}{\partial x} + \frac{\partial N_i^e}{\partial y} \frac{\partial N_j^e}{\partial y} \right) dV \right) A_{zj}^e - \int_V \left(N_i^e J_z \right) dV = 0 \tag{2.6.13}$$

The above equations (2.6.11)-(2.6.13) can be written as matrix form as

$$\begin{bmatrix} K_{xx}^e & K_{xy}^e & K_{xz}^e \\ K_{yx}^e & K_{yy}^e & K_{yz}^e \\ K_{zx}^e & K_{zy}^e & K_{zz}^e \end{bmatrix} \begin{pmatrix} A_x^e \\ A_y^e \\ A_z^e \end{pmatrix} = \begin{pmatrix} f_x^e \\ f_y^e \\ f_z^e \end{pmatrix} \tag{2.6.14}$$

$$K_{xx}^e = \int_V \frac{1}{\mu} \left(\frac{\partial N_i^e}{\partial y} \frac{\partial N_j^e}{\partial y} + \frac{\partial N_i^e}{\partial z} \frac{\partial N_j^e}{\partial z} \right) dV \tag{2.6.15}$$

$$K_{yy}^e = \int_V \frac{1}{\mu} \left(\frac{\partial N_i^e}{\partial x} \frac{\partial N_j^e}{\partial x} + \frac{\partial N_i^e}{\partial z} \frac{\partial N_j^e}{\partial z} \right) dV \tag{2.6.16}$$

$$K_{zz}{}^{e} = \int_V \frac{1}{\mu}\left(\frac{\partial N_i^e}{\partial x}\frac{\partial N_j{}^{e}}{\partial x} + \frac{\partial N_i^e}{\partial y}\frac{\partial N_j{}^{e}}{\partial y}\right)dV \tag{2.6.17}$$

$$K_{pq}{}^{e} = -\int_V \frac{1}{\mu}\left(\frac{\partial N_i^e}{\partial p}\frac{\partial N_j{}^{e}}{\partial q}\right)dV \qquad p,q = x,y,z \;; \quad p \neq q \tag{2.6.18}$$

$$f_p{}^{e} = \int_V \left(N_i^e J_p\right)dV \qquad p = x,y,z \tag{2.6.19}$$

From Eq. (2.6.14)-(2.6.19), the element stiffness matrix and element force vector can be found. By summing the element stiffness matrix and force vector, the global matrix equation is derived. By solving this equation, the magnetic vector potential **A** at nodes can be obtained.

The magnetic flux density **B** in a Cartesian coordinate can be determined from the calculated magnetic vector potential **A**, and can be written as

$$B_x{}^{e} = A_{zi}{}^{e}\frac{\partial N_i^e}{\partial y} - A_{yi}{}^{e}\frac{\partial N_i^e}{\partial z} \tag{2.6.20}$$

$$B_y{}^{e} = A_{xi}{}^{e}\frac{\partial N_i^e}{\partial z} - A_{zi}{}^{e}\frac{\partial N_i^e}{\partial x} \tag{2.6.21}$$

$$B_z{}^{e} = A_{yi}{}^{e}\frac{\partial N_i^e}{\partial x} - A_{xi}{}^{e}\frac{\partial N_i^e}{\partial y} \tag{2.6.22}$$

Finite element formulation using edge element

In a 3D hexahedral isoparametric edge element, the magnetic vector potential A is approximated as

$$\mathbf{A} = \sum_{i=1}^{12} A_i \mathbf{N}_i \tag{2.6.23}$$

where A_i is the scalar degree of freedom at each 12 edge, and $\mathbf{N}_i$ is the vector shape function that has non-zero tangential components only along edges on its degree-of-freedom. The vector shape function in an isoparametric element can be represented as

$$\mathbf{N}_i = N_i(r,s,t)\nabla e_i \qquad e_{1,3,5,7} = r,\ e_{2,4,6,8} = r,\ e_{9,10,11,12} = t \tag{2.6.24}$$

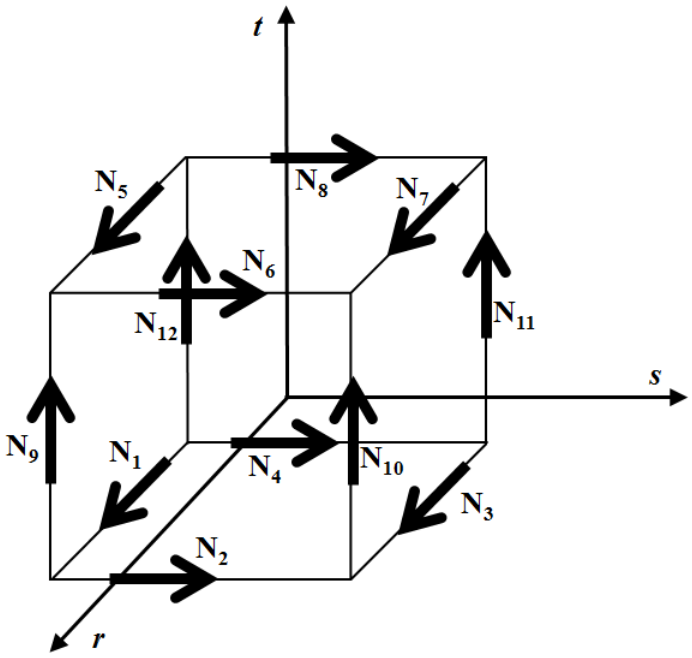

Figure 2.6.1. Vector shape functions of edge element

Figure 2.6.1 shows the location of each vector shape function. The scalar component N_i in vector shape functions is defined so as to satisfy the following properties

$$\int_{i\text{ th edge}} N_i(r,s,t)\, d\Gamma_i = 1 \tag{2.6.25}$$

$$\int_{\text{other edge}} N_i(r,s,t)\, d\Gamma_i = 0 \tag{2.6.26}$$

, which means that the line integral on its edge is one and on other edge is zero.

From Eq. (2.6.23) and (2.6.24), the curl of vector potential **A** in Eq. (2.6.1) can be represented as

$$\nabla \times \mathbf{A} = \sum_{i=1}^{12} \nabla \times \left(A_i N_i \nabla e_i \right) \tag{2.6.27}$$

From vector calculus identity $\nabla \times (\varphi \mathbf{a}) = \nabla\varphi \times \mathbf{a} + \varphi \nabla \times \mathbf{a}$ and $\nabla \times (\nabla\varphi)$, Eq. (2.6.27) becomes

$$\nabla \times \mathbf{A} = \sum_{i=1}^{12} \left[A_i \left(\nabla \mathbf{N}_i \times \nabla e_i \right) \right] \tag{2.6.28}$$

Then, the functional Eq. (2.6.1) in a element can be written as

$$\mathbf{F}_1^e\left(\mathbf{A}^e\right)=\frac{1}{2}\int_V\frac{1}{\mu}\left[\left(\mathrm{A}_i{}^e\mathrm{A}_j{}^e\left(\nabla N_i^e\times\nabla e_i\right)\cdot\left(\nabla N_j{}^e\times\nabla e_j\right)\right)\right]-2\left(\mathrm{A}_i{}^e\mathrm{J}_j\left(N_i^e\nabla e_i\right)\cdot\left(N_j{}^e\nabla e_j\right)\right)dV \tag{2.6.29}$$

The minimization of Eq. (2.6.29) with respect to edge vector potential A^e in a element gives

$$\frac{\partial\mathbf{F}_1^e}{\partial\mathrm{A}_k{}^e}=\sum_{\mathrm{j}=1}^{12}A_j\left[\int_V\frac{1}{\mu}\left(\nabla N_i\times\nabla e_i\right)\cdot\left(\nabla N_j\times\nabla e_j\right)-\mathrm{J}_j\left(N_i\nabla e_i\right)\cdot\left(N_j\nabla e_j\right)dV\right] \tag{2.6.30}$$

$$\int_V\frac{1}{\mu}\left(\nabla N_i\times\nabla e_i\right)\cdot\left(\nabla N_j\times\nabla e_j\right)dV\cdot A_j{}^e=\int_V\mathrm{J}_j\left(N_i\nabla e_i\right)\cdot\left(N_j\nabla e_j\right)dV \tag{2.6.31}$$

$$K_{ij}{}^e\cdot A_{zj}{}^e=f_i^e \tag{2.6.32}$$

Then, the element stiffness matrix and element force vector can be obtained as

$$K_{ij}{}^e=\int_V\frac{1}{\mu}\left(\nabla N_i\times\nabla e_i\right)\cdot\left(\nabla N_j\times\nabla e_j\right)dV \tag{2.6.33}$$

$$f_i=-\int_V\mathrm{J}_j\left(N_i\nabla e_i\right)\cdot\left(N_j\nabla e_j\right)dV \tag{2.6.34}$$

The gradient of N_i and e_i can be calculated using the coordinate transformation matrix in an isoparametric element. The global matrix equation is obtained by summing the element stiffness matrix and element force vector. By solving the global matrix equation, the magnetic vector potential **A** can be obtained.

The magnetic flux density **B** in a Cartesian coordinate can be determined from the calculated magnetic vector potential **A**, and can be written as

$$B_x^e = A_i^e \left(\frac{\partial \mathbf{N}_i^e}{\partial y} - \frac{\partial \mathbf{N}_i^e}{\partial z} \right) \tag{2.6.35}$$

$$B_y^e = A_i^e \left(\frac{\partial \mathbf{N}_i^e}{\partial z} - \frac{\partial \mathbf{N}_i^e}{\partial x} \right) \tag{2.6.36}$$

$$B_z^e = A_i^e \left(\frac{\partial \mathbf{N}_i^e}{\partial x} - \frac{\partial \mathbf{N}_i^e}{\partial y} \right) \tag{2.6.37}$$

2.7. Finite element formulation for non-linear B-H relation

The permeability μ of common materials depends on the magnetic field. Figure 2.7.1 shows **B-H** curve of three types of steel [103]. In a low magnetic field, magnetic flux density **B** is proportional to magnetic field intensity **H**. Then, the permeability μ is constant. However, in a high magnetic field, magnetic saturation occurs, and therefore, magnetic flux density **B** increase less as magnetic field intensity **H** increases. In this case, the permeability μ is a function of magnetic flux density **B**. In [103], the permeability μ model using an exponential function is proposed and can be written as

$$\frac{1}{\mu\left(B^2\right)} = k_1 e^{k_2 B^2} + k_3 \tag{2.7.1}$$

The non-linear **B-H** relation also makes the magnetostatic problem non-linear. Because most electro-mechanical devices operate in the non-linear **B-H** region, analysis of the non-linear magnetostatic problem is necessary. This chapter shows how to solve the non-linear magnetostatic problem using the Newton-Raphson method, which is the most common method for solving non-linear problems.

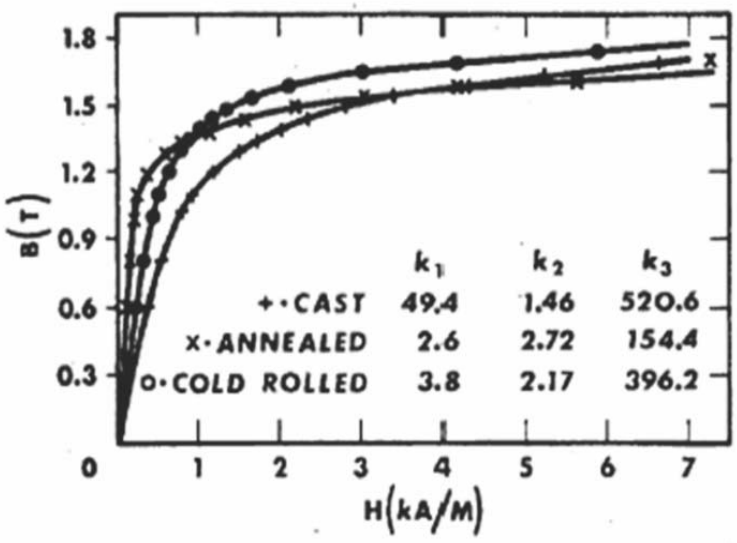

Figure 2.7.1. **B-H** curve of steel

The energy functional of 2D non-linear magnetostatic problems can be defined as

$$\mathbf{F}_{non-linear}(A_z) = \int_V \left[\int H \, dB - J_z A_z \right] dV \tag{2.7.2}$$

From (a) the approximation of **A** – Eq. (2.5.4), (b) constitutive relation – Eq. (2.2.6), (c) permeability model – Eq. (2.7.1), Eq. (2.7.2) in a element is modified as

$$\mathbf{F}_{non-linear}(A_z) = \int_V \left[\int \frac{1}{k_1 e^{k_2 B^2} + k_3} B\, dB - J_z N_p A_{zp} \right] dV \tag{2.7.3}$$

The minimization of function (2.7.3) with respect to the vector potential A_{zi} gives

$$\frac{\partial \mathbf{F}_{non-linear}}{\partial A_{zi}} = \int_V \left[\frac{\partial \left(\int \frac{1}{k_1 e^{k_2 B^2} + k_3} B\ dB \right)}{\partial A_{zi}} - J_z N_i \right] dV = 0 \tag{2.7.4}$$

The first term can be modified as

$$\begin{aligned} \frac{\partial \left(\int_0^B \frac{1}{k_1 e^{k_2 b^2} + k_3} b\ db \right)}{\partial A_{zi}} &= \frac{1}{2} \frac{\partial \left(\int_0^B \frac{1}{k_1 e^{k_2 b^2} + k_3}\ db^2 \right)}{\partial A_{zi}} \quad \left(\because db^2 = 2b\, db \right) \\ &= \frac{1}{2} \frac{\partial \left(M\left(B^2\right) - M(0) \right)}{\partial A_{zi}} \qquad \left(\because \frac{\partial \left(M\left(b^2\right) \right)}{\partial b^2} = \frac{1}{k_1 e^{k_2 b^2} + k_3} \right) \\ &= \frac{1}{2} \frac{\partial \left(M\left(B^2\right) - M(0) \right)}{\partial B^2} \frac{\partial B^2}{\partial A_{zi}} = \frac{1}{2} \frac{1}{k_1 e^{k_2 b^2} + k_3} \frac{\partial B^2}{\partial A_{zi}} \end{aligned} \tag{2.7.5}$$

Because the square of the magnetic flux density B^2 can be written as

$$B^2 = \mathbf{B}\cdot\mathbf{B} = \left(A_{zm}\frac{\partial N_m}{\partial y}\hat{x} - A_{zm}\frac{\partial N_m}{\partial x}\hat{y} \right)\cdot\left(A_{zn}\frac{\partial N_n}{\partial y}\hat{x} - A_{zn}\frac{\partial N_n}{\partial x}\hat{y} \right)$$
$$= A_{zm}\left(\frac{\partial N_m}{\partial x}\frac{\partial N_n}{\partial x} + \frac{\partial N_m}{\partial y}\frac{\partial N_n}{\partial y} \right) A_{zn} \tag{2.7.6}$$

Then the term $\frac{\partial B^2}{\partial A_{zi}}$ becomes

$$\frac{\partial B^2}{\partial A_{zi}} = 2\left(\frac{\partial N_i}{\partial x}\frac{\partial N_j}{\partial x} + \frac{\partial N_i}{\partial y}\frac{\partial N_j}{\partial y} \right) A_{zj} \tag{2.7.7}$$

From Eq. (2.7.5) and (2.7.7), Eq. (2.7.4) becomes

$$\int_V \left[\frac{1}{k_1 e^{k_2 B^2} + k_3}\left(\frac{\partial N_i}{\partial x}\frac{\partial N_j}{\partial x} + \frac{\partial N_i}{\partial y}\frac{\partial N_j}{\partial y} \right) \right] dV \cdot A_{zj} - \int_V J_z N_i \, dV = 0 \tag{2.7.8}$$

$$F_{non-linear} = K_{ij}\left(A_z \right)\cdot A_{zj} - f_i = 0 \tag{2.7.9}$$

To solve the above non-linear equation, we apply the Newton-Raphson iteration method. This method is the best known method to find the root of a non-linear equation. In this method, better approximation of the root is assumed using the derivative of the equation. Using this method, the better approximation of the solution of Eq. (2.7.9) can be written as

$$A_{zj}^{(n+1)} = A_{zj}^{(n)} - \mathbf{J}^{-1}\left(A_{zj}^{(n)}\right) F_{non-linear}\left(A_{zj}^{(n)}\right) \tag{2.7.10}$$

The Jacobian matrix **J** is composed of the derivative of the equation with respect to unknowns and can be written as

$$\mathbf{J}(\mathbf{x}) = \begin{bmatrix} \frac{\partial F_{non-linar\ 1}}{\partial A_{z1}} & \frac{\partial F_{non-linar\ 1}}{\partial A_{z2}} & \cdots & \frac{\partial F_{non-linar\ 1}}{\partial A_{zm}} \\ \frac{\partial F_{non-linar\ 2}}{\partial A_{z1}} & \frac{\partial F_{non-linar\ 2}}{\partial A_{z2}} & \cdots & \frac{\partial F_{non-linar\ 2}}{\partial A_{zm}} \\ \vdots & \vdots & & \vdots \\ \frac{\partial F_{non-linar\ m}}{\partial A_{z1}} & \frac{\partial F_{non-linar\ m}}{\partial A_{z2}} & \cdots & \frac{\partial F_{non-linar\ m}}{\partial A_{zm}} \end{bmatrix} \tag{2.7.11}$$

The component of the Jacobian matrix **J** can be written as

$$J_{ij} = \frac{\partial F_{non-linar\ i}}{\partial A_{zj}} = \frac{\partial\left(K_{ik} A_{zk} - f_i\right)}{\partial A_{zj}} = K_{ij} + \frac{\partial K_{ik}}{\partial A_{zj}} A_{zk} \tag{2.7.12}$$

From Eq. (2.7.7), the derivative of K_{ik} with respect to A_{zj} can be derived as

$$\frac{\partial K_{ik}}{\partial A_{zj}} = \frac{\partial\left(\int\left(\frac{1}{k_1 e^{k_2 B^2}+k_3}\left(\frac{\partial N_i}{\partial x}\frac{\partial N_k}{\partial x}+\frac{\partial N_i}{\partial y}\frac{\partial N_k}{\partial y}\right)\right)d\Omega\right)}{\partial A_{zj}}$$

$$= \frac{\partial\left(\int\left(\frac{1}{k_1 e^{k_2 B^2}+k_3}\left(\frac{\partial N_i}{\partial x}\frac{\partial N_k}{\partial x}+\frac{\partial N_i}{\partial y}\frac{\partial N_k}{\partial y}\right)\right)d\Omega\right)}{\partial B^2}\frac{\partial B^2}{\partial A_{zj}} \tag{2.7.13}$$

$$= 2\int\left(\frac{\partial\left(\frac{1}{k_1 e^{k_2 B^2}+k_3}\right)}{\partial B^2}\left(\frac{\partial N_i}{\partial x}\frac{\partial N_k}{\partial x}+\frac{\partial N_i}{\partial y}\frac{\partial N_k}{\partial y}\right)\left(\frac{\partial N_j}{\partial x}\frac{\partial N_n}{\partial x}+\frac{\partial N_j}{\partial y}\frac{\partial N_n}{\partial y}\right)A_{zn}\right)d\Omega$$

From Eq. (2.7.10)-(2.7.13), the solution of Eq. (2.7.9) can be obtained, and finally the magnetic field with non-linear permeability can be found.

In the Newton-Raphson method, it should be noted that the appropriate initial solution is very important. If the initial solution is too far from the final solution, the method may fail to find the final solution. Therefore the initial solution needs to be close to the final solution although we cannot predict the final solution. In Eq. (2.7.9), the final solution of A_{zj} is zero if the right-hand-side term f_i is zero. For making the initial solution close to the final solution, we set the initial solution as zero, and then gradually increase the right-hand-side term f_i for each iteration.

2.8. Numerical examples

In this chapter, numerical examples are presented to verify the developed finite element program for magnetostatic analysis. The developed finite element program is

applied to analyze the magnetic actuator model modified from [10]. Both two and three dimensional models are analyzed with both a linear and non-linear problems. Geometries and meshes of each component of magnetic actuator are presented in Figure 2.8.1. In the two dimensional models shown in Figure 2.8.1 (a), the winded coil is modeled as two separated rectangles, and current density is applied as opposite directions. Figure 2.8.1 (b) shows three dimensional models without the mesh of air elements. Because the air elements surround all other components, we need to remove the air elements to see the components' configuration. In three dimensional models, the divergence of the current density should be zero to obtain the converged solution [97]. The continuity condition is not sensitive when we use the nodal element, but it can cause a serious error in the edge element [104]. Therefore, the current density in three dimensional problems is chosen to strictly satisfy the continuity condition.

The quantity of the current density is set as $0.428571\times10^{9}\ A/m^{2}$ considering the area of the coil part and the number of windings. At the outer boundary, the vector potential **A** is set as zero. This means that magnetic field is insulated at the boundary, and therefore, the magnetic flux does not flow outside the boundary.

The magnetic vector potential **A** and magnetic flux density **B** are calculated using the developed program. To verify the developed program, the results are compared with those calculated from commercial programs ANSYS and COMSOL. The analysis results are presented as the following order: 2D linear model in section 2.8.1, 2D non-linear model in section 2.8.2, 3D linear model in section 2.8.3, 3D non-linear model section 2.8.4.

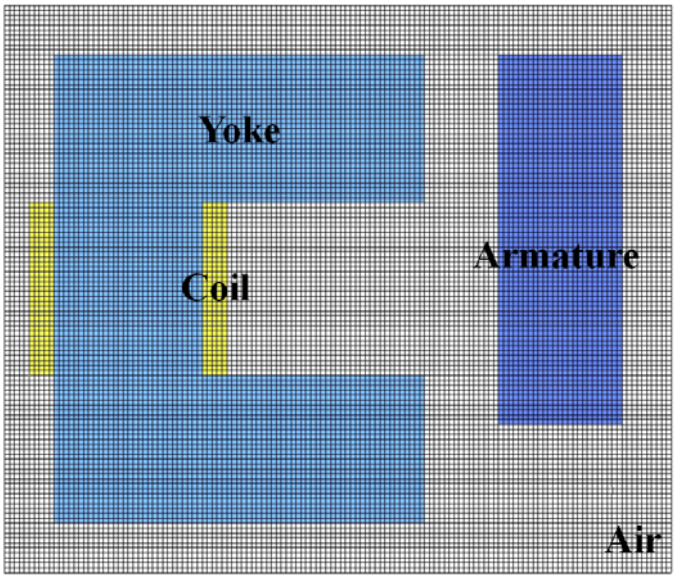

(a)

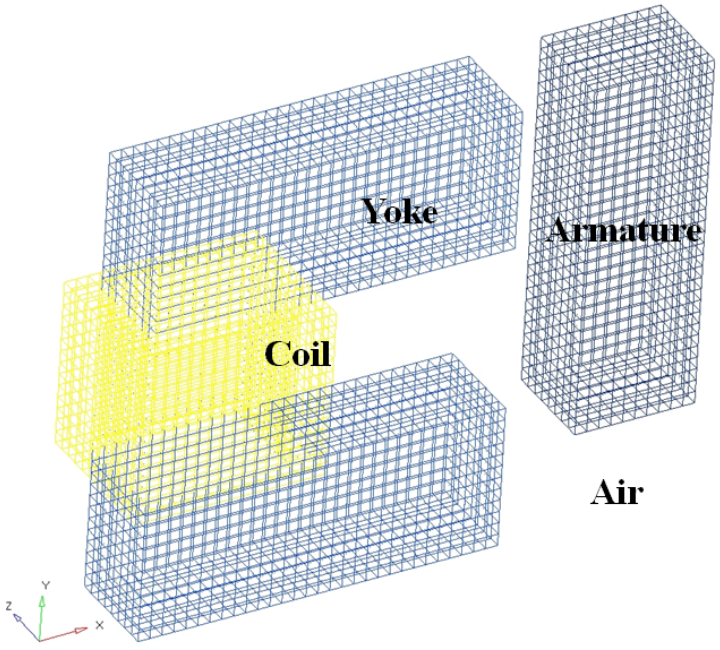

(b)

Figure 2.8.1. Magnetic actuator model

(a) 2D model, (b) 3D model

2.8.1. 2D Linear model

Two dimensional analysis of the magnetic actuator is performed when the **B-H** relation is linear. The permeability of yoke and armature is assumed to be constant at 1.9209×10^{-3} H/m. Figure 2.8.2 shows the equipotential lines of vector potential **A** calculated from each FEA program. The lines are almost identical, and therefore, the developed program is verified for two dimensional linear magnetostatic analysis.

In two dimensional cases, the equipotential lines physically mean the direction of magnetic flux density. The reason can be explained as follows. The gradient of vector potential A_z can be written as

$$\nabla A_z = \begin{pmatrix} \dfrac{\partial A_z}{\partial x} \\ \dfrac{\partial A_z}{\partial y} \\ 0 \end{pmatrix} \tag{2.8.1}$$

The direction of the gradient of a scalar is normal to the lines which have constant scalar value. Therefore, the gradient of vector potential A_z is normal to equipotential lines. In two dimensional cases, the magnetic flux **B** is normal to ∇A_z as can be seen in Eq. (2.5.11) -(2.5.12). Therefore, the direction of magnetic flux **B** is tangential to the equipotential lines. Finally, we may say that the magnetic flux flows along the equipotential lines in two dimensional cases.

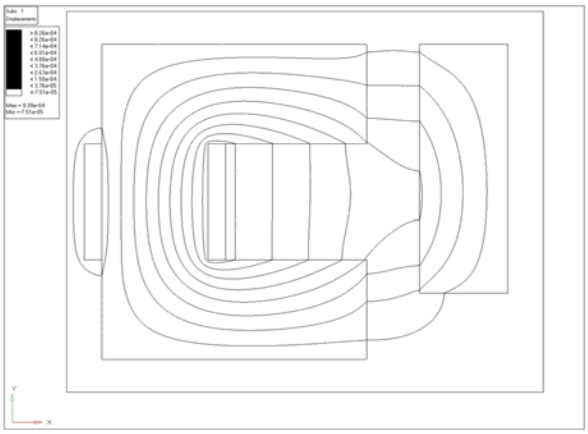

(a)

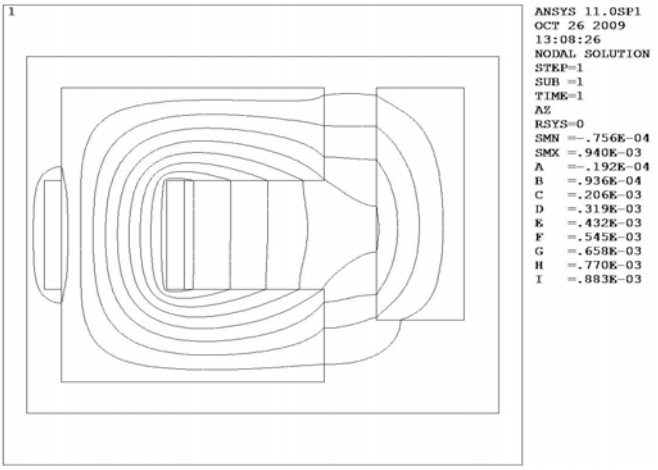

(b)

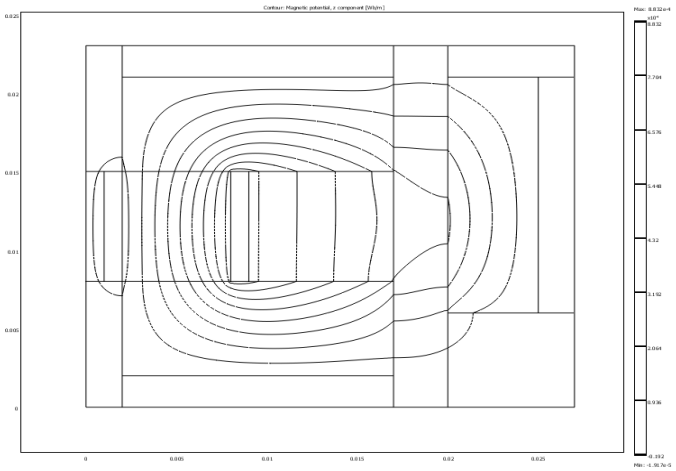

(c)

Figure 2.8.2. Equipotential lines of vector potential **A** in 2D linear case

(a) Developed Program, (b) ANSYS, (c) COMSOL

The magnetic energy W_f over the whole domain in linear problems, can be represented as

$$W_f = \int_V \left(\frac{1}{2} HB \right) dV \tag{2.8.2}$$

As can be seen in Table 2.8.1, the energy results calculated from each finite element program are exactly identical.

Table 2.8.2 compares the vector potential **A** at some nodes. This table shows that the vector potential **A** calculated from each program is exactly identical. Table 2.8.3 shows the calculated magnetic flux density **B**. All four nodes in this table are in one element, whose number is 13443. Because magnetic flux density **B** is not continuous at the interface of elements, one node has four different values calculated from four elements. Each program has its own method to determine the magnetic flux density **B** at nodes from different values. Therefore, the flux density **B** is slightly different in each result, although vector potential **A** is identical. These three tables confirm that the developed program is reliable for two dimensional linear magnetostatic analysis. The location of nodes used in the above comparison is shown in Figure 2.8.3.

Table 2.8.1. Comparison of magnetic energy $W_f(J)$ – 2D linear case

	Developed Program	**ANSYS**	**COMSOL**

Magnetic energy W_f	14.832	14.832	14.832

Table 2.8.2. Comparison of vector potential **A** (*Wb/m*) – 2D linear case

Node Number	**814**	**1256**	**4360**
Developed Program	0.18089E-02	0.11468E-03	0.68706E-02
ANSYS	0.18089E-02	0.11468E-03	0.68706E-02
COMSOL	0.18089E-02	0.11468E-03	0.68706E-02

Table 2.8.3. Comparison of magnetic flux density **B** (Wb/m^2) – 2D linear case

Node Number in element 13343		**1274**	**6041**	**14090**	**6236**
Developed Program	B_x	-0.957677	-1.024102	-1.024102	-0.957677
	B_y	0.782605	0.782605	0.716181	0.716181
ANSYS	B_x	-0.95768	-1.0241	-1.0241	-0.95768E-01
	B_y	0.78260	0.78260	0.71618E-01	0.71618E-01

COMSOL	B_x	-0.957664	-1.024086	-1.024086	-0.957664
	B_y	0.782595	0.782595	0.716172	0.716172

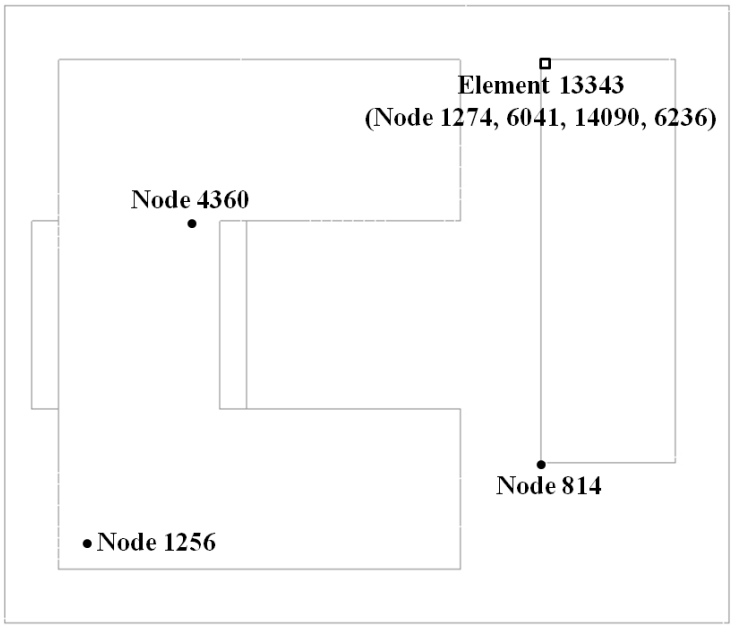

Figure 2.8.3. Location of nodes and element for comparison of **A** and **B**

2.8.2. 2D Non-linear model

Two dimensional analysis of the magnetic actuator model is performed when the **B-H** relation is non-linear. The geometries and boundary conditions are the same as those used

in the previous section for the linear model. The only difference is the permeability μ of the yoke and armature. Cast iron is used for the non-linear permeability. Therefore, the coefficients in Eq. (2.7.1) are set as k_1=49.4 k_2=1.46, k_3=520.6 as can be seen in Figure 2.7.1.

The analysis results obtained from three finite element programs are compared. The equipotential lines of vector potential **A** are shown in Figure 2.8.4. The lines obtained from each finite element program seem to be exactly identical.

In the figure of equipotential lines, we can see the effect of non-linear permeability. In the non-linear case, the permeability μ decreases as magnetic flux density **B** increases. The decreased permeability interrupts the increase of the magnetic flux density **B**. Therefore, the concentration of magnetic flux density at the narrow flux path is avoided, and the magnetic flux density is willing to be distributed more evenly. This non-linear effect can be seen in equipotential lines. In two dimensional equipotential lines, the dense and curved line means strong magnetic flux density. If comparing equipotential lines of the non-linear case (Figure 2.8.4) with the linear case (Figure 2.8.2), we can notice that the lines are modified to avoid dense and curved lines in the non-linear case. This means that non-linear permeability makes the concentrated magnetic flux spread out over the domain.

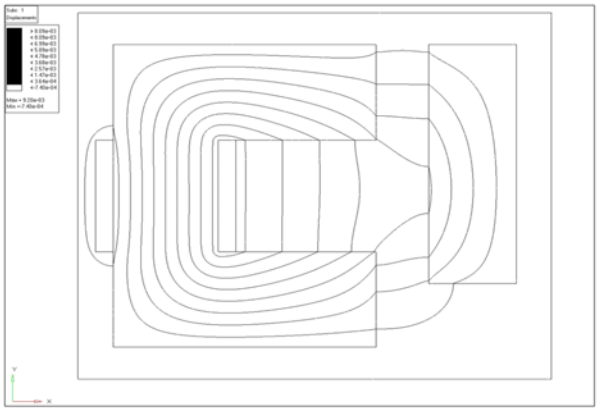

(a)

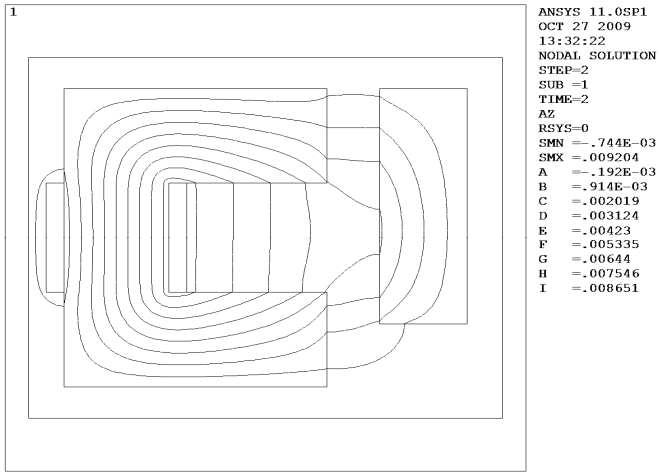

(b)

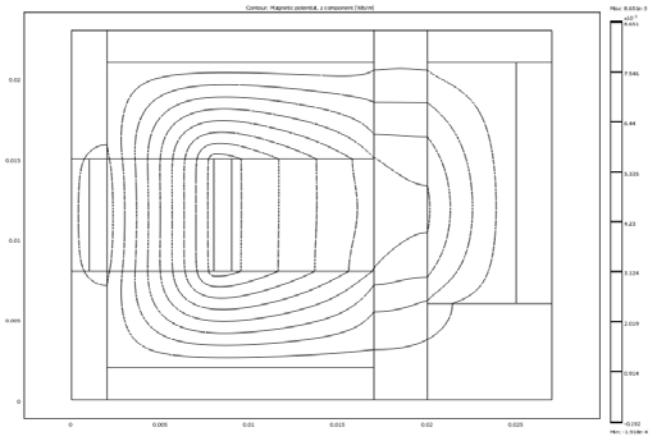

(c)

Figure 2.8.4. Equipotential lines of vector potential **A** in 2D non-linear case (b) Developed Program, (b) ANSYS, (c) COMSOL

Table 2.8.4 shows the magnetic energy W_f obtained from each finite element program. In the non-linear problem, the magnetic energy W_f can be written as

$$W_f = \int_V \left(\int_0^B H \, dB \right) dV \tag{2.8.3}$$

The energy from the developed program and ANSYS is exactly the same, but the result of COMSOL is different from other results. This might be because COMSOL mistakenly calculates the magnetic energy of non-linear problem using Eq. (2.8.2), that is, the energy of linear problem. When we use Eq. (2.8.2) in the developed program, we obtained the energy as 14.533, which is exactly the same quantity as the result of COMSOL.

Table 2.8.5 and Table 2.8.6 compares the magnetic vector potential **A** and the magnetic flux density **B** at specific nodes and elements, respectively. The results from all finite element programs are almost identical, and therefore, the developed program is verified for two dimensional non-linear magnetostatic analysis.

Table 2.8.4. Comparison of magnetic energy $W_f(J)$ – 2D non-linear case

	Developed Program	**ANSYS**	**COMSOL**
Magnetic energy W_f	14.325	14.325	14.533

Table 2.8.5. Comparison of vector potential **A** (*Wb/m*) – 2D non-linear case

Node Number	**814**	**1256**	**4360**
Developed Program	0.177337E-02	0.217659E-03	0.778278E-02
ANSYS	0.17734E-02	0.21763e-03	0.77827E-02
COMSOL	0.177336E-02	0.217659E-3	0.778284E-02

Table 2.8.6. Comparison of magnetic flux density **B** (Wb/m^2)) – 2D non-linear case

Node Number		**1274**	**6041**	**14090**	**6236**
Developed Program	B_x	-0.936867	-0.968096	-0.968096	-0.936867
	B_y	0.765458	0.765458	0.7342295	0. 7342295
ANSYS	B_x	-0.93688	-0.96811	-0.96811	-0.93688
	B_y	0.76547	0.76547	0.73424	0.73424
COMSOL	B_x	-0.936854	-0.968083	-0.968083	-0.936854
	B_y	0.765449	0.765449	0.734219	0.734219

2.8.3. 3D Linear model

Three dimensional analysis of the magnetic actuator is performed when the **B-H** relation is linear. Both nodal and edge elements are used for the three dimensional analysis. The magnetic flux density **B** at the center plane in the z-direction and the magnetic energy W_f over the whole domain are compared to verify the developed program. The location of the center plane is shown in Figure 2.8.5 as black elements.

Figure 2.8.6 and Figure 2.8.7 show the magnetic flux density **B** distribution at the center plane when the nodal and edge element is used for the analysis, respectively. The COMSOL nodal element result is not shown because it uses only the edge element for three dimensional magnetostatic analysis. The result of the ANSYS nodal element shown in Figure 2.8.6(b) is totally different from other results and looks physically unreasonable. The ANSYS low-frequency electromagnetic nodal element (SOLID97 element) always applies the gauge condition. This condition might be the reason for the error in the result. As already explained in chapter 2.6, modification of the functional for the gauge condition in the nodal element can cause serious error. The other results, except that using ANSYS nodal element, are reasonably similar to each other. The comparison of the nodal values is not shown because of the difficulty of picking an element or node inside three dimensional models.

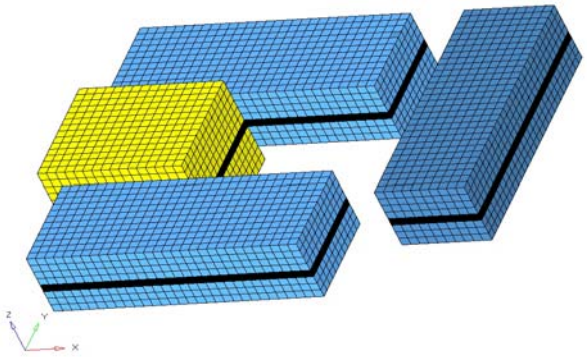

Figure 2.8.5. Location of plane for magnetic flux density **B** contour

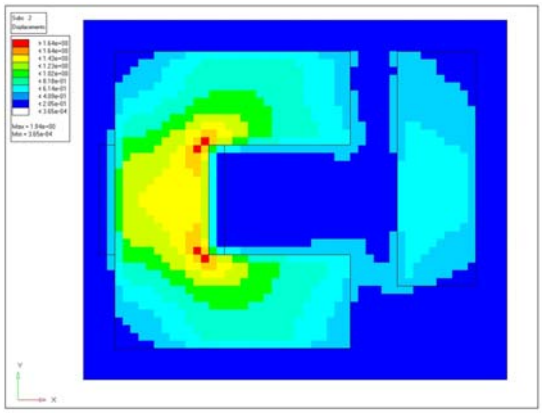

(a)

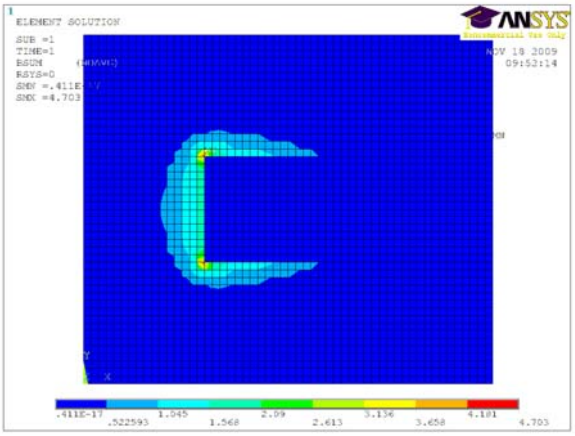

(b)

Figure 2.8.6. Magnetic flux density **B** – 3D linear case using nodal element

(a) Developed Program, (b) ANSYS

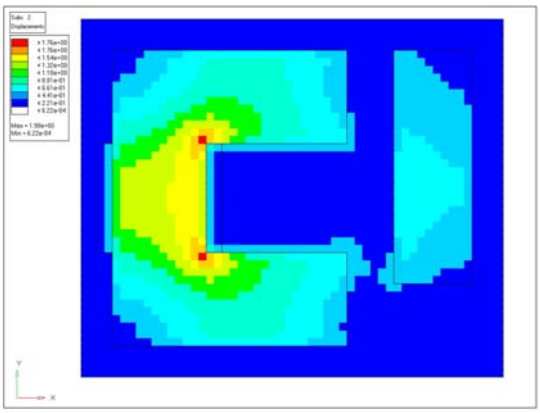

(a)

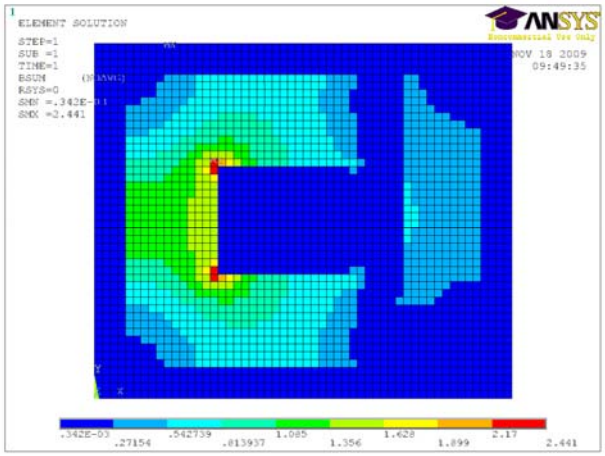

(b)

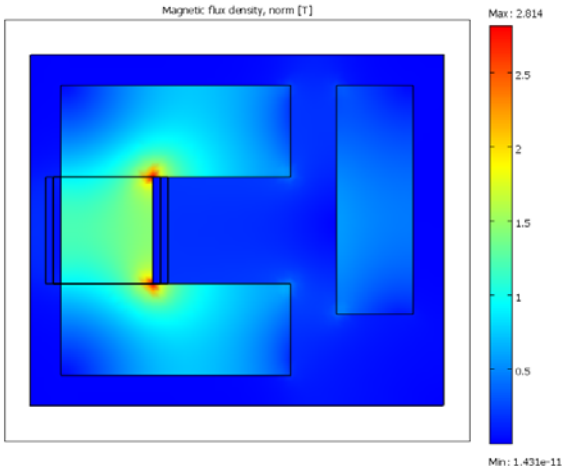

(c)

Figure 2.8.7. Magnetic flux density **B** – 3D linear case using edge element

(a) Developed Program, (b) ANSYS, (c) COMSOL

Table 2.8.7 compares the magnetic energy W_f calculated from various programs. The energy from the ANSYS nodal element is totally different from other results. This error is expected as can be seen in the error of the magnetic flux density **B** distribution. In the edge element case, the energy of the developed program is almost the same as that of COMSOL and slightly different (less than 0.6%) with that of ANSYS. ANSYS edge element (SOLID117 element) always applies the tree-cotree gauging. This might be the reason for the slight difference in the energy result. Nodal and edge elements give a similar magnetic energy; they are different less than 3%.

To check the boundary conditions, some nodes at the interface of steel and air are picked, and the normal magnetic flux density B_n and two tangential field intensities H_{t1} and H_{t2} at the node are compared in Table 2.8.8. As already explained in section 2.6, these fields should be continuous even at the different material interface. Because the magnetic vector potential method is used, the B_n continuity condition is automatically satisfied in both nodal and edge elements. The edge element satisfies H_{t1} and H_{t2} continuity conditions to some extent, but the nodal element does not satisfy the conditions as expected. This comparison confirms that the nodal element gives an error on the magnetic field at different material interfaces, while the edge element can give more accurate magnetic field solutions.

In conclusion, we might say that the ANSYS nodal element is not recommended for three dimensional linear magnetostatic problems and the developed program gives reasonable results in both nodal and edge elements. If our interest is the magnetic energy over the whole domain, both nodal and edge elements can be used, but the nodal element is not recommended if we need accurate field solutions at different material interfaces.

Table 2.8.7. Comparison of magnetic energy $W_f(J)$ – 3D linear case

	Developed Program	**ANSYS**	**COMSOL**
Magnetic energy W_f (Nodal Element)	1.5339×10^{-2}	0.5303×10^{-2}	
Magnetic energy W_f (Edge Element)	1.4924×10^{-2}	1.4835×10^{-2}	1.4925×10^{-2}

Table 2.8.8. Boundary conditions at the interface of steel and air

	Nodal Element		**Edge Element**	
	Steel	**Air**	**Steel**	**Air**
B_n	-0.20199	-0.20199	-0.19167	-0.19167
H_{t1}	-568.950	- 7368.444	-506.553	-928.098
H_{t2}	6.34963×10^{-9}	1.27312×10^{-6}	-2.0679×10^{-3}	3.72333×10^{-3}

2.8.4. 3D Non-linear model

Three dimensional analysis of magnetic actuator is performed when the **B-H** relation is non-linear. Both nodal and edge elements are used for the analysis. The magnetic flux density **B** at the center plane and the magnetic energy W_f over the whole domain are compared to verify the developed program.

Figure 2.8.8 and Figure 2.8.9 show the magnetic flux density **B** distribution at the center plane when the nodal or edge element is used for the analysis, respectively. All results except the ANSYS nodal element are similar. A huge error in the ANSYS nodal element might be due to the gauge condition, which is already shown in the linear result.

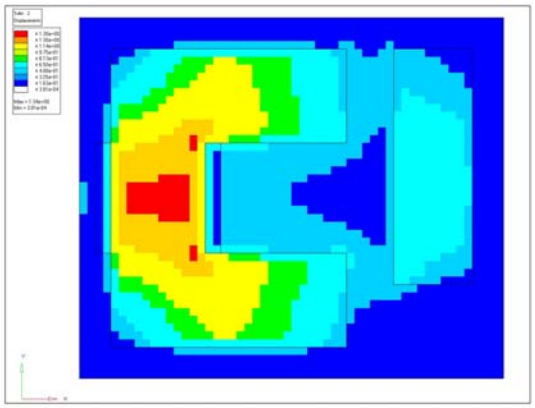

(a)

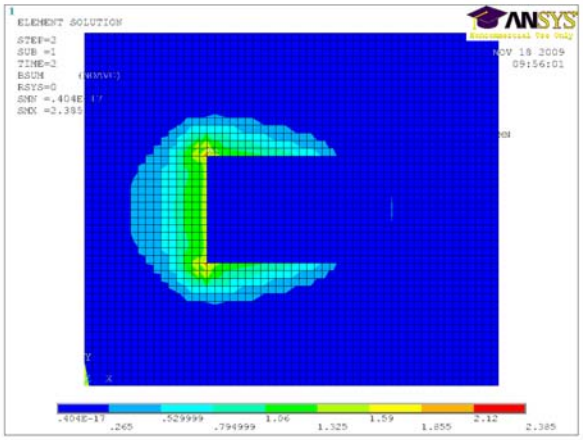

(b)

Figure 2.8.8. Magnetic flux density **B** – 3D non-linear case using nodal element
(a) Developed Program, (b) ANSYS

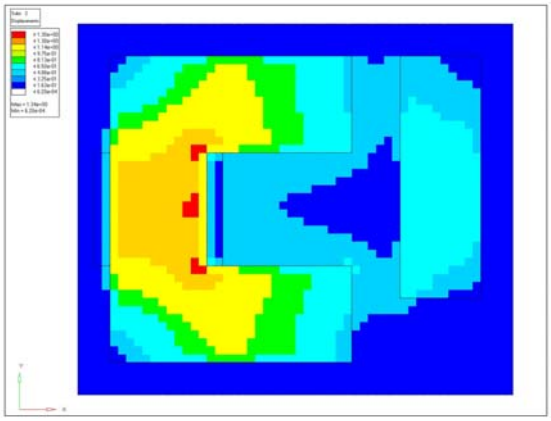

(a)

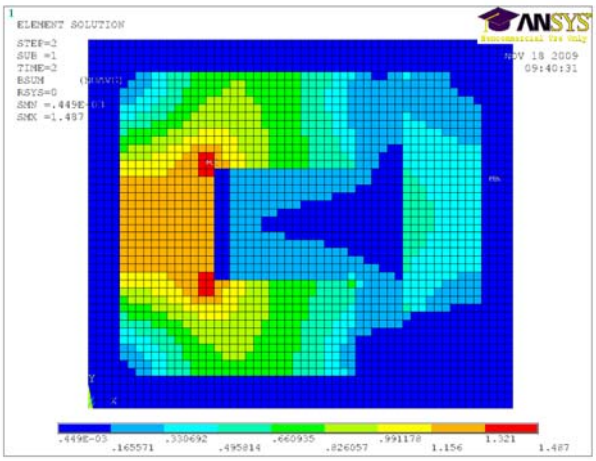

(b)

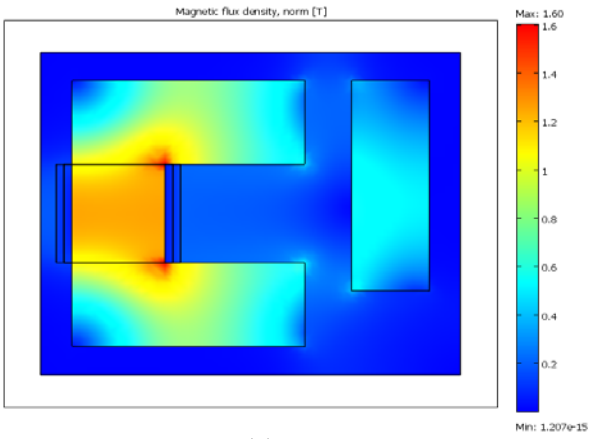

(c)

Figure 2.8.9. Magnetic flux density **B** – 3D non-linear case using edge element
(a) Developed Program, (b) ANSYS, (c) COMSOL

Table 2.8.9 compares the magnetic energy W_f calculated from various programs. The energy from the ANSYS nodal element is totally different from other results as expected. In the edge element result, the energy from COMSOL is different from that of the developed program. The reason for this difference might be the same as that with two dimensional problems. COMSOL mistakenly calculates the magnetic energy of non-linear problem using Eq. (2.8.2), that is, the energy of linear problem. When we use Eq. (2.8.2) in the developed program, we obtained the energy as 1.4798×10^{-2}, which is almost the same quantity as the result of COMSOL. The difference between ANSYS and the developed program in the edge element result is less than 0.6% and it might be due to the tree-cotree gauging.

In conclusion, we might say that the ANSYS nodal element is not recommended for three dimensional non-linear problems as well, and the developed program gives reasonable results for this problem.

Table 2.8.9. Comparison of magnetic energy $W_f(J)$ – 3D non-linear case

	Developed Program	**ANSYS**	**COMSOL**
Magnetic energy W_f (Nodal Element)	1.4475×10^{-2}	0.5260×10^{-2}	
Magnetic energy W_f (Edge Element)	1.4733×10^{-2}	1.4644×10^{-2}	1.4801×10^{-2}

2.9. Conclusions

The finite element method for magnetostatic analysis is presented in this chapter. The Maxwell's equations describing the behavior of electromagnetic fields are modified to the equations for the magnetostatic case, where the current generates a magnetic field and all fields do not vary with the time. To solve the derived magnetostatic equation, we present two potential methods: scalar potential and vector potential methods. The strength and weakness of each potential method are described, and the guideline to choose a potential method is presented. Then, we explain a gauge condition to solve the uniqueness problem, which has been one of the important issues in magnetostatic analysis using the potential method. Next, the finite element formulation is described for the 2D linear problem, the 3D linear problem and the problem for the non-linear **B-H** relation. The 3D problem can be solved using either the nodal or edge finite element considering two continuous boundary conditions. The non-linear magnetostatic problem is solved using the Newton-Raphson iteration method. From the explained finite element formulation, a program is developed for the magnetostatic analysis, and the developed program is applied to analyze the 2D/3D linear/non-linear magnetic actuator. The developed program is verified by comparing the analysis result with that using COMSOL and ANSYS.

CHAPTER 3
MAGNETIC FORCE CALCULATION

3.1. Introduction

This chapter shows how to calculate magnetic force on a ferromagnetic material. Force calculation is an essential procedure in the analysis of electric machines because they are designed to move or rotate an object such as an actuator armature or machine stator/rotor. There are two different types of forces in the aspect of electric machine analysis: global (total) force, and local (distributed) force [78, 81, 93, 99]. Global force is single net force acting on an object, whereas local force is a distribution of forces acting at specific places on an object. In general, calculating a global force is simpler than calculating a local force. If the interest is placed only on the operational total force on the rigid moving object, a global force calculation may be enough. However, the calculation of a local force distribution is necessary for the noise and vibration analysis of electric machines. This chapter describes the various methods to calculate both global and local forces.

A lot of research has been conducted to find a accurate and reliable force calculation methods for electric machines [105-119]. Popular methods for the force calculation based

on finite element field solutions are as follows: (a) Maxwell stress tensor method, (b) virtual work method, (c) equivalent source method. All of these methods can calculate both global and local force. It is shown that all methods provide almost the same global force. However, each method gives a different local force distribution. These different results raise questions about which method provides true force distribution.

Recently, a new local force calculation method is developed using a virtual air-gap scheme [120-122] derived from the generalized equivalent source method [123, 124]. The developed method determines successfully the magnetic force of electric machines [125]. This method calculates body force as a local force distribution while the conventional method provides the surface force. It asserts that the body force is not zero when the magnetic field inside the body is not uniform. In addition, it tries to show the similarity between the magnetic force and the gravitational force, applied to the body. It is shown that this new method provides the unique local force distribution regardless of the force calculation methods. We are not sure whether one of the surface force results is true or the body force distribution is true. However, we can be sure that the analysis and design result for the structural and vibration problems will be totally different due to the difference in surface and body force as a local force distribution.

This chapter investigates both the conventional method and the new method using the virtual air-gap concept. The outline of this chapter is as follows. Section 3.2-3.4 explains three conventional methods: Maxwell stress tensor method, virtual work method, and the equivalent source method. The body force calculation method using the virtual air-gap scheme is presented in section 3.5. In section 3.6, all the force calculation methods are investigated using numerical examples. Finally, section 3.7 summarizes this chapter.

3.2. Maxwell stress tensor method

The Maxwell stress tensor method is one of the most efficient and popular methods. Calculation of both the global and local force is available. This method enables us to calculate the magnetic force simply from a single finite element field solution. This might be the reason why this method become so popular.

The Maxwell stress tensor method can be derived from the fact that the ferromagnetic material may be replaced by air with a distribution of surface currents $\mathbf{J}_s$ and volume currents $\mathbf{J}_v$. After the replacement, the magnetic field is represented by the modified Ampere's circuital law:

$$\nabla \times \left(\frac{1}{\mu_0} \mathbf{B} \right) = \mathbf{J} + \mathbf{J}_s + \mathbf{J}_v \tag{3.2.1}$$

where μ_0 is the permeability of the air.

Then, the magnetic force can be calculated using Lorentz volume force density, which can be written as

$$\mathbf{f}_v = \left(\mathbf{J} + \mathbf{J}_s + \mathbf{J}_v \right) \times \mathbf{B} \tag{3.2.2}$$

From Eq. (3.2.1) and (3.2.2), the magnetic force $\mathbf{f}_v$ can be expressed as the divergence of a tensor.

$$\mathbf{f}_v = \nabla \cdot \boldsymbol{\tau} \tag{3.2.3}$$

The tensor $\boldsymbol{\tau}$ is called as the Maxwell stress tensor. In two dimensional problems with the linear **B-H** relation, the stress tensor $\boldsymbol{\tau}$ is derived as

$$\boldsymbol{\tau} = \frac{1}{\mu_0}\begin{bmatrix} B_x{}^2 - \frac{1}{2}|B|^2 & B_x B_y & B_x B_z \\ B_y B_x & B_y{}^2 - \frac{1}{2}|B|^2 & B_y B_z \\ B_z B_x & B_z B_y & B_z{}^2 - \frac{1}{2}|B|^2 \end{bmatrix} \tag{3.2.4}$$

The derivation of $\boldsymbol{\tau}$ is straightforward, and therefore it is not shown here. In a tensor notation, the stress tensor τ_{ij} can be written as

$$\tau_{ij} = \frac{1}{\mu_0} B_i B_j - \delta_{ij}\left(\frac{1}{2\mu_0} B_k B_k\right) \quad (i, j, k = 1,2) \tag{3.2.5}$$

The stress tensor for the non-linear **B-H** relation is derived in [105] and written as

$$\tau_{ij} = \frac{1}{\mu} B_i B_j - \delta_{ij}\left(\int_0^B \frac{1}{\mu}\tilde{B} d\tilde{B}\right) \quad (i, j = 1,2) \tag{3.2.6}$$

The integration in the second term of Eq. (3.2.6) describes the nonlinearity due to magnetic saturation.

Finally, the global force is calculated by integrating the volume force density $\mathbf{f}_v$. From the divergence theorem, the volume integration is transformed to surface integration. Therefore, the global force can be written as

$$\mathbf{F}_{total} = \int_V \nabla \cdot \boldsymbol{\tau} \, dV = \oiint_A \boldsymbol{\tau} \cdot d\mathbf{A} \tag{3.2.7}$$

where the **A** is any close surface surrounding the object, which is called the integration path.

The local force distribution can be obtained by adjusting the integration path of the Maxwell stress tensor method. The global force expressed in Eq. (3.2.7) contains the surface integration of some function. This function can be thought of as the local force distribution along the surface. In a strict mathematical sense, this function cannot be a local force distribution because the surface integration is mathematically derived using the divergence theorem. It only means that the global force using the volume integration is identical with that using the surface integration. It does not mean that the distribution is also identical. However, this local force distribution is frequently used for practical applications because it gives a reasonable force distribution.

In the Maxwell stress tensor method, the force formulation of the non-linear problem becomes identical with that of linear problem if the integration path is not on the non-linearly magnetized object. This is because the integration is taken only at the air region,

which has a constant permeability μ_0. If permeability μ in Eq. (3.2.6) is constant as air permeability μ_0, Eq. (3.2.6) becomes identical with Eq. (3.2.5), that is, the stress tensor in a linear **B-H** relation. Therefore, the same force formulation using Eq. (3.2.5) at the air integration path is available for both linear and non-linear problems. For the non-linear problem, we only need to consider that the final converged quantity of the magnetic flux density **B** should be used.

In practical applications, forces in the normal and tangential directions are more preferred than those expressed in the Cartesian coordinate. In two dimensional cases, the relation between unit vectors in Cartesian coordinates and normal/tangential coordinate can be represented as

$$\mathbf{n} = -\mathbf{i}\sin\theta + \mathbf{j}\cos\theta \tag{3.2.8}$$

$$\mathbf{t} = \mathbf{i}\cos\theta + \mathbf{j}\sin\theta \tag{3.2.9}$$

where **i** and **j** are x and y directional unit vectors in Cartesian coordinates, **n** and **t** are normal and tangential unit vectors, and θ is the angle between the surface line and x direction. From the above relation, the global force Eq. (3.2.7) can be derived for the normal and tangential direction, which can be written as

$$\mathbf{F}_{total} = \left[\oint_A \frac{1}{2\mu_0}(B_n{}^2 - B_t{}^2)\, dA \right] \mathbf{t} + \left[\oint_A \frac{1}{\mu_0} B_n B_t \, dA \right] \mathbf{n} \tag{3.2.10}$$

In the Maxwell stress tensor method, the selection of the integration path is critical for the accuracy problem. Although the integration path is theoretically arbitrary, the path strongly influences the result. This is because the result is calculated only with the magnetic flux density **B** on the integration path, and this value is correct only at the Gaussian integration point and has large error particularly at finite element nodes. Therefore, the flux density **B** calculated at Gaussian integration points can be used for magnetic force calculation at the integration path. It is known that the difficulty in the integration path makes trouble in implementing the Maxwell stress tensor method for three dimensional problems.

3.3. Virtual work method

The virtual work method is based on the principle of conservation of energy or co-energy and the principle of virtual displacement. The magnetic energy W_f and the co-energy W_{co} is defined as

$$W_f = \int_V \left(\int_0^B H \, dB \right) dV \tag{3.3.1}$$

$$W_{co} = \int_V \left(\int_0^H B \, dH \right) dV \tag{3.3.2}$$

This method calculates the magnetic force as the derivative of the energy W_f with respect to position at constant flux linkage Φ or the co-energy W_{co} with respect to the position at constant current i. Therefore the global force for α direction can be written as

$$F_{tot} = -\frac{\partial W_f}{\partial \alpha}\Big|_{\Phi=\text{constant}} \tag{3.3.3}$$

$$F_{tot} = \frac{\partial W_{co}}{\partial \alpha}\Big|_{i=\text{constant}} \tag{3.3.4}$$

It is known that the virtual work method is well suited to finite element analysis because the finite element solution is formulated using minimized stored magnetic energy W_f [115]. In addition, this method is less sensitivity to the errors of magnetic flux density because it uses the global quantity obtained from the volume integral. The virtual work method is classified into: (a) global (classical) virtual work method, and (b) local (Coulomb) virtual work method.

Global (Classical) virtual work method

The global virtual work method calculates Eq. (3.3.4) using the total magnetic co-energy W_{co} of the system when its moving part is physically displaced in the direction of the required component of force. In this method, not Eq. (3.3.3), but Eq. (3.3.4) is chosen because the constant current condition is more efficient for developing finite element codes than the flux linkage constant condition. In this method, the partial derivative of the equation can be evaluated using a finite difference approximation. For the finite difference calculation of the derivative, at least two finite element solutions are required when the component on which we want to compute the force is slightly moved with the constant current.

Instead of the finite difference approximation, a curve fitting can be used to approximate the total co-energy W_{co} function with respect to the location of the object in the α direction. The co-energy function W_{co} using a curve fitting can be easily differentiated, and then, the magnetic force can be obtained using Eq. (3.3.4). The curve fitting method is particularly convenient in the problem where the object moves in only one direction like a rotating electric machine.

The biggest disadvantage of the global virtual work method is that it requires more than two finite element solutions with different meshes, which increase the computation cost. In addition, the result using finite difference approximation may suffer from cancellation error. The co-energy quantities of two closed positions are usually very close. The subtraction of two close large quantities and the division of two small quantities can cause significant error in the result. Another disadvantage is that calculating the local force distribution is not available practically, as can be seen in the name of the "global" virtual work method. The slight movement of one element may give the local force acting on that element. However, the movement of every element in the finite element model is very inefficient and impossible practically.

Local (Coulomb) virtual work method

The local virtual work method is based on the same concept as the global virtual work method; that is, it also calculates the force using Eq. (3.3.3) or (3.3.4). However, in the local virtual work method, the derivative is evaluated by direct, closed form differentiation of the magnetic energy W_f or co-energy W_{co}. The advantage of this method

is that it requires only one finite element solution like the Maxwell stress tensor method. In addition, the local force distribution can be obtained using this method.

This method first calculates the local force associated with a node. As can be seen in Figure 3.3.1, a single node *j* moves in the direction of the required force component, while the other nodes remain fixed. Then, the local force is calculated by the direct differentiation of the magnetic energy or co-energy. The element directly connected with node *j* only contributes to the local force for that node. The calculated force is assumed to be applied in the half line between node *i* and *k*, which has the length as (length of *ij* + length of *jk*) / 2. After calculating the local force distribution, the global force can be calculated by summing the local force. It should be noted that the local force is not zero only at the nodes located at the interface of air and steel.

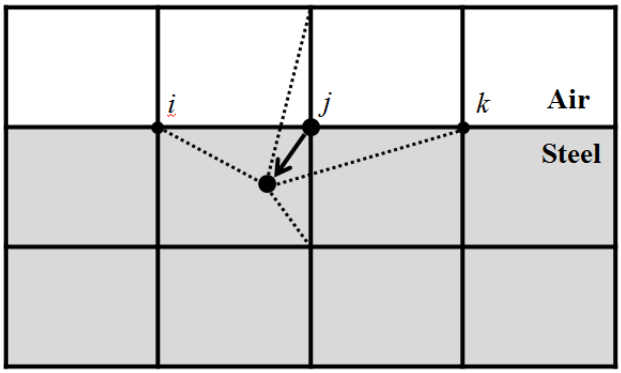

Figure 3.3.1. Movement of a node in the local virtual work method

To apply the local virtual work method, Eq. (3.3.3) is more convenient if the vector potential **A** method is used because the fixed constant linkage Φ means fixed magnetic flux density **B**, and therefore, fixed vector potential **A**. If the scalar potential Ω is used,

Eq. (3.3.4) is more convenient because fixed current i means fixed magnetic field intensity **H**, and therefore, fixed scalar potential Ω. The fixed unknowns in each case make it simple to derive the direct analytical differentiation in Eq. (3.3.3) or (3.3.4).

In two dimensional linear problems using vector potential **A** method, the local force at a node i in α direction can be derived from the analytical differentiation of Eq. (3.3.3), and can be derived as

$$F_i = -\frac{1}{2\mu} A_z^{\mathrm{T}} \frac{\partial \mathbf{S}}{\partial \alpha_i} A_z \tag{3.3.5}$$

$$\begin{aligned} \frac{\partial \mathbf{S}}{\partial \alpha_i} = & \iint \begin{pmatrix} \dfrac{\partial N_p}{\partial r} \\ \dfrac{\partial N_p}{\partial s} \end{pmatrix}^T \mathbf{J}^{-T}\mathbf{J}^{-1} \begin{pmatrix} \dfrac{\partial N_q}{\partial r} \\ \dfrac{\partial N_q}{\partial s} \end{pmatrix} \frac{\partial |\mathbf{J}|}{\partial \alpha_i} \, dr\, ds \\ & - 2\iint \begin{pmatrix} \dfrac{\partial N_p}{\partial r} \\ \dfrac{\partial N_p}{\partial s} \end{pmatrix}^T \mathbf{J}^{-T}\mathbf{J}^{-1} \frac{\partial \mathbf{J}}{\partial \alpha_i} \mathbf{J}^{-1} \begin{pmatrix} \dfrac{\partial N_q}{\partial r} \\ \dfrac{\partial N_q}{\partial s} \end{pmatrix} |\mathbf{J}| \, dr\, ds \end{aligned} \tag{3.3.6}$$

where N_p and N_q are the shape functions of finite element formulation, and **J** is the Jacobian matrix for the coordinate change using an isoparametric element. The derivative of Jacobian matrix **J** and its determinant |**J**| is written as

$$\frac{\partial \mathbf{J}}{\partial \alpha_i} = \begin{pmatrix} \dfrac{\partial N_p}{\partial r} \\ \dfrac{\partial N_q}{\partial s} \end{pmatrix} \begin{pmatrix} \dfrac{\partial X_p}{\partial \alpha_i} & \dfrac{\partial Y_q}{\partial \alpha_i} \end{pmatrix} \tag{3.3.7}$$

$$\begin{aligned} \frac{\partial |\mathbf{J}|}{\partial \alpha_i} = & \left(\frac{\partial X_p}{\partial \alpha_i} \frac{\partial N_p}{\partial r} \right) \left(Y_q \frac{\partial N_q}{\partial s} \right) + \left(X_p \frac{\partial N_p}{\partial r} \right) \left(\frac{\partial Y_q}{\partial \alpha_i} \frac{\partial N_q}{\partial s} \right) \\ & - \left(\frac{\partial X_p}{\partial \alpha_i} \frac{\partial N_p}{\partial s} \right) \left(Y_q \frac{\partial N_q}{\partial r} \right) - \left(X_p \frac{\partial N_p}{\partial s} \right) \left(\frac{\partial Y_q}{\partial \alpha_i} \frac{\partial N_q}{\partial r} \right) \end{aligned} \tag{3.3.8}$$

where X_p and Y_p are the node locations in x and y coordinates.

In two dimensional problems with non-linear **B-H** relation, the local force can be derived as

$$\mathbf{F}_i = -\int \left(\int_0^B \frac{1}{\mu\left(b^2\right)} b\, db \right) \cdot \frac{\partial |\mathbf{J}|}{\partial \alpha_i} dV_{rst} + \int \left\{ \frac{1}{\mu\left(b^2\right)} A_{zi} A_{zj} \begin{pmatrix} \dfrac{\partial N_i}{\partial r} \\ \dfrac{\partial N_i}{\partial s} \end{pmatrix}^T \mathbf{J}^{-T} \mathbf{J}^{-1} \frac{\partial \mathbf{J}}{\partial \alpha_i} \mathbf{J}^{-1} \begin{pmatrix} \dfrac{\partial N_i}{\partial r} \\ \dfrac{\partial N_i}{\partial s} \end{pmatrix} \right\} \cdot |\mathbf{J}| dV_{rst} \tag{3.3.9}$$

The integration $\left(\int_0^B \frac{1}{\mu\left(b^2\right)} b\, db \right)$ in the first term describes the non-linearity. If we change the permeability $\mu(b^2)$ to a constant one, the above formulation for non-linear problems becomes identical with Eq. (3.3.5) and Eq. (3.3.6), which apply to linear problem. The detailed derivation of the above equations is described in [118, 126]. It should be noted that the local virtual work method requires integration at the magnetic material, which adds considerable complexity to the force calculation of the non-linear

problem. The formulation for three dimensional problems is almost identical with those for two dimensional problems and not described here.

3.4. Equivalent source method

This method is based on replacing ferromagnetic material by a non-magnetic one with a superficial distribution of equivalent field sources: (a) equivalent currents, (b) equivalent charges.

To derive the equivalent source method, we need the relation between the magnetization **M** and the magnetic field. When the magnetic field is applied on the magnetic material, a net alignment of magnetic dipoles occurs and the medium becomes magnetically polarized. The amount of magnetic polarization can be described as the magnetization **M**, which is a magnetic dipole moment per unit volume. The relation between the magnetization **M** and the magnetic field **B** or **H** at the interface of magnetic material m1 with permeability $\mu_0\mu_r$ and non-magnetic material m2 with permeability μ_0 can be written as

$$M_{nm1} = H_{nm2} - H_{nm1} \tag{3.4.1}$$

$$M_{tm1} = \frac{1}{\mu_0}\left(B_{tm1} - B_{tm2}\right) \tag{3.4.2}$$

The equations (3.4.1)-(3.4.2) are identical conditions with the continuous normal magnetic flux density **B**, and tangential field intensity **H**, which is the well known

interface conditions shown in Eq. (2.6.5)-(2.6.6). These two equations will be used to derive the magnetic force using the equivalent source method.

Equivalent currents

The surface current $\mathbf{J}_s$, due to the magnetization $\mathbf{M}$ of material 1 can be written as

$$\mathbf{J}_s = \mathbf{M}_1 \times \mathbf{n} \tag{3.4.3}$$

From Eq. (3.4.1)-(3.4.2), the surface current $\mathbf{J}_s$ can be written as

$$\mathbf{J}_s = \frac{1}{\mu_0}\left(B_{2t} - B_{1t}\right)\left(\mathbf{t} \times \mathbf{b}\right) \tag{3.4.4}$$

The local force of the non-magnetic material with the surface current $\mathbf{J}_s$ can be calculated using Lorentz law:

$$\mathbf{F}_s = \mathbf{J}_s \times \mathbf{B}_s \tag{3.4.5}$$

From Eq. (3.4.4)- (3.4.5), the normal and tangential component of local force at the surface of magnetic material can be written as

$$\mathbf{F}_s = \left[\frac{\mu_0}{2} \left(\mu_r{}^2 - 1 \right) H_t{}^2 \right] \mathbf{n} + \left[\left(1 - \mu_r \right) B_n H_t \right] \mathbf{t} \tag{3.4.6}$$

The above local force is expressed using the continuous component B_n and H_t at the interface of magnetic material and non-magnetic material. The global force can be obtained by summing the calculated local force.

Equivalent charges

The surface charge ρ_s due to the magnetization **M** of material 1 can be written as

$$\rho_s = \mu_0 \, \mathbf{n} \cdot \mathbf{M}_1 \tag{3.4.7}$$

From Eq. (3.4.1)-(3.4.2), the surface current ρ_s can be written as

$$\rho_s = B_{2n} - \frac{1}{\mu_r} B_{1n} \tag{3.4.8}$$

The local force distribution by the surface charge can be written from Coulomb's law as

$$\mathbf{F}_s = \rho_s \mathbf{H}_s \tag{3.4.9}$$

From Eq. (3.4.8)- (3.4.9), the normal and tangential component of local force distribution at the surface of magnetic material can be derived as

$$\mathbf{F}_s = \left[\frac{1}{2\mu_0}\left(1-\mu_r^{\,2}\right)B_n^{\,2} \right]\mathbf{n} + \left[\left(1-\frac{1}{\mu_r} \right) B_n H_t \right]\mathbf{t} \qquad (3.4.10)$$

The above local force is expressed using the continuous component B_n and H_t at the interface of magnetic material and non-magnetic material. The global force can be obtained by summing the calculated local force.

The equivalent source method can be also used for the problem with the non-linear **B-H** relation. Nonlinear reluctivity μ does not affect the derivation of the equivalent source method. We only need to consider that the final converged magnetic field and the relative permeability μ_r should be used for the calculation.

3.5. Body force calculation method

This section describes a rather new method for calculating both local and global magnetic forces. This method gives the local force distribution as the body force, which is different from the surface force given by the conventional methods described in section 3.2-3.4. The global force is simply obtained by summing the local force distribution. In this method, the object is split into a number of small bodies. Then, the magnetic force applied to the small bodies is calculated using the conventional methods

described in chapter 3.2-3.4. The conventional methods are defined only in the object surrounded by the air. Therefore, a virtual air gap is inserted between the small bodies contacting each other. At the virtual air gap, the magnetic flux density **B** and magnetic field intensity **H** is derived using the equivalent source method. Then the conventional methods can be used to calculate the magnetic force of the small bodies contacting each other. Finally, the body force is obtained by dividing the magnetic force applied to the small bodies by their volume. The finite elements are chosen as the small bodies because the finite element method is used for the magnetic field calculation.

The magnetic flux density **B** and the magnetic field intensity **H** at the virtual air gap are derived using the generalized equivalent current method [123] and generalized equivalent charge method [124] respectively. It is shown that the magnetic field **B** and **H** at the virtual air gap between material 1 and 2 is same as the field satisfying the boundary condition between material 1 and the airgap and also between material 2 and the airgap. The detailed formulation of generalized equivalent methods and the derivation of the magnetic field at the virtual air gap are shown in [120, 121].

The boundary conditions at the virtual air gap are written as

$$B_{na} = B_{n1} = B_{n2} \tag{3.5.1}$$

$$H_{ta} = H_{t1} = H_{t2} \tag{3.5.2}$$

From these conditions, the magnetic flux density $\mathbf{B}_a$ and field intensity $\mathbf{H}_a$ at the air gap can be written as

$$\mathbf{B}_a = B_{n1}\mathbf{n} + \frac{B_{t1}}{\mu_{r1}}\mathbf{t} = B_{n2}\mathbf{n} + \frac{B_{t2}}{\mu_{r2}}\mathbf{t} \tag{3.5.3}$$

$$\mathbf{H}_a = \mu_{r1}H_{n1}\mathbf{n} + H_{t1}\mathbf{t} = \mu_{r2}H_{n2}\mathbf{n} + H_{t2}\mathbf{t} \tag{3.5.4}$$

where μ_1 and μ_2 are the relative permeability of material 1 and 2 respectively. Because these two magnetic fields at the virtual air gap satisfy the boundary condition as if it is a real air gap, these fields also satisfy the constitutive relation in the air material.

$$\mathbf{B}_a = \mu_0\mathbf{H}_a \tag{3.5.5}$$

After obtaining the magnetic field at the virtual air gap, the magnetic force at a finite element surrounded by the virtual air gap can be calculated using the conventional force calculation method. Then, the body force acting on a finite element is calculated by dividing the magnetic force by the finite element volume.

This method can be easily applied to calculate the magnetic force in the nonlinear **B**-**H** relation as well. The final converged magnetic field and the permeability should be considered for each finite element. The other process for the body force calculation is not different in linear and non-linear problems.

3.6. Numerical examples

In this section, numerical examples are presented to investigate the various magnetic force calculation methods. In every method except the virtual work method, an accurate magnetic field at the interface of air and ferromagnetic material is critical for accurate force calculation. As already explained, the finite element method gives inaccurate magnetic fields at the interface. To alleviate the inaccuracy, several correction methods are proposed in section 3.6.1.

The developed force calculation program is added to the finite element program as post-processing. The magnetic actuator model, which is same as that used in the section 2.8, is revisited with the same boundary conditions. In this model, the total force and local force distribution acting on the armature is calculated for both linear and non-linear problems. The permeability model for the non-linear analysis is also identical with that used in section 2.8. The global force calculation results are investigated in Section 3.6.2, and the local force distribution results are compared in section 3.6.3.

3.6.1. Correction of magnetic field at the interface

The magnetic field obtained from the first-order nodal finite element method with the potential method has considerable error at the material interface [109]. The reason for this error is already described in section 2.6. This error is ignorable in the virtual work method because it treats the magnetic energy over an element. However, this error can cause a severe inaccuracy when the magnetic field at the interface is necessary for the

magnetic force calculation. To reduce this inaccuracy, the magnetic field at the interface needs to be corrected.

Correction of the magnetic field is performed in a way that satisfies two boundary conditions at the interface. As already shown in Eq (2.6.5) and (2.6.6), the magnetic flux density **B** in the normal direction and the magnetic field intensity **H** in the tangential direction should be continuous at the interface of different materials. When the magnetic vector potential **A** method is applied, the normal flux density B_n continuity condition is automatically satisfied. However, the tangential field intensity H_t continuity condition is not met.

In the calculation of the tangential field intensity H_t at the interface, four different methods can be considered. The first two methods use either field intensity at the air element or at the ferromagnetic element without correcting the magnetic field. Next, Wignall *et. al.* [111] shows that the result using the ferromagnetic side is more accurate than that using the air side. Then, they proposed the weighted average method using the permeability of the air and the ferromagnetic material. In this method, the continuous tangential field intensity H_t can be corrected as

$$H_{t\_Wignall} = \frac{H_{t\_air}\mu_0 + H_{t\_ferr}\mu_f}{\mu_0 + \mu_f} \tag{3.6.1}$$

where μ_f is the permeability of the ferromagnetic material, H_{t_air} and H_{t_ferr} is the tangential magnetic field intensity at the interface calculated in the air side and ferromagnetic side respectively. Because the vector potential **A** method provides the

magnetic flux density **B**, the correction of **B** is more straightforward. From the constitutive relation between **B** and **H**, Eq. (3.6.1) can give two discontinuous tangential magnetic flux densities at the air side $B_{t\_air\_Wignall}$ and ferromagnetic side $B_{t\_ferr\_Wignall}$ **:**

$$B_{t\_air\_Wignall} = \frac{\mu_0}{\mu_0 + \mu_f}\left(B_{t\_air} + B_{t\_ferr}\right) \tag{3.6.2}$$

$$B_{t\_ferr\_Wignall} = \frac{\mu_f}{\mu_0 + \mu_{fl}}\left(B_{t\_air} + B_{t\_ferr}\right) \tag{3.6.3}$$

The last method for the correction of the tangential field intensity at the interface is averaging using the arithmetic mean. In this method, the continuous tangential field intensity H_t is corrected as

$$H_{t\_average} = \frac{H_{t\_air} + H_{t\_ferr}}{2} \tag{3.6.4}$$

Then, the discontinuous tangential magnetic flux densities can be written as

$$B_{t\_air\_average} = \frac{B_{t\_air} + \left(\frac{\mu_0}{\mu_f}\right)B_{t\_ferr}}{2} \tag{3.6.5}$$

$$B_{t\_ferr\_average} = \frac{\left(\frac{\mu_f}{\mu_0}\right)B_{t\_air} + B_{t\_ferr}}{2} \tag{3.6.6}$$

Figure 3.6.1 shows how each method considers the continuity condition of the tangential field intensity H_t. The Wignall and average methods connect two disconnected values (1) H_{t_air} and (2) H_{t_ferr} at the interface. For this connection, many methods might be proposed such as geometric mean and harmonic mean. However, it is not clear which connection method gives the most accurate force calculation result in every physical situation. The most straightforward method is averaging using the arithmetic mean although Wignall *et. al* shows that their method gives accurate results in some problems.

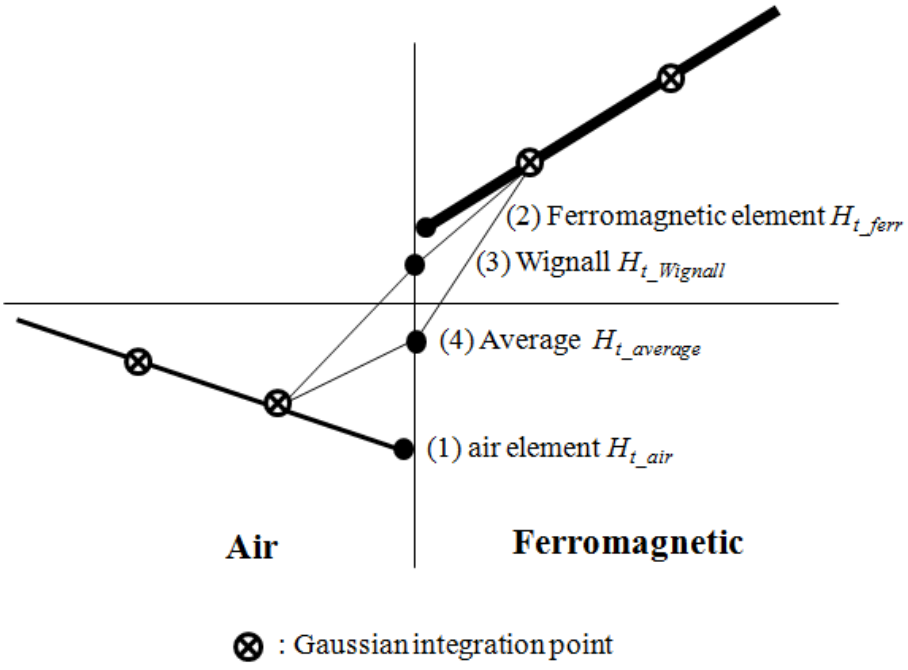

Figure 3.6.1. Various methods for correction of H_t at interface.

3.6.2. Global force comparison

The global force acting on the armature is calculated using various methods such as the Maxwell stress tensor method, the local virtual work method, the equivalent current and charge method, and the body force calculation method using the virtual air gap scheme. In the Maxwell stress tensor method, three different integration paths are considered to see how the integration path influences the force calculation result. Three integration paths are shown in Figure 3.6.2. Path 1 is on the interface of the armature and the air. Therefore, the Wignall or averaging method needs to be applied for correcting the magnetic field at the interface. For path 2 and 3, the magnetic field using the extrapolation at Gaussian integration points is used for accurate calculation [109]. The magnetic field at the interface of the air and ferromagnetic material is also required as well for the following force calculation methods: the equivalent source method and the body force calculating method using the Maxwell stress tensor and equivalent source methods. For these methods, correcting the magnetic field with the Wignall or averaging methods is used as well. Table 3.6.1 shows the x and y directional global forces acting on the armature when the **B-H** relation is linear, and the forces for the non-linear **B-H** relation are shown in Table 3.6.2.

.

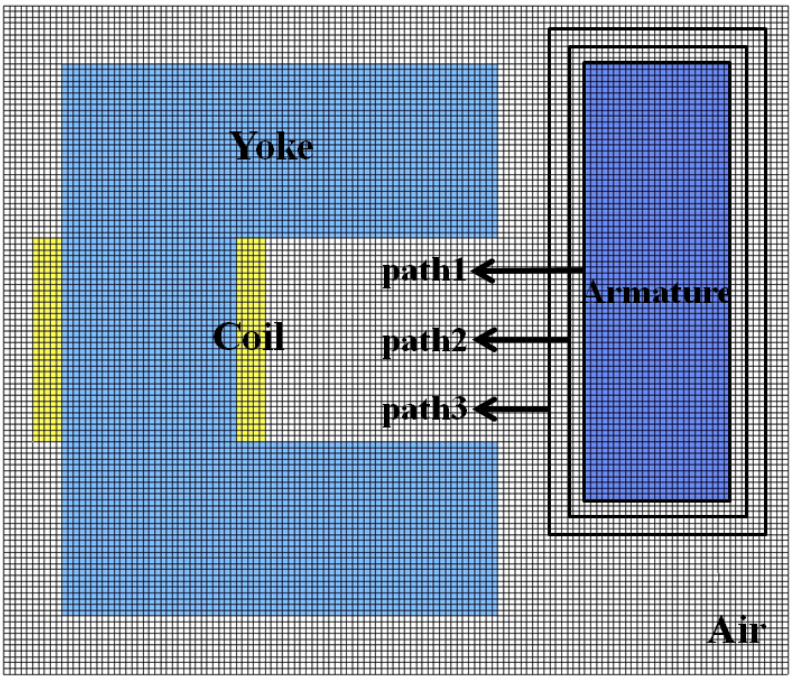

Figure 3.6.2. Three different integration paths of the Maxwell stress tensor method.

As shown in Table 3.6.1, most of methods give reasonable global forces when the **B-H** relation is linear, but the equivalent current method with the averaging method fails to calculate an accurate global force. The global force from the body force calculation method is exactly the same as that from corresponding conventional methods. This result confirms the fact that the body force calculation method does not change the global force although it gives completely different local force distributions, which are presented in [120, 121]. The global force of the local virtual work method, which is known as the most accurate method, is almost the same as those of the Maxwell stress tensor method using integration path 2, 3, and 1 with the averaging method, and the equivalent charge method with the averaging method. The difference in the above results is less than 1%. It confirms that the global force is almost the same regardless of the force calculation methods. It is noted that the result of the equivalent current method with the averaging method has a huge error although the equivalent current method with the Wignall method gives a reasonable result. When we compare the results using different correction methods, we can find that the averaging method gives more accurate results while the Wignall method gives more reliable result in this example.

Table 3.6.1. Global force on armature in linear **B-H** relation

		Wignall		Averaging	
		F_{x_global}	F_{y_global}	F_{x_global}	F_{y_global}
Conventional method	Maxwell Stress tensor (Path1)	-1498.29	-265.26	-1570.16	-302.77
	Equivalent current	-1491.08	-273.72	-1.4735×10^{7}	-8.3880×10^{6}
	Equivalent charge	-1498.29	-265.26	-1576.46	-306.36
		F_{x_global}		F_{y_global}	
	Local virtual work	-1579.97		-307.12	
	Maxwell Stress tensor (Path2)	-1573.57		-304.33	
	Maxwell Stress tensor (Path3)	-1573.44		-304.67	
Body force calculation method using virtual air gap		Wignall		Averaging	
		F_{x_global}	F_{y_global}	F_{x_global}	F_{y_global}
	Maxwell Stress tensor	-1498.29	-265.26	-1570.16	-302.77
	Equivalent current	-1491.08	-273.72	-1.4735×10^{7}	-8.3880×10^{6}
	Equivalent charge	-1498.29	-265.26	-1576.46	-306.36

Table 3.6.2 shows the global forces in the non-linear **B-H** relation. The global force of the non-linear case is about 5% less than that of the linear case. The reason for the decreased force might be the reduced magnetic field caused by the magnetic saturation effect. The equivalent current method with any of the Wignall and averaging methods fails to provide the reasonable global force again in non-linear problems. The other characteristics of each method in the non-linear case are almost same as that of the linear case. Each result with conventional methods is identical with the result of the corresponding body force calculation method. The fact that the body force calculation method does not change the global force is confirmed again for the non-linear **B-H** relation. The global force of the local virtual work method is almost the same as those of the Maxwell stress tensor method using integration path 2, 3, and 1 with the averaging method, and the equivalent charge method with the averaging method. The difference in the above results is less than 1%. It is confirmed that every global force except the equivalent current method gives similar unique global force results in the non-linear **B-H** relation.

Table 3.6.2. Global force on armature in non-linear **B-H** relation

		Wignall		Averaging	
		F_{x_global}	F_{y_global}	F_{x_global}	F_{y_global}
Conventional method	Maxwell Stress tensor (Path1)	-1437.46	-258.52	-1502.93	-291.27
	Equivalent current	-122908	-146685	-1.4871×10^{7}	-8.9711×10^{7}
	Equivalent charge	-1437.51	-258.58	-1509.30	-295.11
		F_{x_global}		F_{y_global}	
	Local virtual work	-1511.92		-295.14	
	Maxwell Stress tensor (Path2)	-1506.05		-292.70	
	Maxwell Stress tensor (Path3)	-1505.93		-293.03	
Body force calculation method using virtual air gap		Wignall		Averaging	
		F_{x_global}	F_{y_global}	F_{x_global}	F_{y_global}
	Maxwell Stress tensor	-1437.46	-258.52	-1502.93	-291.27
	Equivalent current	-122908	-146685	-1.4871×10^{7}	-8.9711×10^{7}
	Equivalent charge	-1437.51	-258.58	-1509.30	-295.11

3.6.3. Local force distribution comparison

The local force distribution acting on the armature is calculated using the various methods for both linear and non-linear cases. The distribution of the linear case is shown in Figure 3.6.3 and Figure 3.6.4, and the distribution of the non-linear case is presented in Figure 3.6.5 and Figure 3.6.6.

Figure 3.6.3 shows the surface force distribution using the conventional method in the linear problem. The force distribution of the equivalent charge method shown in Figure 3.6.3(a) is almost identical to that of the Maxwell stress tenor method shown in Figure 3.6.3(c). The distribution of the local virtual work method shown in Figure 3.6.3(d) is different from that of Figure 3.6.3(a) and (c) at the corner. This might be because the corner is a numerically singular location. Except for this singular location, three methods give almost the same local force. However, the equivalent current method gives a totally different local force than that of other methods as shown in Figure 3.6.3(b). This result confirms that the conventional force calculation methods provide different force distribution although they give the unique global force.

Figure 3.6.4 shows the body force distribution using the virtual air-gap scheme. Despite the exact same global force obtained from the body force calculation method and the corresponding conventional method, the force distribution shown in Figure 3.6.4 is completely different from that of Figure 3.6.3. As expected, it is shown that an almost unique body force distribution is obtained regardless of force calculation methods. Although the distribution at the corner is slightly different in each method, it is not a major portion and the overall distribution is almost the same in every method.

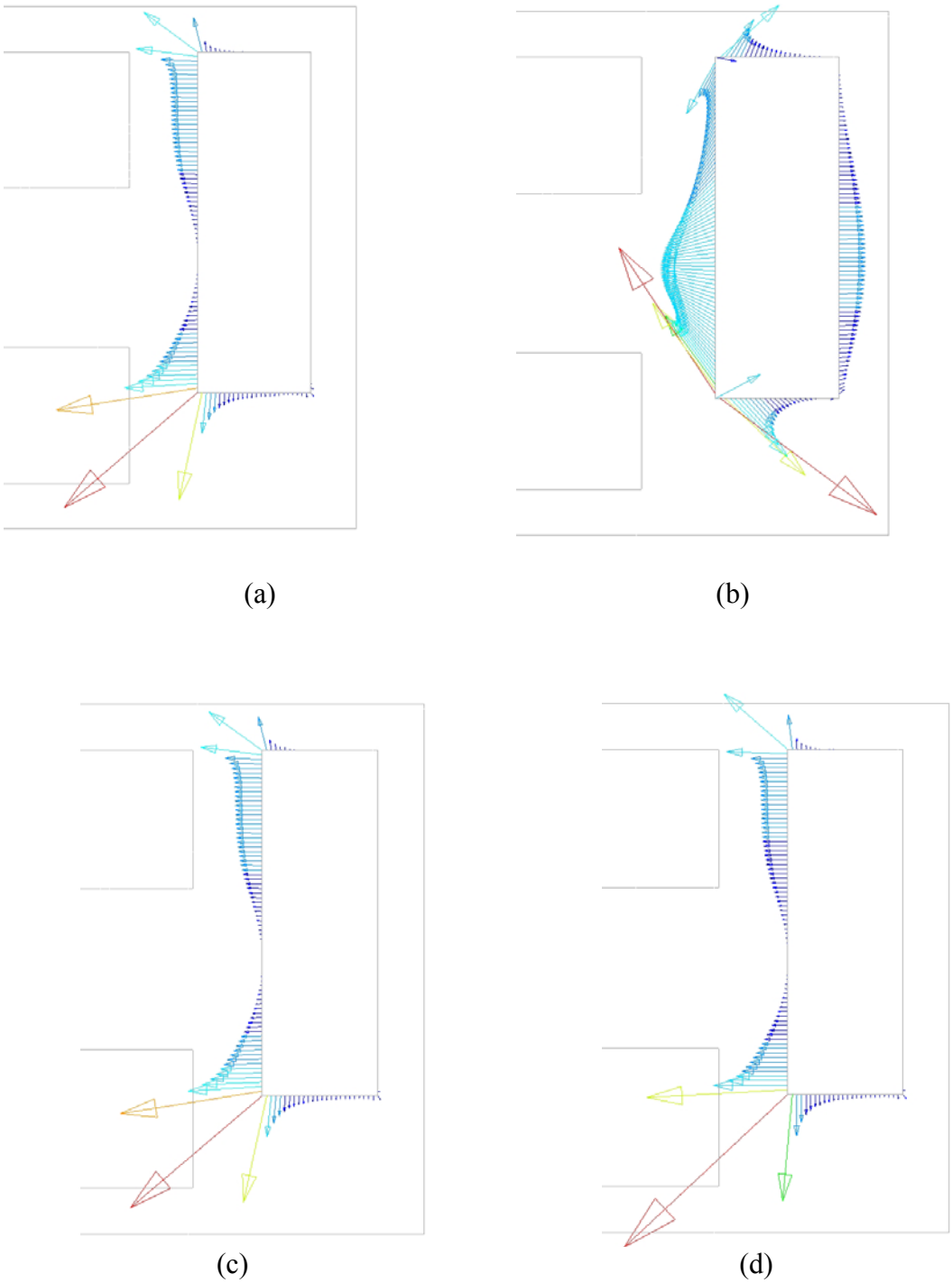

Figure 3.6.3. Local force distribution of linear problem – Conventional method: (a) Equivalent charge with averaging, (b) Equivalent current with Wignall, (c) Maxwell stress tensor with averaging, (d) local virtual work method

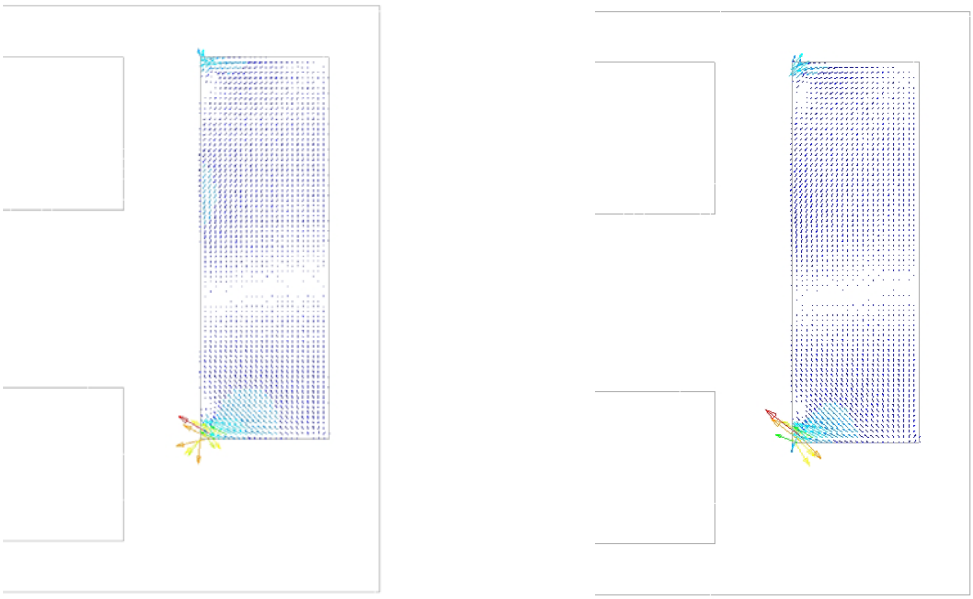

(a) (b)

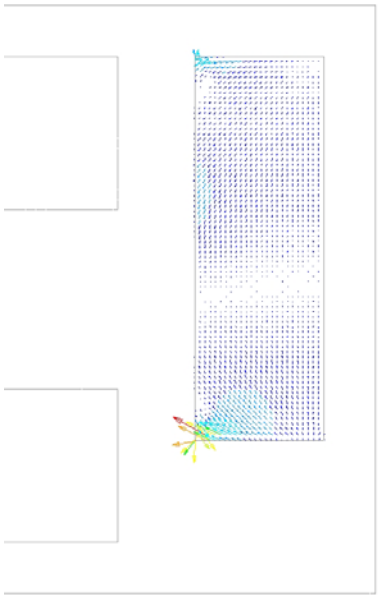

(c)

Figure 3.6.4. Local force distribution of linear problem – body force calculating using virtual air-gap scheme

(a) Equivalent charge with averaging, (b) Equivalent current with Wignall, (c) Maxwell stress tensor with averaging,

The force distribution in non-linear problems is shown in Figure 3.6.5 and Figure 3.6.6. The characteristics of each method in the non-linear case are almost the same as that of the linear case. Figure 3.6.5(a) is almost identical with that of the Maxwell stress tensor method shown in Figure 3.6.5(c). The distribution of the local virtual work method shown in Figure 3.6.5(d) is different from that of Figure 3.6.5(a) and (c) at the singular corner. The distribution using the equivalent current method shown in Figure 3.6.5 (b) has a huge error at the left bottom corner because that is a numerically singular location. This error might be the reason for the unreasonable global force of this method. The equivalent current method gives a totally different local force from that of other methods. This result confirms that the conventional force calculation methods provide different force distribution in non-linear problems.

Figure 3.6.6 shows the body force distribution in non-linear problem. The result of the equivalent current method shown in Figure 3.6.6(b) gives a huge error at the corner again. It is shown that every method including the equivalent current method gives similar body force distribution except at the corner. We might conclude that the body force distribution is unique regardless of calculation methods in both linear and non-linear problems if the method calculates the unique global force.

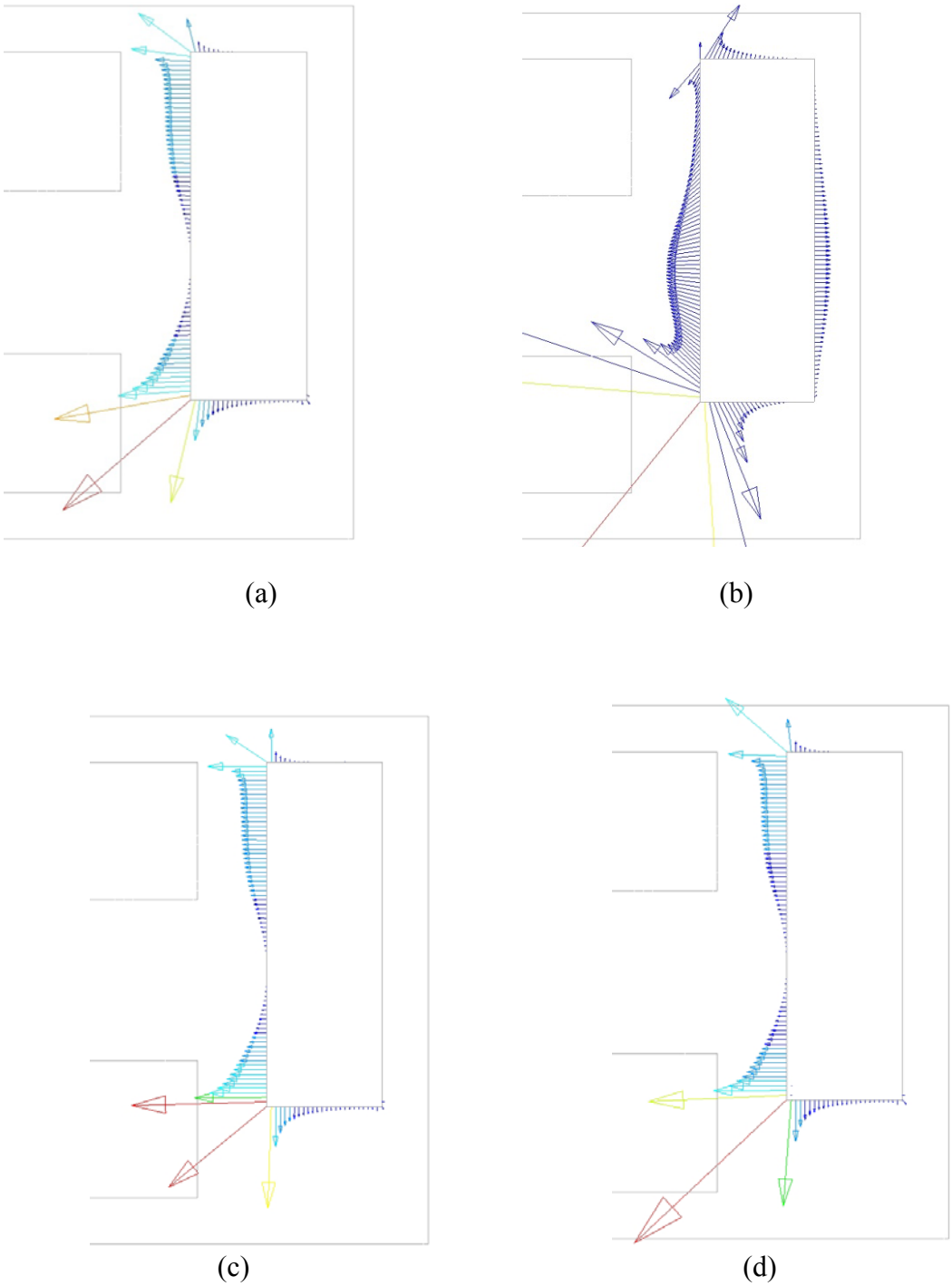

Figure 3.6.5. Local force distribution of non-linear problem – Conventional method
(a) Equivalent charge with averaging, (b) Equivalent current with Wignall,
(c) Maxwell stress tensor with averaging, (d) local virtual work method

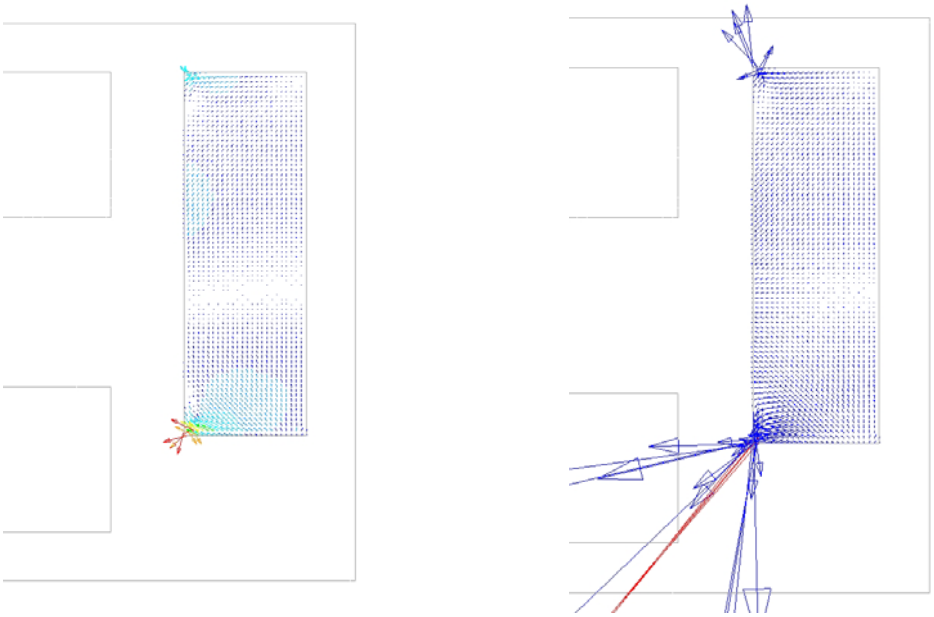

(a) (b)

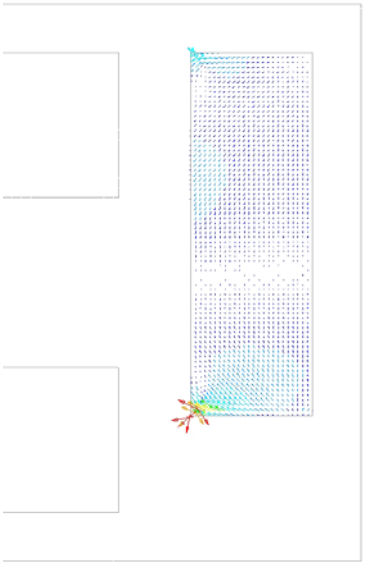

(c)

Figure 3.6.6. Local force distribution of non-linear problem – body force calculating method using virtual air-gap scheme

(a) Equivalent charge with averaging, (b) Equivalent current with Wignall, (c) Maxwell stress tensor with averaging,

3.7. Conclusions

We describe the various magnetic force calculation methods: (1) the Maxwell stress tensor method, (2) the virtual work method, (3) the Equivalent source method, (4) the body force calculation method. The virtual work method is classified into (a) global (classical) virtual work method and (b) local (Coulomb) virtual work method. The equivalent source method is classified into (a) equivalent current method (b) equivalent charge method. The derivation of each method is briefly described for both linear and non-linear problems, and the characteristics of each method are explained. As a numerical example, the magnetic force acting on the armature of the magnetic actuator is calculated using the explained methods. The Maxwell stress tensor method, virtual work method, and equivalent source method give the surface force distribution. In contrast, the body force distribution method provides the force distribution on a whole body. Although the local force distribution of the body force calculation method and conventional method is completely different, the global force of the body force calculation method is identical with that using the corresponding conventional method. The unique global force is obtained from all conventional calculation methods except the equivalent current method. However, each conventional method gives different local force distribution while the body force calculation method provides unique local force distribution.

CHAPTER 4
TOPOLOGY OPTIMIZATION TO MAXIMIZE MAGNETIC FORCE

4.1. Overview

This chapter presents a topology optimization approach to design electrical machinery. The optimization is performed based on the magnetostatic analysis and magnetic force calculation, which are demonstrated in chapter 2 and 3. Considering the different types of magnetic force, two optimization examples are presented. The first optimization example is mainly focused on the global (total) magnetic force. In contrast, the second example deals with both global (total) force and local (distributed) force in order to minimize the mechanical deformation by the local force distribution.

4.2. Optimization example I: Magnetic actuator design to maximize total magnetic force and effect of non-linear permeability

In the first example, we present the structural topology optimization of a magnetic actuator in both linear and non-linear magnetostatic systems. By comparing optimization results, the effect of nonlinearity on the actuator design is investigated. The design goal is

to maximize the total magnetic force acting on the armature. The magnetic force is calculated using the two most popular methods: the Maxwell stress tensor (MST) and local virtual work (LVW) method. Design sensitivity analysis for both linear and non-linear problems is performed using the adjoint method, and the formulated optimization problem is solved using the method of moving asymptotes (MMA). The optimization results with three different permeability models are presented, and the effect of non-linear permeability is discussed. In addition, the effect of the volume and the force calculation methods is discussed as well.

4.2.1. Introduction

The magnetic characteristics of electromagnetic devices are highly influenced by the system geometry. Therefore, the device geometry has been designed using structural optimization methods. One of the methods, structural topology optimization, has been successfully performed to improve the performance of various magnetic devices [12, 14, 127]. A perpendicular magnetic recording head has been designed for the high magnetic field of the recording region [14]. An electromagnetic shield has been optimized to reduce the average flux density in a target region [127]. The design optimization of a magnetic actuator has been performed for maximizing the force using the level-set based optimization method [12]. These studies are limited to a linear problem, where the permeability of magnetic material is constant. A few works address the structural optimization of the non-linear problem [16, 23]. However, none of these works presented the effect of nonlinearity on the design result.

We present the structural topology optimization of a magnetic actuator in both linear and non-linear problems. By comparing optimization results, the effect of the non-linear **B-H** relation is investigated. In addition, the effect of the design domain volume is also examined. The optimization goal is to maximize the magnetic force acting on the armature. The magnetic force is calculated using two major methods: the Maxwell stress tensor (MST) and local virtual work (LVW) method. It should be noted that the LVW method has not yet been used for the structural optimization problem with a non-linear **B-H** relation. The optimization results of two force calculation methods are compared, and the influence of the force calculation methods is investigated.

4.2.2.Formulation of the optimization problem

A two dimensional model of the magnetic actuator is designed using the structural topology optimization method. This method aims to find the density distribution of the design domain to achieve a design goal. In order to perform the sensitivity analysis for the mathematical programming methods, the density is relaxed as a continuous function. When the density is zero, the material becomes the air, and when the density is one, it becomes the steel. The material properties of intermediate densities are interpolated using the density method proposed in [10]. Then, the permeability μ can be written as

$$\frac{1}{\mu(B^2)} = \left(s_1 \cdot e^{s_2 B^2} + s_3\right)\rho^p + \frac{1}{\mu_{air}}\left(1-\rho^p\right) \tag{4.2.1}$$

The design goal is to maximize the magnetic force F_i acting on the armature. The magnetic force is predicted using both the MST and LVW methods. The model of the magnetic actuator and the integration path used for the MST method is shown in Figure 4.2.1. The armature in the model is set as the design domain of the structural topology optimization problem. In order to find the density distribution maximizing the magnetic force with the volume constraint, the optimization problem is defined as

$$\begin{aligned} &\text{Find} && \rho_{\mathrm{k}} \\ &\text{Maximize} && F_i\left(\mathbf{A}(\boldsymbol{\rho}),\boldsymbol{\rho}\right) \\ &\text{subject to} && 0<\rho_{\min} \le \rho_k \le \rho_{\max} \qquad \left(k=1,..,ND\right) \\ & && \frac{V(\boldsymbol{\rho})}{V^*}=1 \end{aligned} \tag{4.2.2}$$

where **A** is the vector potential obtained as the finite element solution, ρ_k is the density of element k, ND is the number of design variables, $V(\boldsymbol{\rho})$ is the volume of the design domain, and V^* is the specified volume fraction. The objective function (*i.e.* the magnetic force F_i) is a function of magnetic vector potential **A** and density $\boldsymbol{\rho}$. The above optimization problem is solved using the method of moving asymptotes (MMA).

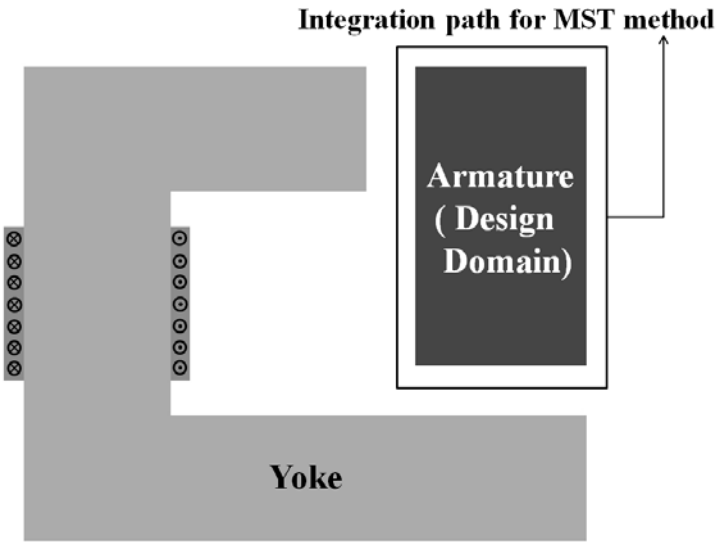

Figure 4.2.1. Magnetic actuator model

4.2.3. Sensitivity analysis and verification

The sensitivity of the objective function with respect to the design variable (*i.e.* density ρ) is analytically derived using the adjoint variable method.

Linear problem

In the linear problem, the finite element equation is written as

$$\mathbf{K}(\boldsymbol{\rho})\mathbf{A} = \mathbf{Q} \tag{4.2.3}$$

where **K** and **Q** represent the magnetic stiffness matrix and the load vector. From the adjoint variable method, the sensitivity of the force F_i is derived as

$$\begin{aligned}\frac{dF_i}{d\boldsymbol{\rho}} &= \frac{\partial F_i}{\partial \boldsymbol{\rho}} + \frac{\partial F_i}{\partial \mathbf{A}}\frac{\partial \mathbf{A}}{\partial \boldsymbol{\rho}} + \boldsymbol{\lambda}^T \frac{\partial}{\partial \boldsymbol{\rho}}\left(\mathbf{K}\mathbf{A} - \mathbf{Q}\right) \\ &= \frac{\partial F_i}{\partial \boldsymbol{\rho}} + \boldsymbol{\lambda}^T \frac{\partial \mathbf{K}}{\partial \boldsymbol{\rho}}\mathbf{A} + \cancel{\left(\boldsymbol{\lambda}^T \mathbf{K} + \frac{\partial F_i}{\partial \mathbf{A}}\right)\frac{\partial \mathbf{A}}{\partial \boldsymbol{\rho}}} \\ &\qquad\qquad \left(\because \text{adjoint equation}\right) \\ &= \frac{\partial F_i}{\partial \boldsymbol{\rho}} + \boldsymbol{\lambda}^T \frac{\partial \mathbf{K}(\boldsymbol{\rho})}{\partial \boldsymbol{\rho}}\mathbf{A}\end{aligned} \tag{4.2.4}$$

Because **K** is symmetric, the adjoint equation becomes:

$$\mathbf{K}^T\boldsymbol{\lambda} = -\frac{\partial F_i}{\partial \mathbf{A}} \tag{4.2.5}$$

The calculation of Eq. (4.2.4) and (4.2.5) requires $\frac{\partial F_i}{\partial \boldsymbol{\rho}}$ and $\frac{\partial F_i}{\partial \mathbf{A}}$, which can be derived from the force formulation F_i in each method.

When the MST method is used, the above two terms are obtained as follows. The first term $\frac{\partial F_i}{\partial \boldsymbol{\rho}}$ is zero if the integration line is not on the surface of an object. The density $\boldsymbol{\rho}$ does not influence the total force F_i explicitly. Next, the derivative of total force $\frac{\partial F_i}{\partial \mathbf{A}}$ can be derived from Eq. (3.2.10) as

$$\frac{\partial F_i}{\partial \mathbf{A}} = \left[\iint_A \frac{1}{2\mu_0}(2B_n \frac{\partial B_n}{\partial \mathbf{A}} - 2B_t \frac{\partial B_t}{\partial \mathbf{A}})dA\right]\mathbf{t} + \left[\iint_A \frac{1}{\mu_0}\left(\frac{\partial B_n}{\partial \mathbf{A}}B_t + B_n \frac{\partial B_t}{\partial \mathbf{A}}\right)dA\right]\mathbf{n} \tag{4.2.6}$$

From Eq.(3.2.8) and (3.2.9) , the derivatives of normal and tangential magnetic flux density B_n and B_t are written as

$$\frac{\partial B_n}{\partial \mathbf{A}} = -\sin(\theta)\frac{\partial B_x}{\partial \mathbf{A}} + \cos(\theta)\frac{\partial B_y}{\partial \mathbf{A}} \tag{4.2.7}$$

$$\frac{\partial B_t}{\partial \mathbf{A}} = \cos(\theta)\frac{\partial B_x}{\partial \mathbf{A}} + \sin(\theta)\frac{\partial B_y}{\partial \mathbf{A}} \tag{4.2.8}$$

where θ is the angle between the surface line and x direction. From the relation between the magnetic flux density B and the vector potential A in the 2D finite element formulation, the derivative of B_x and B_y can be written as

$$\begin{pmatrix} \dfrac{\partial B_x}{\partial A_j} \\ \dfrac{\partial b_y}{\partial A_j} \end{pmatrix} = \begin{pmatrix} \dfrac{\partial N_1}{\partial y} & \dfrac{\partial N_2}{\partial y} & \dfrac{\partial N_3}{\partial y} & \dfrac{\partial N_4}{\partial y} \\ -\dfrac{\partial N_1}{\partial x} & -\dfrac{\partial N_2}{\partial x} & -\dfrac{\partial N_3}{\partial x} & -\dfrac{\partial N_4}{\partial x} \end{pmatrix} \begin{pmatrix} \delta_{1j} \\ \delta_{2j} \\ \delta_{3j} \\ \delta_{4j} \end{pmatrix} \tag{4.2.9}$$

where N_1-N_4 is the shape functions of the finite element method, and δ_{ij} is the Kronecker delta function.

When the LVW method is applied, the two terms $\frac{\partial F_i}{\partial \boldsymbol{\rho}}$ and $\frac{\partial F_i}{\partial \mathbf{A}}$ are derived from the force formulation Eq. (3.3.5) Because **S** of Eq. (3.3.5) is not a function of either $\boldsymbol{\rho}$ and **A**, the first term $\frac{\partial F_i}{\partial \boldsymbol{\rho}}$ is simply written as

$$\frac{\partial F_i}{\partial \boldsymbol{\rho}} = \frac{\partial (1/2\mu)}{\partial \boldsymbol{\rho}} \mathbf{A}^{\mathbf{T}} \frac{\partial \mathbf{S}}{\partial \alpha} \mathbf{A} \tag{4.2.10}$$

The second term $\frac{\partial F_i}{\partial \mathbf{A}}$ is derived as

$$\frac{\partial F_i}{\partial \mathbf{A}} = \frac{1}{2\mu} \left(\frac{\partial \mathbf{A}}{\partial \mathbf{A}} \right)^T \frac{\partial \mathbf{S}}{\partial \alpha} \mathbf{A} + \frac{1}{2\mu} \mathbf{A}^T \frac{\partial \mathbf{S}}{\partial \alpha} \frac{\partial \mathbf{A}}{\partial \mathbf{A}} \tag{4.2.11}$$

Finally the sensitivity of magnetic force in the linear problem is calculated from Eq. (4.2.4)-(4.2.11).

Non-linear problem

In the non-linear problem, the finite element equation is represented as

$$\mathbf{K}\left(\mathbf{A}(\boldsymbol{\rho}), \boldsymbol{\rho}\right) \mathbf{A} = \mathbf{Q} \tag{4.2.12}$$

Here, the stiffness matrix **K** is the function of the magnetic vector potential **A**. To solve Eq. (4.2.12) using the Newton-Raphson method, we need to solve the equation:

$$\left(K_{ij} + \frac{\partial K_{ik}}{\partial A_j} A_k \right) v_i^{(n)} = Q_j - K_{ij} A_j \tag{4.2.13}$$

From the adjoint variable method, the sensitivity of the total magnetic force is derived as

$$\begin{aligned}\frac{dF_q}{d\rho_p} &= \frac{\partial F_q}{\partial \rho_p} + \frac{\partial F_q}{\partial A_j}\frac{\partial A_j}{\partial \rho_p} + \lambda_i \frac{\partial\left(K_{ij}A_j - f_i\right)}{\partial \rho_p} \\ &= \frac{\partial F_q}{\partial \rho_p} + \lambda_i \frac{\partial K_{ij}}{\partial \rho_p}A_j + \cancel{\left(\lambda_i\left(K_{ij} + \frac{\partial K_{ik}}{\partial A_j}A_k\right) + \frac{\partial F_q}{\partial A_j}\right)\frac{\partial A_j}{\partial \rho_p}} \\ &\qquad\qquad (\because \text{ adjoint equation}) \\ &= \frac{\partial F_q}{\partial \rho_p} + \lambda_i \frac{\partial K_{ij}}{\partial \rho_p}A_j\end{aligned} \tag{4.2.14}$$

The adjoint equation is given as

$$\left(K_{ij} + \frac{\partial K_{ik}}{\partial A_j}A_k\right)\lambda_i = -\frac{\partial F_q}{\partial A_j} \tag{4.2.15}$$

The stiffness matrix of Eq. (4.2.15) is identical with the Jacobian matrix of the Newton-Raphson method, which is shown in (4.2.13). It is noted that **K** and **A** should be the final converged quantities. Therefore, the sensitivity analysis of the non-linear problem is carried out after the Newton-Raphson iteration is finished. The calculation of Eq. (4.2.14) and (4.2.15) requires $\frac{\partial F_q}{\partial \rho_p}$ and $\frac{\partial F_q}{\partial A_j}$, which can be derived from the force formulation of each method.

When the MST method is applied, the force formulation is not different from that of the linear problem, and consequently, two terms are also identical with that of linear problem. Thus, $\frac{\partial F_q}{\partial \rho_p}$ is zero and $\frac{\partial F_q}{\partial A_j}$ is derived from Eq. (4.2.6)-(4.2.9).

When the LVW method is used, the force formulation Eq. (3.3.9) is different from that of linear problem Eq. (3.3.5). The first term $\frac{\partial F_q}{\partial \rho_p}$ is derived as

$$\frac{\partial F_q}{\partial \rho_p} = -\int \left\{ \frac{\partial \left(1/\mu\left(B^2\right)\right)}{\partial \rho_p} A_{zi} A_{zj} \begin{pmatrix} \frac{\partial N_i}{\partial r} & \frac{\partial N_i}{\partial s} \end{pmatrix} \mathbf{J}^{-T} \mathbf{J}^{-1} \frac{\partial \mathbf{J}}{\partial \alpha} \mathbf{J}^{-1} \begin{pmatrix} \frac{\partial N_i}{\partial r} & \frac{\partial N_i}{\partial s} \end{pmatrix}^T \right\} \cdot |\mathbf{J}| \, dV_{rs} + \int \left(\int_0^B \frac{\partial \left(1/\mu(B^2)\right)}{\partial \rho_p} b \, db \right) \cdot \frac{\partial |\mathbf{J}|}{\partial \alpha} dV_{rs} \tag{4.2.16}$$

where

$$\frac{\partial \left(1/\mu(B^2)\right)}{\partial \rho} = p\left(s_1 \cdot e^{s_2 B^2} + s_3\right) \rho^{p-1} - p \frac{1}{\mu_{air}} \rho^{p-1} \tag{4.2.17}$$

$$\int_0^B \frac{\partial \left(1/\mu(B^2)\right)}{\partial \rho} b \, db = \frac{s_2 s_3 B^2 + s_1 \left(e^{s_2 B^2} - 1\right)}{2 s_2} p \rho^{p-1} - \frac{1}{2} B^2 p \frac{1}{\mu_{air}} \rho^{p-1} \tag{4.2.18}$$

The second term $\frac{\partial F_q}{\partial A_j}$ is derived as

$$\frac{\partial F_q}{\partial A_j} = -\int \left\{ \frac{1}{\mu(B^2)} \frac{\partial A_{zm}}{\partial A_j} \frac{\partial \tilde{S}_{mn}}{\partial \alpha} A_{zn} \right\} \cdot |\mathbf{J}| \, dV_{rs} - \int \left\{ \frac{1}{\mu(B^2)} A_{zm} \frac{\partial \tilde{S}_{mn}}{\partial \alpha} \frac{\partial A_{zn}}{\partial A_j} \right\} \cdot |\mathbf{J}| \, dV_{rs}$$
$$- \int \left\{ \frac{\partial \left(1/\mu(B^2) \right)}{\partial A_j} A_{zm} \frac{\partial \tilde{S}_{mn}}{\partial \alpha} A_{zn} \right\} \cdot |\mathbf{J}| \, dV_{rs} + \int \frac{\partial \left(\int_0^B \frac{1}{\mu(B^2)} b \, db \right)}{\partial A_j} \cdot \frac{\partial |\mathbf{J}|}{\partial \alpha} dV_{rs} \tag{4.2.19}$$

where

$$\frac{\partial \tilde{S}_{mn}}{\partial \alpha} = \begin{pmatrix} \frac{\partial \mathbf{N}}{\partial r} \\ \frac{\partial \mathbf{N}}{\partial s} \end{pmatrix}^T \mathbf{J}^{-T} \mathbf{J}^{-1} \frac{\partial \mathbf{J}}{\partial \alpha} \mathbf{J}^{-1} \begin{pmatrix} \frac{\partial \mathbf{N}}{\partial r} \\ \frac{\partial \mathbf{N}}{\partial s} \end{pmatrix} \tag{4.2.20}$$

$$\frac{\partial \left(1/\mu\left(B^2\right) \right)}{\partial A_j} = \frac{\partial \left(1/\mu\left(B^2\right) \right)}{\partial B^2} \frac{\partial B^2}{\partial A_j} = 2\left(s_1 s_2 \cdot e^{s_2 B^2} \right) \rho^p \left(\frac{\partial N_j}{\partial x} \frac{\partial N_n}{\partial x} + \frac{\partial N_j}{\partial y} \frac{\partial N_n}{\partial y} \right) a_n \tag{4.2.21}$$

The sensitivity of magnetic force in the non-linear problem can be obtained from Eq. (4.2.14)-(4.2.21).

The derived analytical sensitivity is compared to the finite difference sensitivity for verification. The sensitivity of the linear problem is compared in Figure 4.2.2.(a), and that of the non-linear problem is compared in Figure 4.2.2.(b). The sensitivity from both the MST and LVW methods are shown here. As shown in Figure 4.2.2., the analytical sensitivity is in good agreement with the finite difference sensitivity.

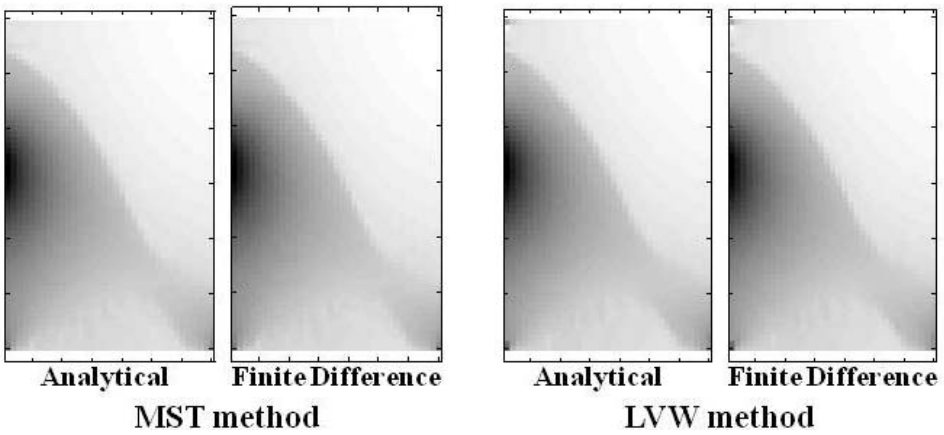

(a)

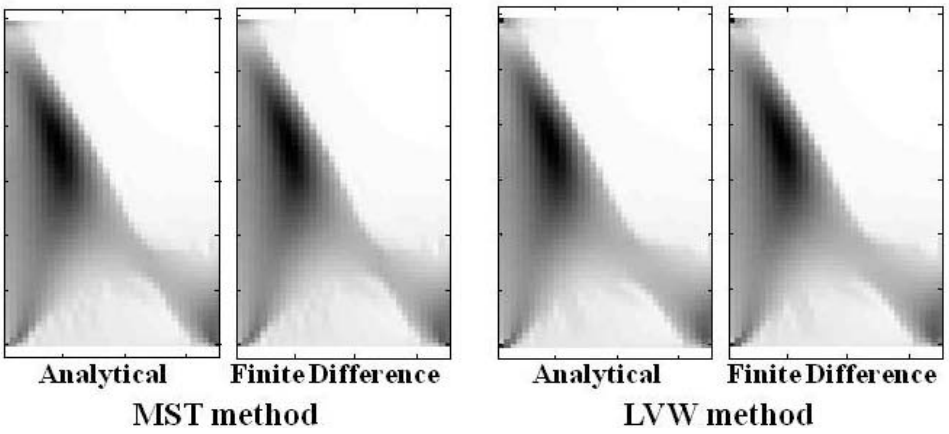

(b)

Figure 4.2.2.Comparison of the analytical and finite difference sensitivity
(a) Linear problem, (b) Non-linear problem

4.2.4. Design result and physical explanation

In order to investigate the effect of the non-linear **B-H** relation on the actuator design, three different cases of the permeability are applied to the yoke and armature. The permeability model proposed in [103], is written as

$$\frac{1}{\mu\left(B^2\right)} = k_1 e^{k_2 B^2} + k_3 \tag{4.2.22}$$

In the first case, the permeability is constant (k_1=k_2=0, k_3=520.6), and the **B-H** relation is linear. In the second case, the **B-H** relation is non-linear (k_1=30, k_2=0.8, k_3=520.6). In the third case, it is highly non-linear (k_1=49.4, k_2=1.46, k_3=520.6). The **B-H** relations of three cases are shown in Figure 4.2.3

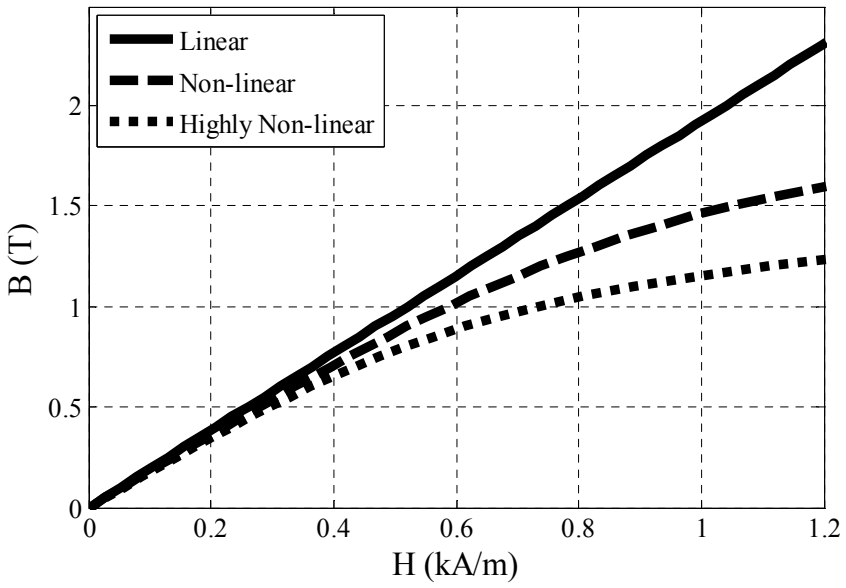

Figure 4.2.3. **B-H** relation of three cases

The armature of the magnetic actuator is designed for maximizing x or y directional force acting on it with different volume constraints. The design result is shown in Figure 4.2.4(a) and (b). The results from the MST and LVW methods are almost identical, and therefore only the results from the LVW methods are presented in Figure 4.2.4. It is well known that the different force calculation methods give identical total magnetic force results. Here, it is shown that the optimization result for the total magnetic force is also not dependent on the force calculation methods.

The effect of the non-linear **B-H** relation can be seen in Figure 4.2.4. The design results show that the nonlinearity makes the structure simple and concentrated. The result of the linear problem contains several thin structures, whereas that of the non-linear problem is composed of one or two thick structures. This might be because the magnetic field is easily saturated in a thin structure. In the linear problem, the magnetic saturation is ignored, and therefore thin structures can maximize the magnetic field. In the non-linear problem, however, the magnetic saturation of a thin structure decreases the magnetic field, and therefore the result tends to have a thick concentrated structure. Although the magnetic field is not linearly related to the magnetic force, it can be thought that the low magnetic field may decrease the magnetic force.

	V^*=0.2	V^*=0.4	V^*=0.6
Linear	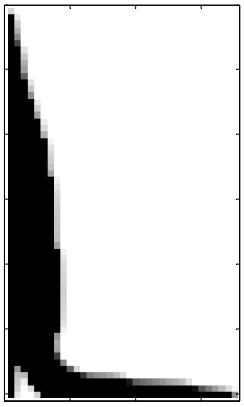	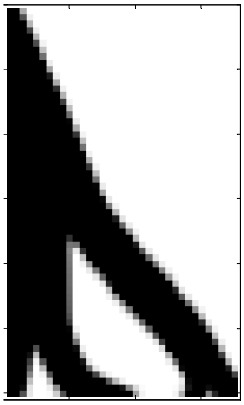	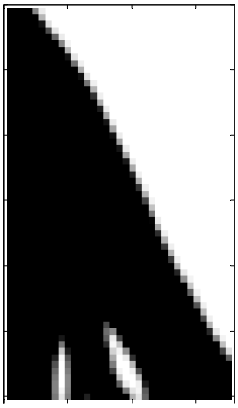
Non-linear	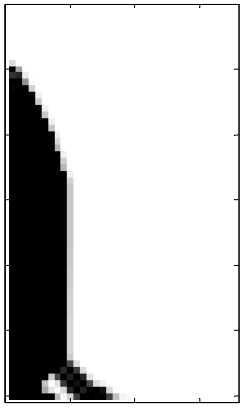	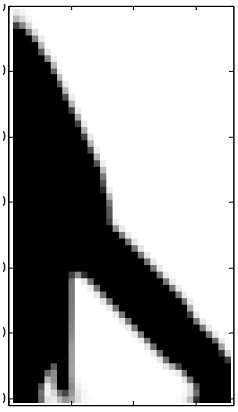	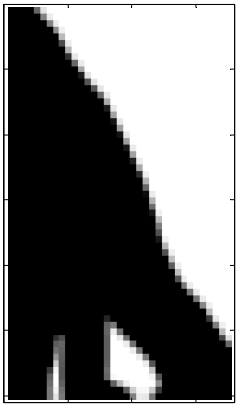
Highly Non-linear		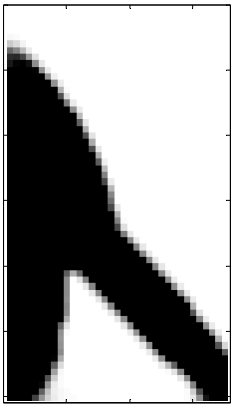	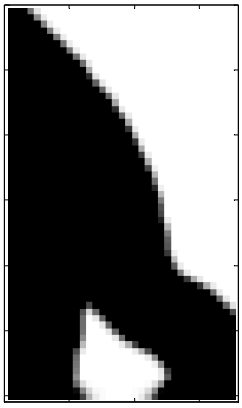

(a)

	V^*=0.2	V^*=0.4	V^*=0.6
Linear	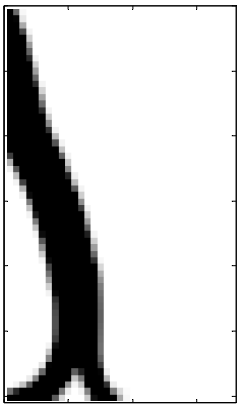	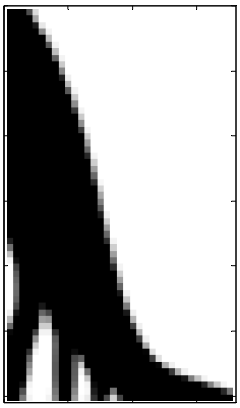	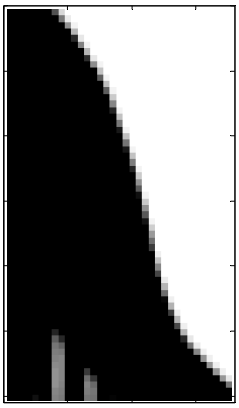
Non-linear	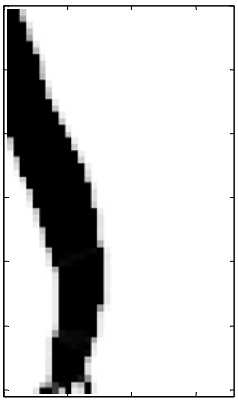	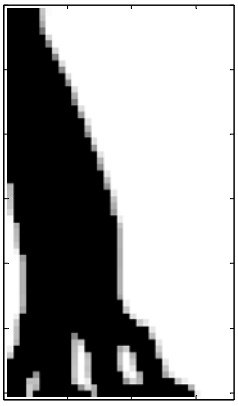	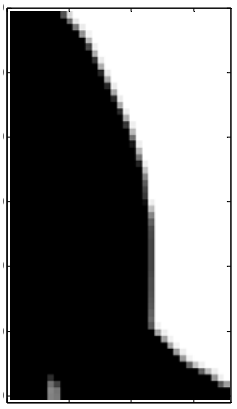
Highly Non-linear			

(b)

Figure 4.2.4. Armature design result

(a) F_x maximization, (b) F_y maximization

The effect of the volume constraint can be investigated in Figure 4.2.5(a) and (b). They show the calculated force of the optimized results with respect to the volume constraint. In the linear problem, the force is slightly decreased in a small volume. The force is decreased by only 10% when the volume is decreased from 100% to 20%. In the non-linear problem, however, the force is considerably decreased in a small volume. This may be because the magnetic saturation becomes severe in a small volume. In a linear problem, the magnetic field can increase freely even in a small volume. However, the magnetic saturation of a non-linear problem interrupts the increase of the magnetic field in a small volume, and consequently the force is severely decreased.

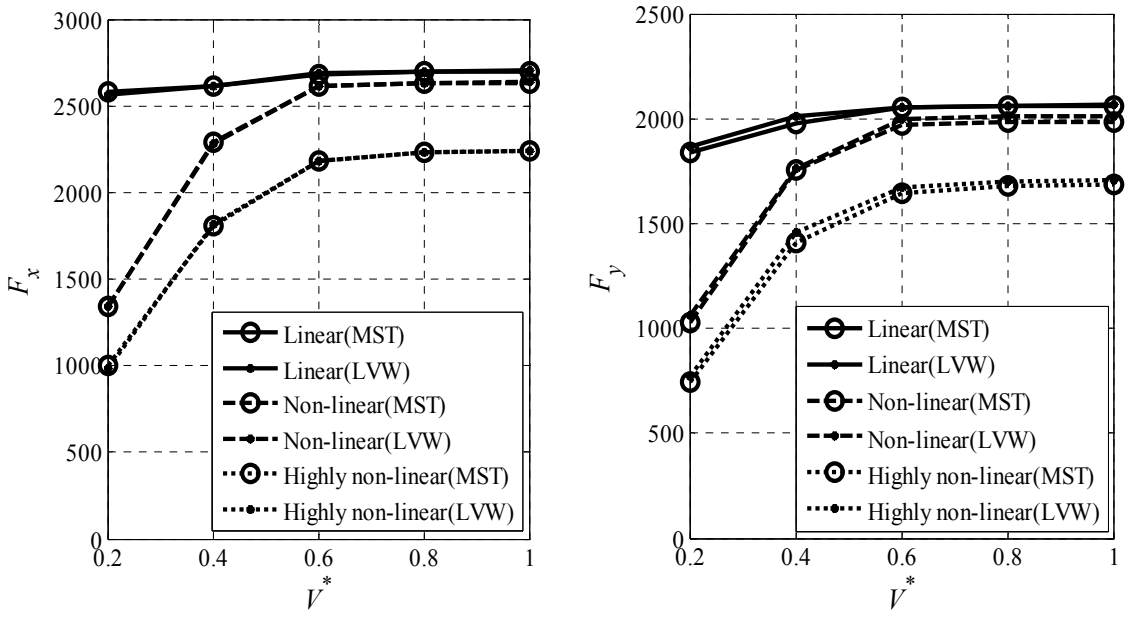

(a) (b)

Figure 4.2.5. Magnetic force with respect to volume constraint
(a) F_x maximization, (b) F_y maximization

4.2.5. Conclusion

The structural topology optimization of a magnetic actuator is carried out to maximize the magnetic force. The magnetic force is calculated from the MST and LVW methods, and the design sensitivity is analytically derived and verified. The armature of the actuator is optimized with three different permeability models. From the optimization results, the nonlinear effect on the actuator design is discussed, and the effect of volume constraint and force calculation methods is also presented.

4.3. Optimization example II: Structural optimization to maximize stiffness with body force distribution

In the second example, we present structural topology optimization applied to the coupled magneto-structural problem. The design goals are to minimize mechanical compliance and to maximize total magnetic force. To calculate the compliance and magnetic force, coupled magneto-structural analysis is performed using the finite element method. From the solution of magnetostatic analysis, distribution of the magnetic body force is obtained using the virtual air gap scheme. The structural analysis from the calculated force distribution then provides the mechanical compliance. The design sensitivity analysis for the optimization is performed using the adjoint method, and the derived sensitivity is verified by comparing it with the finite difference sensitivity. The optimization problem is formulated and solved using the sequential linear programming (SLP) method. To show the validity of the proposed analysis and optimization approach, design of the solenoid actuator is presented.

4.3.1. Introduction

Electrical machinery such as electric motors and solenoid actuators are aimed at producing a strong movement of an object with minimum vibration. Therefore, high magnetic force and low vibration level have been two main goals in designing electrical machinery. These design goals have been successfully achieved using the structural topology optimization approach [8, 12, 77, 128]. Magnetic force of the actuator was maximized using the level-set based optimization method [12]. The optimal shape of the

electromagnetic coupler was designed to maximize the actuating force in a prescribed direction [128]. Vibration reduction also has been accomplished. The frequency response excited by the magnetic harmonic force was minimized using the homogenization design method [8]. A switched reluctance motor was designed to minimize the vibration level [77]. None of these studies, however, shows design optimization of electrical machinery than can satisfy both magnetic and mechanical design goals.

This paper presents a structural topology optimization approach to maximize the total magnetic force and minimize the mechanical deformation caused by the distributed magnetic force. The magnetic force is calculated as the distributed body force using the virtual air-gap scheme [120, 121]. A similar approach using the Coulomb virtual work (CVW) method was already presented in [17]. The CVW method gives the force distribution on the surface of magnetic materials. Figure 4.3.1 (a) and (b) compare the surface force distribution using the CVW method and the body force distribution using the virtual air-gap scheme. It is well known that the total force is identical regardless of the force calculation methods, but the force distribution is totally different, as shown in Figure 4.3.1. A debate about the true force distribution is still in progress. However, the application of the CVW method for structural topology optimization has considerable problems even if it describes true force distribution.

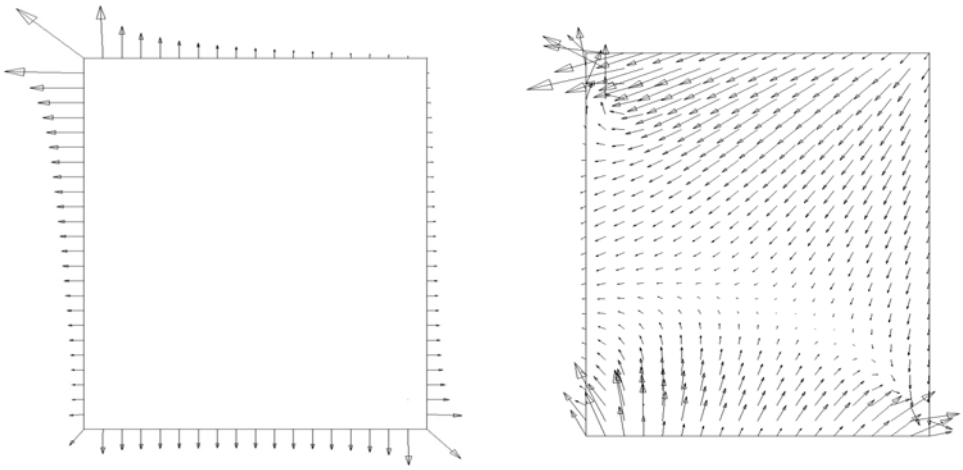

(a) (b)

Figure 4.3.1. Magnetic force distribution

(a) Surface force from CVW method, (b) Body force from virtual air-gap scheme

The CVW method identifies the large numerical errors in the force distribution calculation when different materials are in contact [121]. This method can be used only when an object surrounded by air is composed of a single material. In the structural topology optimization procedure, each finite element may have different material properties. This structure can be thought of as a composition containing different materials in contact with others. Therefore, the force distribution during the structural topology optimization cannot be accurately calculated using the CVW method. Even if the CVW method gives a true force distribution, it may not be proper for the structural topology optimization. In contrast, the virtual air-gap scheme gives accurate force distribution of different materials in contact. Thus, the body force distribution using the virtual air-gap scheme may be more appropriate for the structural topology optimization problem.

Structural optimization considering the body force distribution of electric machines has not been carried out yet. The optimization result is expected to be totally different from that using the CVW method. As already shown in Figure 4.3.1, the force distribution with the two methods is completely different. Thus the structural analysis result may be different as well, and consequently, a different optimization result may be obtained. In spite of the inconclusive debate about the true force distribution, optimization using the body force distribution deserves to be investigated.

4.3.2. Magneto-structural analysis

Coupled magneto-structural analysis is performed using the finite element method. First, the magnetostatic analysis is carried out using the vector potential **A** method. From the analysis solution, we can calculate the body force **b** distribution using the virtual air-gap scheme. Next, the body force distribution yields the structural nodal force vector $\mathbf{f}_S$. Finally the structural analysis gives the mechanical displacement **u**.

The finite element equation for the magnetostatic analysis can be written as

$$\mathbf{K}_M \mathbf{A} = \mathbf{Q} \tag{4.3.1}$$

where $\mathbf{K}_M$ is the magnetic stiffness matrix, **A** is the vector potential, and **Q** is the magnetic load vector. After solving (4.3.1), the magnetic flux density **B** is calculated as

$$\mathbf{B} = \nabla \times \mathbf{A} \tag{4.3.2}$$

From the magnetic field **B**, the distribution of the body force **b** can be calculated using the virtual air-gap scheme, which is presented in section 3.5. For the accurate force calculation, the magnetic field is corrected using the averaging method, which is explained in section 3.6.1.

The distributed body force **b** gives the structural nodal force vector $\mathbf{f}_S$. In the finite element formulation, the nodal force at the *j*th node $\mathbf{f}_S^j$ is represented as

$$\mathbf{f}_S{}^j = \int N_j \mathbf{b}\, d\Omega \tag{4.3.3}$$

where N_j is the shape function of the *j*th node. Then, the finite element equation for the structural analysis can be written as

$$\mathbf{K}_S \mathbf{u} = \mathbf{f}_S \tag{4.3.4}$$

where $\mathbf{K}_S$ is the structural stiffness matrix, and **u** is the mechanical displacement vector. The structural force vector $\mathbf{f}_s$ is the function of the magnetic vector potential **A**. Therefore, the structural analysis is coupled with the magnetostatic analysis.

By solving Eq. (4.3.4), **u** is obtained, and the mechanical compliance *l* is calculated as

$$l = \mathbf{f}_S{}^T \mathbf{u} \tag{4.3.5}$$

When the compliance is minimized, the displacement **u** is reduced, and consequently, the stiffness of the structure is globally maximized.

4.3.3. Optimization problem formulation

Electrical machinery design can be performed using the structural topology optimization method. As with the conventional structural topology optimization problem, the densities of the design domain are set as the design variable, and the material property is interpolated using the density method proposed in [10].

The optimization goals are to minimize the mechanical compliance and to maximize the total magnetic force. The total force F_{tot} is the magnitude of the total force vector which can be obtained as the sum of the distributed body force. To achieve the above design goals, the optimization problem is formulated as

$$\begin{aligned} &\text{Find} \quad \rho_{\mathrm{k}} \quad (k = 1,..,ND) \\ &\text{Minimize} \quad \varphi = \alpha\left[\mathbf{f}_S\left(\mathbf{A}(\boldsymbol{\rho}),\boldsymbol{\rho}\right)^T \mathbf{u}(\boldsymbol{\rho})\right] + \beta\left[-F_{tot}\left(\mathbf{A}(\boldsymbol{\rho}),\boldsymbol{\rho}\right)\right] \\ &\text{subject to} \quad 0<\rho_{\min} \le \rho_k \le \rho_{\max} \\ &\qquad \frac{V(\boldsymbol{\rho})}{V^*} = 1 \end{aligned} \tag{4.3.6}$$

where ρ_k is the density of element k, and ND is the number of design variables. The objective function φ is defined as the scaled sum of the mechanical compliance and total

magnetic force. The scaling factors α and β are controlled using the adaptive scaling strategy proposed in [129]. The volume $V(\boldsymbol{\rho})$ of the design domain is constrained to the specified volume fraction V^*. The optimization problem Eq. (4.3.6) is solved by SLP, which requires design sensitivity analysis.

4.3.4. Design sensitivity analysis

The sensitivity of the objective function φ is analytically derived using the adjoint variable method. The derivative of the function φ with respect to the density $\boldsymbol{\rho}$ is written as

$$\frac{\partial \varphi}{\partial \boldsymbol{\rho}} = \alpha \left[\frac{\partial \left(\mathbf{f}_S \left(\mathbf{A}(\boldsymbol{\rho}), \boldsymbol{\rho} \right)^T \mathbf{u}(\boldsymbol{\rho}) \right)}{\partial \boldsymbol{\rho}} \right] + \beta \left[\frac{\partial \left(-F_{tot} \left(\mathbf{A}(\boldsymbol{\rho}), \boldsymbol{\rho} \right) \right)}{\partial \boldsymbol{\rho}} \right] \tag{4.3.7}$$

From the adjoint variable method using the finite element equations (Eq. (4.3.1) and (4.3.4)) , the first term of (4.3.7) is derived as

$$\frac{\partial \mathbf{f}_s{}^T \mathbf{u}}{\partial \boldsymbol{\rho}} = \left(\frac{\partial \mathbf{f}_s}{\partial \boldsymbol{\rho}} + \frac{\partial \mathbf{f}_s}{\partial \mathbf{A}} \frac{\partial \mathbf{A}}{\partial \boldsymbol{\rho}} \right)^T \mathbf{u} + \mathbf{f}_s{}^T \frac{\partial \mathbf{u}}{\partial \boldsymbol{\rho}} + \boldsymbol{\lambda}_1{}^T \frac{\partial}{\partial \boldsymbol{\rho}} \left(\mathbf{K}_\mathbf{M} \mathbf{A} - \mathbf{Q} \right) - \boldsymbol{\lambda}_2{}^T \left(\mathbf{K}_\mathbf{S} \mathbf{u} - \mathbf{f}_S \right)$$

$$= \frac{\partial \mathbf{f}_s{}^T}{\partial \boldsymbol{\rho}} \mathbf{u} + \boldsymbol{\lambda}_1{}^T \frac{\partial \mathbf{K}_\mathbf{M}}{\partial \boldsymbol{\rho}} \mathbf{A} - \boldsymbol{\lambda}_2{}^T \frac{\partial \mathbf{K}_\mathbf{S}}{\partial \boldsymbol{\rho}} \mathbf{u}$$

$$+ \cancel{\left(\mathbf{u}^T \frac{\partial \mathbf{f}_s}{\partial \mathbf{A}} + \boldsymbol{\lambda}_1{}^T \mathbf{K}_\mathbf{M} + \boldsymbol{\lambda}_2{}^T \frac{\partial \mathbf{f}_S}{\partial \mathbf{A}} \right) \frac{\partial \mathbf{A}}{\partial \boldsymbol{\rho}}} + \cancel{\left(\mathbf{f}_s{}^T - \boldsymbol{\lambda}_2{}^T \mathbf{K}_\mathbf{S} \right) \frac{\partial \mathbf{u}}{\partial \boldsymbol{\rho}}} \tag{4.3.8}$$

$$\text{(adjoint equation)} \qquad \text{(adjoint equation)}$$

$$= 2 \frac{\partial \mathbf{f}_s{}^T}{\partial \boldsymbol{\rho}} \mathbf{u} + \boldsymbol{\lambda}_1{}^T \frac{\partial \mathbf{K}_M}{\partial \boldsymbol{\rho}} \mathbf{A} + \boldsymbol{\lambda}_2{}^T \left(-\frac{\partial \mathbf{K}_S}{\partial \boldsymbol{\rho}} \mathbf{u} \right)$$

The adjoint variables $\boldsymbol{\lambda}_1$ and $\boldsymbol{\lambda}_2$ are obtained by solving the following adjoint equations:

$$\mathbf{K}_M \boldsymbol{\lambda}_1 = -2 \frac{\partial \mathbf{f}_S{}^T}{\partial \mathbf{A}} \mathbf{u} \tag{4.3.9}$$

$$\mathbf{K}_S \boldsymbol{\lambda}_2 = \mathbf{f}_S \tag{4.3.10}$$

By comparing Eq. (4.3.4) and (4.3.10), we can see that the second adjoint variable $\boldsymbol{\lambda}_2$ is identical with the mechanical displacement **u**.

The second term of (4.3.7) is already derived in section 4.2.3 when the Maxwell stress tensor or the local virtual work method is used. The derivation for the body force distribution case is basically identical, and therefore it is not shown here.

4.3.5. Design results and physical explanation

To validate the above analysis and optimization approach, design of the solenoid actuator is performed. The actuator model and the fixed boundary condition for the structural analysis are shown in Figure 4.3.2. The design domain is defined at the armature, and displacement of the right boundary is fixed as zero. The volume fraction V^* is set as 0.6 and the move limit of SLP is set as 0.004. Before performing the optimization, the analytical sensitivity is verified by comparing it with the finite difference sensitivity. Figure 4.3.3(a) shows the sensitivity of the compliance, which is the first term of Eq. (4.3.7). The second term of Eq. (4.3.7), that is, the sensitivity of total magnetic force, is shown in Figure 4.3.3(b). This comparison confirms that the analytical sensitivity is in good agreement with the finite difference sensitivity.

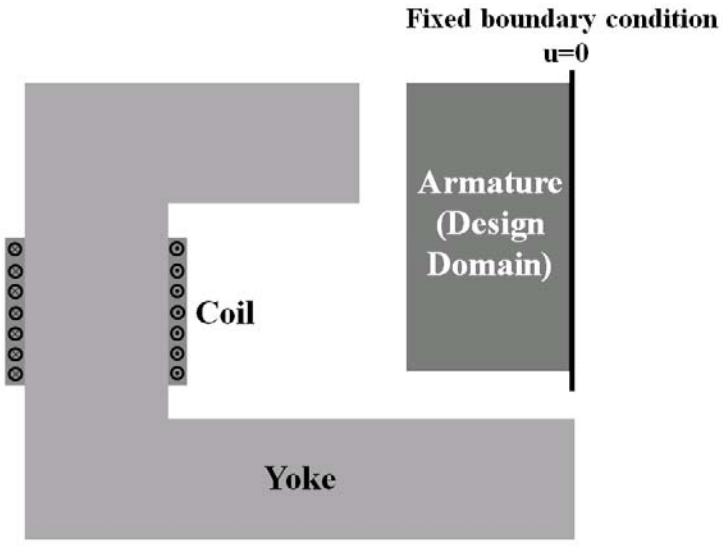

Figure 4.3.2. Magnetic actuator model and boundary condition

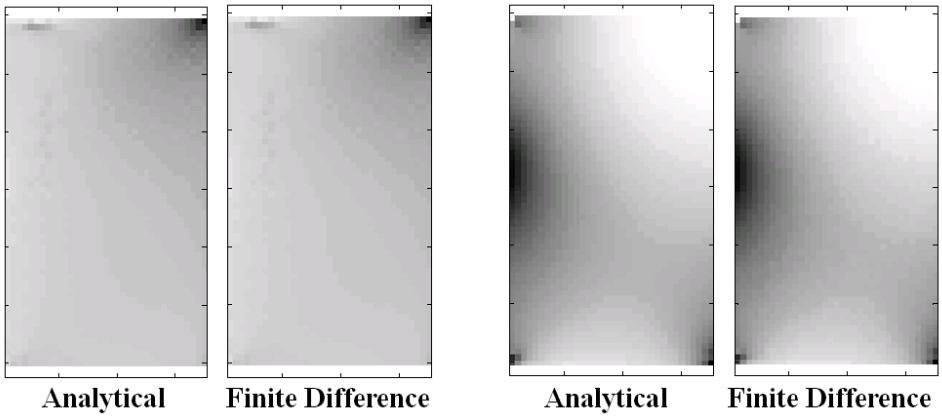

(a) (b)

Figure 4.3.3. Magnetic Comparison of the analytical and finite difference sensitivity (a) Compliance l, (b) Total magnetic force F_{tot}

The design result and its magnetic and structural analysis result are presented in Figure 4.3.4(a)-(e). As shown in Figure 4.3.4(a), the structure maximizing both the stiffness and the total magnetic force is obtained using the proposed method. For the comparison, the same design optimization is performed when the magnetic force is calculated using the CVW method proposed in [17]. The design result and its surface force distribution are presented in Figure 4.3.5(a) and (b).

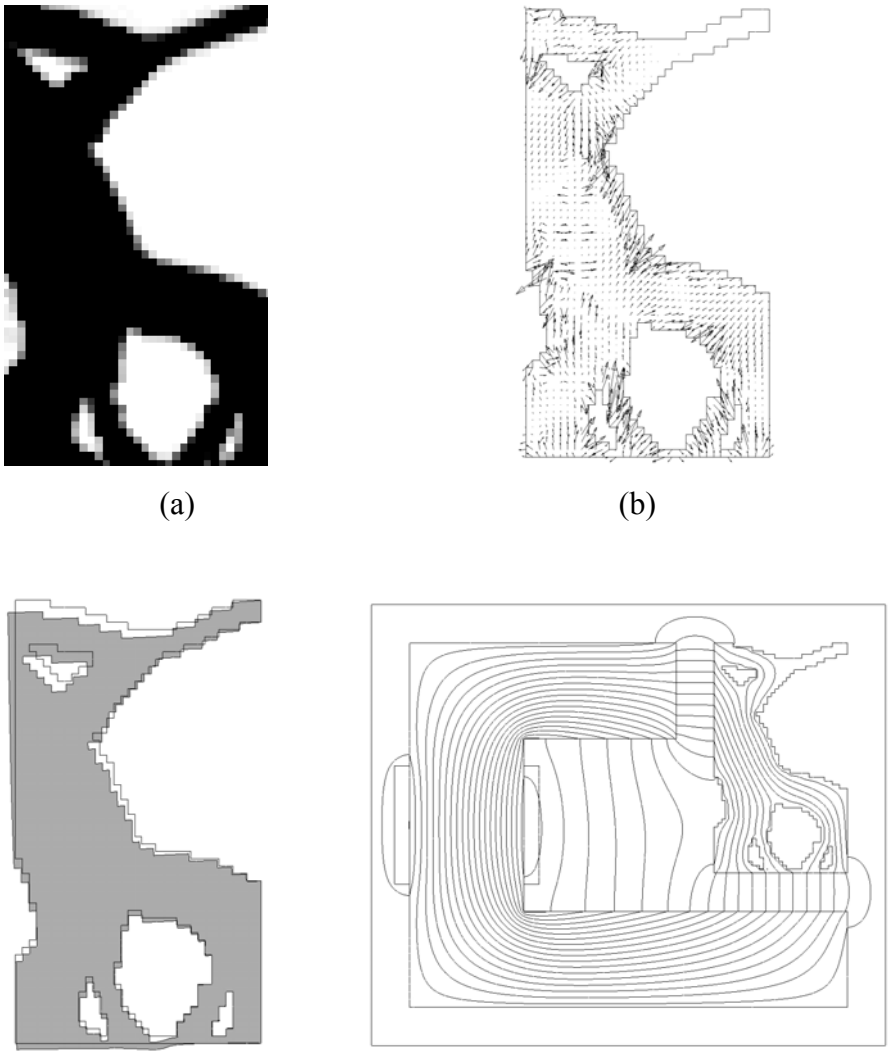

Figure 4.3.4. Armature design result (virtual air-gap scheme)
(a) Optimal shape, (b) distributed body force, (c) Deformed shape,
(d) Equipotential lines (tangential direction of magnetic flux density **B**)

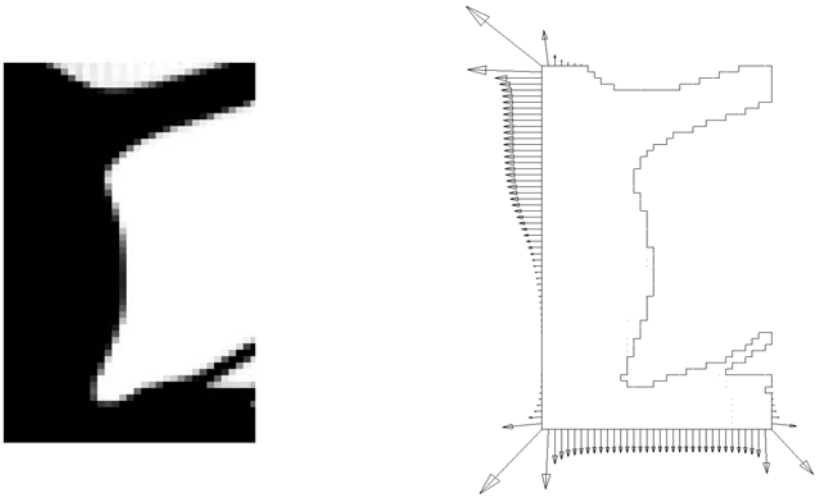

(a) (b)

Figure 4.3.5. Armature design result for comparison (CVW method)
(a) Optimal shape, (b) distributed surface force

Both optimal shapes have a similar general configuration, which is consist of main structure around left upper and bottom boundaries, and the additional structure around right upper. The main structures take a role to maximize the flow of magnetic field, which might also maximize the global magnetic force. For this role, the structures connect the left upper and bottom boundaries. In addition, a structure around the right upper takes a role to minimize the mechanical deformation by connecting the main structure and the right side fixed boundaries

In spite of a similar general configuration, two results show the difference due to the completely different local force distribution. The body force shown in Figure 4.3.4(b) spreads out over the whole structure, whereas the surface force shown in Figure 4.3.5(b) is mainly distributed at the left upper and bottom boundaries. Thus the optimal layout of

the structure shown in Figure 4.3.4(a) is rather complex, while that of Figure 4.3.5(a) tends to be simply concentrated around the left upper and bottom boundaries.

Table 4.3.1 compares the x and y directional total forces and mechanical compliance of two design results (Figure 4.3.4(a) and Figure 4.3.5(a)). The total forces of the two results are almost identical. Both results seem to maximize the total magnetic force successfully. However, the compliance of two results is entirely different due to the different force distribution. As already explained, the CVW method gives an inaccurate force distribution during the optimization. Therefore, the result using the CVW method might not guarantee stiffness maximization. In contrast, the design using the virtual air-gap scheme can maximize the stiffness caused by the body force distribution, which is accurately calculated during the optimization.

Table 4.3.1. Comparison of Magnetic Force and Mechanical Compliance

	Virtual air-gap	CVW
F_{tot_x}	-2680.22	-2685.01
F_{tot_y}	-2048.92	-2051.56
Compliance	0.6237×10^{-3}	0.2515×10^{-3}

4.3.6. Conclusion

A design method for electrical machinery is proposed to maximize both the stiffness and magnetic force. The magnetic force is calculated as the distributed body force using the virtual air-gap scheme. For accurate force calculation, the magnetic field at the material interface is corrected using the averaging scheme. To achieve the design goals, the objective function is determined as the scaled sum of the mechanical compliance and the total magnetic force. The sensitivity of the objective function is analytically derived and verified. Then, the SLP method is used to solve the optimization problem. As a design example, the armature of the solenoid actuator is optimized using the proposed optimization approach.

CHAPTER 5
TOPOLOGY OPTIMIZATION OF SWITCHED RELUCTANCE MOTORS IN LINEAR B-H RELATION

5.1. Introduction

Switched reluctance motors (SRMs) have gained in popularity over recent years due to a number of advantages they offer. First, their rugged structure is simple and robust, and the manufacturing cost is low. Second, they have a high torque/mass ratio and high efficiency. Third, their operation is reliable even at very high speeds. Therefore, SRMs have been considered as a potential candidate for electric vehicles (EVs) and hybrid electric vehicles (HEVs).

Over the past several years, there have been vigorous research activities in electromagnetic design optimization for the high performance of SRMs [59, 70-72, 130]. The design goal of those works is to meet the torque requirements such as maximizing average torque and minimizing torque ripples. The operational performance of SRMs is highly dependent on the geometries of the stator and the rotor. Therefore, size and shape optimizations have been utilized to design the geometric parameters such as air-gap length, rotor pole arc length, and stator pole arc length. However, size and shape

optimizations offer less design flexibility than topology optimization, because the topological configurations are fixed in the size and shape design. In this chapter, we consider a topological design approach to obtain the optimal geometry for high-performance SRMs with the minimum amount of material.

Topology optimization is aimed at finding the optimal layout of a structure by distributing material. The technique was first introduced by Bendsøe and Kikuchi [4], and it has been successfully applied to various engineering fields [131]. This success has led to the application of topology optimization to magnetic devices: perpendicular magnetic recording heads [132], dielectric waveguide filters [133], electromagnetic couplers [134] and magnetostrictive patches [135]. Topology optimization of SRMs have been reported in [76] and [77]. In [76], the magnetic energy profile was chosen as the objective function for the rotor design in SRMs. In [77], the design objective was to minimize the mean compliance at a fixed rotor angle for optimizing the geometry of the stator. However, those previous works have not considered the torque requirement which is an essential goal of motor design. In addition, they have optimized only the geometric design domain: the rotor in [76] and the stator in [77].

In this chapter, we take the needs of the target torque profile and the minimum mass of SRMs as the objectives of the topology optimization problem. The target torque profile may be taken as varying with respect to the rotor angle, but we set a uniform target to minimize torque ripples. We note again that the torque profile of SRMs has not yet been considered as the design objective of the topology optimization problem. Furthermore, we attempt to optimize both the geometric and the electric domain of SRMs by adding voltage on-off angles to design variables. Also, we consider both the rotor and the stator

as the geometric design domains for the topology optimization problem. The phase current of SRMs results in copper loss which affects not only thermal stress but also the drive efficiency of SRMs. Thus, we restrain copper loss by introducing constraint on the root-mean-square (RMS) value of the phase current. Using the target torque profile and constraint on the phase current, the optimization problem is formulated to find the optimal distribution of material in rotor/stator and the optimal voltage on-off angles in single-pulse voltage waveform.

The sequential linear programming (SLP) method [136] is used to solve the optimization problem. SLP is the gradient-based optimization method which requires knowledge of the sensitivity of the objective and constraint with respect to design variables. The sensitivity analysis is analytically derived using the explicit approximations of the inductance, the phase current and the torque profile. To explicitly express the inductance profile, Andrade and Krishnan [137] proposed a strategy based on Fourier series expansion. We utilize this method to explicitly determine the torque profile in a steady operation. To calculate the torque of the finite element model of SRMs, the global virtual work method [138] is used.

As a design example, the two/three dimensional model of 6/4 SRMs (6 stator poles and 4 rotor poles) is chosen. It is assumed that magnetic permeability is independent of magnetic flux density (*i.e.,* a linear SRM model is assumed). It should be noted that the proposed design method can be extended to the design optimization of a non-linear model of SRMs.

The outline of this chapter is as follows. Section 5.2 describes the performance analysis to predict the torque profile, and section 5.3 presents the optimization problem

and sensitivity analysis. Next, section 5.4 gives the design optimization results and the mechanical analysis of the optimized SRM model. Section 5.5 summarizes the chapter.

5.2. Performance analysis of SRMs

The performance analysis of SRMs [45, 139, 140] can be summarized as follows. First, the magnetostatic problem is solved using the finite element method at several given rotor angles. Then, the inductances at rotor angles are calculated and approximated by a Fourier series to attain the explicit expression of the inductance curve. Next, we solve the voltage equation to obtain the phase current. Consequently, the torque profile is explicitly determined using the global virtual work method, and it is analytically differentiable.

5.2.1. Inductance curve

Magnetostatic analysis

Maxwell's equation describing the magnetostatic field is

$$\nabla \times \mathbf{H} = \mathbf{J} \tag{5.2.1}$$

$$\nabla \cdot \mathbf{B} = 0 \tag{5.2.2}$$

$$\mathbf{H} = \nu \mathbf{B} \tag{5.2.3}$$

where **H** is the magnetic field intensity, **J** is the source current density, **B** is the magnetic flux density, and v is the magnetic reluctivity. The divergence-free field **B** introduces a magnetic vector potential **A**

$$\mathbf{B} = \nabla \times \mathbf{A} \tag{5.2.4}$$

Then, Eq. (5.2.1) becomes

$$\nabla \times \left(\nu \nabla \times \mathbf{A} \right) = \mathbf{J} \tag{5.2.5}$$

In two dimensional analysis, we can assume that the current density **J** has only a z-direction component [141]. Likewise, the magnetic vector potential **A** has only a z-direction component. Then, we obtain the following Poisson equation

$$-\frac{\partial}{\partial x}\left(\nu \frac{\partial A_z}{\partial x} \right) - \frac{\partial}{\partial y}\left(\nu \frac{\partial A_z}{\partial y} \right) = J_z \tag{5.2.6}$$

Eq. (5.2.6) is solved using the finite element method. Figure 5.2.1 (a) shows the two dimensional finite element mesh of 6/4 SRMs and Figure 5.2.1 (b) illustrates the equipotential line, which is calculated from the finite element analysis. In Figure 5.2.1 (a), the voltage of the coil at the stator pole 'S_1' is turned on, and the angle of the rotor pole 'R_1' is 15°. In this work, the rotor angle is measured from the unaligned position. In Figure 5.2.1, the rotor pole 'R_1' is rotated clockwise by 15° from its unaligned position.

The rotor pole 'R_1' becomes unaligned with the stator pole 'S_1' when the stator pole 'S_1' is at an exact midpoint between the rotor poles 'R_1' and 'R_2'.

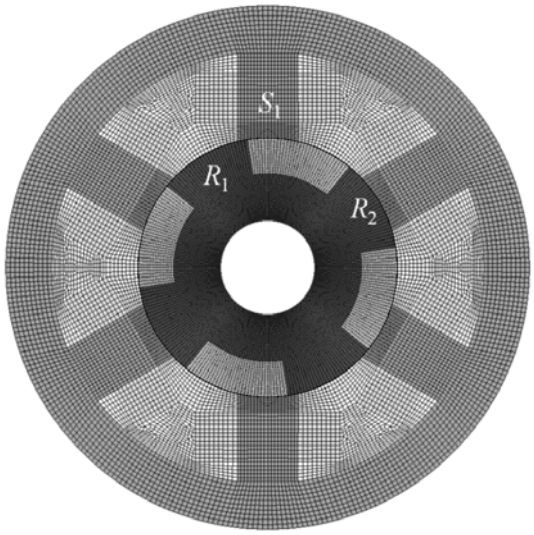

(a)

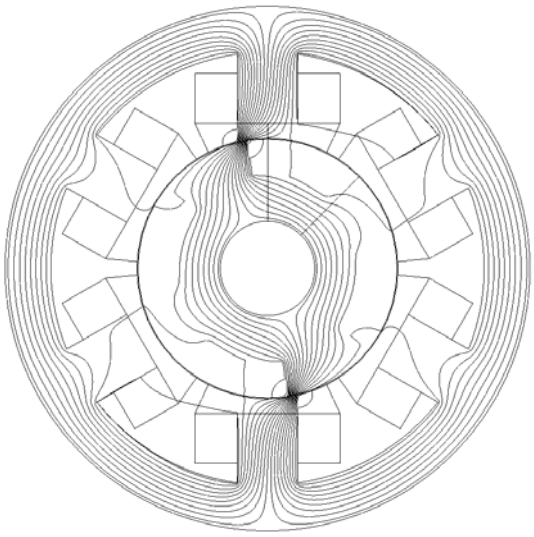

(b)

Figure 5.2.1. Two dimensional finite element analysis (rotor angle=15˚)
(a) finite element mesh, (b) analysis result (equipotential line)

Inductance calculation

The inductance curve of SRMs can be fitted using a small number of the inductance values at the rotor angles where the inductance largely changes. However, considering the design variation during optimization, the inductance values are needed at many different rotor angles. Therefore, finite element analysis is carried out at several rotor angles which are rather closely spaced from the unaligned position to the aligned position.

The magnetostatic energy W_m in a linear material is defined as

$$W_m = \frac{1}{2} l_j i^2 \tag{5.2.7}$$

where l_j is the inductance at the rotor angle θ_j, and i is the current on the coil. From the finite element analysis, the magnetic flux density is calculated by Eq. (5.2.4) and then the magnetostatic energy W_m of the finite element model is obtained by

$$W_m = \frac{1}{2} \int_{\text{all space}} \nu B^2 dA \tag{5.2.8}$$

By equating Eq. (5.2.7) and Eq. (5.2.8), the inductance l_j at the rotor angle θ_j is expressed as

$$l_j = \frac{1}{i^2} \int_{\text{all space}} \nu B^2 dA \tag{5.2.9}$$

Fourier series approximation

The inductance curve can be explicitly represented by the method proposed in [137]. The piecewise line segments bridging discrete inductance values are approximated by a Fourier series. As a result, the attained inductance curve has C^1 continuity, which is necessary to use the global virtual work method of calculating the torque profile.

The equation of the piecewise line segment connecting the inductances at θ_{j+1} and θ_j is

$$L_{(line)j}(\theta) = \left(\frac{l_{j+1} - l_j}{\theta_{j+1} - \theta_j} \right) \theta + \left(l_j - \frac{l_{j+1} - l_j}{\theta_{j+1} - \theta_j} \theta_j \right) \tag{5.2.10}$$

Because the inductance curve is an even function, the cosine Fourier series of the inductance is given by

$$L(\theta) = L_0 + \sum_{n=1}^{NF} L_n \cos(nP_r\theta) \tag{5.2.11}$$

where NF is the number of Fourier series terms and P_r is the number of rotor poles. From Eq. (5.2.10), we obtain Fourier series coefficients L_0 and L_n

$$L_0 = \frac{1}{2\pi / P_r} \sum_{j=1}^{m} \left(\left(l_{j+1} + l_j \right) \left(\theta_{j+1} - \theta_j \right) \right) \tag{5.2.12}$$

$$L_n = \frac{2}{n\pi}\sum_{j=1}^{m}\left[\left(l_{j+1}\right)\cdot\left(\sin\left(nP_r\theta_{j+1}\right)+\frac{\cos\left(nP_r\theta_{j+1}\right)-\cos\left(nP_r\theta_j\right)}{nP_r\left(\theta_{j+1}-\theta_j\right)}\right)\right.$$
$$\left.-\left(l_j\right)\cdot\left(\sin\left(nP_r\theta_j\right)+\frac{\cos\left(nP_r\theta_{j+1}\right)-\cos\left(nP_r\theta_j\right)}{nP_r\left(\theta_{j+1}-\theta_j\right)}\right)\right] \tag{5.2.13}$$

where m is the number of piecewise line segments. Figure 5.2.2 shows the attained inductance curve corresponding to the 6/4 SRM model as described in Figure 5.2.1. The filled circular marks represent the calculated inductance values at the given rotor angles. As shown in Figure 5.2.2, the inductance curve is smoothly approximated by Fourier series expansion.

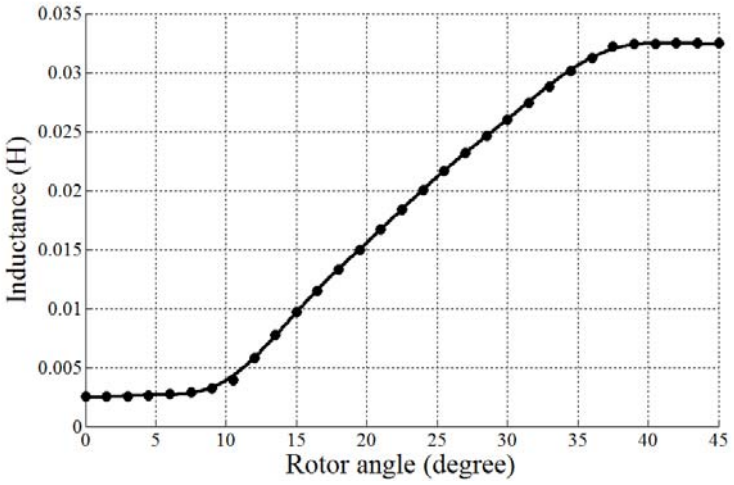

Figure 5.2.2. Example of the inductance curve

5.2.2. Phase current curve

The next step in the performance analysis is to calculate the phase current. The voltage equation of SRMs is given by

$$V = Ri + \frac{d\Phi(i,\theta)}{dt} \tag{5.2.14}$$

where V is the source voltage, R is the coil resistance and Φ is the flux linkage. Figure 5.2.3 shows the single-pulse voltage waveform used in this work. The voltage V is positive (V_0) between the voltage-on angle θ_{on} and the mid-angle θ_{mid}, while negative ($-V_0$) between the mid-angle θ_{mid} and the voltage-off angle θ_{off}. The mid-angle θ_{mid} is an exact midpoint of the voltage-on θ_{on} and the voltage-off angle θ_{off} in order to make the phase current zero at the voltage-off angle θ_{off}.

The flux linkage in a linear material can be written as

$$\Phi(i,\theta) = L(\theta) \cdot i(\theta) \tag{5.2.15}$$

In order to analytically solve Eq. (5.2.14), we neglect the voltage drop due to the coil resistance. Thus, the voltage equation (5.2.14) together with Eq. (5.2.15) then yields

$$V = \frac{d\left(L(\theta) \cdot i(\theta)\right)}{dt} \tag{5.2.16}$$

We assume steady-state rotation and the zero current at the voltage-on angle. Then, integrating Eq. (5.2.16) with the single-pulse voltage pulse waveform as shown in Figure 5.2.3, we obtain the following explicit expression of the phase current

$$i(\theta)=\begin{cases}\dfrac{V_0(\theta-\theta_{on})}{\omega\left(L_0+\sum_{n=1}^{NF}L_n\cos(nP_r\theta)\right)} & (\theta_{on}\le\theta<\theta_{mid})\\ \dfrac{V_0(\theta_{off}-\theta)}{\omega\left(L_0+\sum_{n=1}^{NF}L_n\cos(nP_r\theta)\right)} & (\theta_{mid}\le\theta<\theta_{off})\\ 0 & (\theta<\theta_{on},\ \theta\ge\theta_{off})\end{cases} \tag{5.2.17}$$

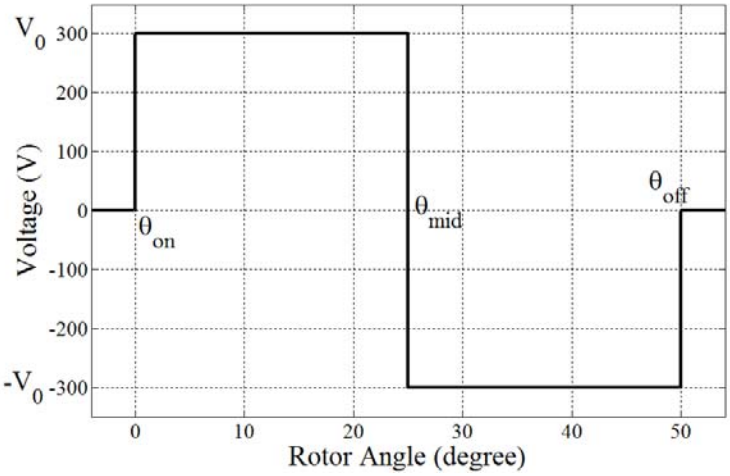

Figure 5.2.3. Single-pulse voltage waveform

5.2.3. Single-phase torque profile

The torque profile of SRMs is calculated using the global virtual work method [138]. The global virtual work method is based on the principle of conservation of energy and virtual displacement. This method uses the coenergy at a set of closely spaced positions of the rotor part. The coenergy W_{co} is defined as

$$W_{\text{co}} = \int_0^{i_1} \Phi \, di \Big|_{\theta=\text{constant}} \tag{5.2.18}$$

By taking the derivative of the total coenergy with respect to the rotor angle θ, the torque is obtained

$$T(i,\theta) = \frac{\partial W_{\text{co}}}{\partial \theta} \Big|_{i=\text{constant}} \tag{5.2.19}$$

In a linear material, Eq. (5.2.19) can be simplified to

$$T(i,\theta) = \frac{1}{2} i^2 \frac{dL(\theta)}{d\theta} \tag{5.2.20}$$

Substituting Eq. (5.2.11) and Eq. (5.2.17) into Eq. (5.2.20), the explicit expression of the torque profile is given by

$$T(\theta)=\begin{cases}\dfrac{1}{2}\left(\dfrac{V(\theta-\theta_{\text{on}})}{\omega\left(L_0+\sum_{n=1}^{NF}L_n\cos(nP_r\theta)\right)}\right)^2\left(-n\,\mathrm{P_r}\sum_{n=1}^{NF}L_n\sin(nP_r\theta)\right) & (\theta_{\text{on}}\le\theta<\theta_{\text{mid}}) \\ \dfrac{1}{2}\left(\dfrac{V(\theta_{\text{off}}-\theta)}{\omega\left(L_0+\sum_{n=1}^{NF}L_n\cos(nP_r\theta)\right)}\right)^2\left(-n\,\mathrm{P_r}\sum_{n=1}^{NF}L_n\sin(nP_r\theta)\right) & (\theta_{\text{mid}}\le\theta<\theta_{\text{off}}) \\ 0 & (\theta<\theta_{on},\,\theta\ge\theta_{off}) \end{cases} \tag{5.2.21}$$

5.2.4. Total torque profile

In the above, we obtained the single-phase torque profile of SRMs (*i.e.,* the torque profile when the voltage of a single pair of the stator poles is switched on and off). Since one phase is overlapped with the previous or the next phase in SRMs, the two consecutive single-phase torque profiles are summed in the overlapped range. After summing the torque profiles in all phases, the total torque profile is determined.

The overlapped range depends on the number of rotor poles P_r and stator poles P_s. The rotor pole repeats its position after the rotor period of $2\pi/P_r$. During this period, the rotor pole passes $P_s/2$ stator poles. Therefore, the single-pulse torque profile is overlapped every P_{torque}

$$P_{torque}=\frac{2\pi/P_r}{P_s/2}=\frac{4\pi}{P_rP_s} \tag{5.2.22}$$

In a steady rotation, the torque profiles of all phases are identical. Therefore, the total torque is given by

$$T_{tot}(\theta) = \sum_{m=1}^{2\pi/P_t} T\left(\theta + (m-1)P_{torque}\right) \tag{5.2.23}$$

Figure 5.2.4 shows three consecutive single-phase torque profiles and the total torque profile of the SRM model shown in Figure 5.2.1. In this example, the voltage on-off angles are set to -2˚ and 48˚ respectively. The single-phase torque exists between these two angles, and repeats every 30˚. (*i.e.,* P_{torque} is 30˚). As illustrated in Figure 5.2.4, SRMs have inherently large torque ripples.

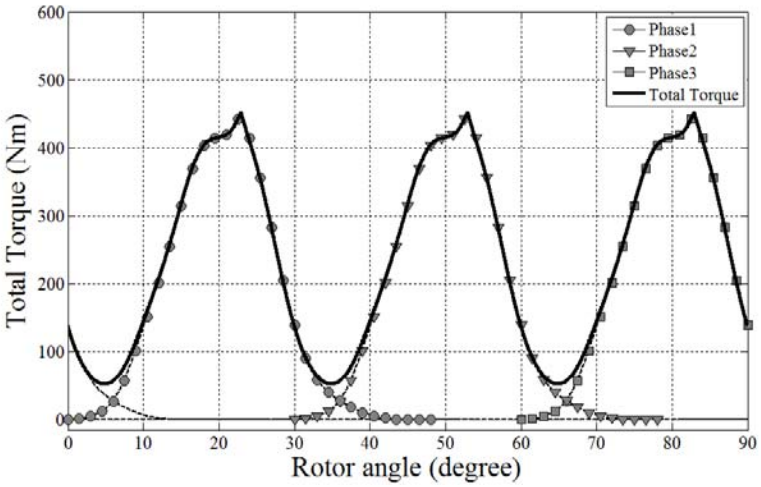

Figure 5.2.4. Single-phase torques (gray) and total torque (black)

5.3. Design optimization of SRMs

5.3.1. Design strategy

As with the conventional topology optimization method, the density design variables are relaxed to use a continuous mathematical programming method such as SLP. The material becomes air when the material density is zero (*i.e.,* void) and steel when the material density is one (*i.e.,* solid). To specify the material property of intermediate material densities, we utilize the interpolation of reluctivity $v(\rho)$ proposed in [142]. The interpolation of permeability μ, previously used in [143], causes distortion of the design sensitivity and results in unstable optimization. This instability can be avoided by using the interpolation of reluctivity v

$$\nu_k(\rho_k) = \nu_{steel}\rho_k{}^p + \nu_{air}\left(1-\rho_k{}^p\right) \tag{5.3.1}$$

where v_{air} is the reluctivity of air, v_{steel} is the reluctivity of steel, ρ_k is the element density of k^{th} element and p is the penalization power.

The geometric design domain is shown in Figure 5.3.1. Since 6/4 SRMs is chosen, the 1/8 part of the rotor and the 1/12 part of the stator is considered as the geometric design domain. Then, the material densities in geometric design domain are reflected and copied to the corresponding symmetric and periodic part of the rotor and stator. Using this approach, the symmetries in the rotor and the stator of SRMs are assured.

The design optimization with minimizing mass could yield a geometric design with a very thin member, which results in high current densities. High current can damage

electronics, cause high energy loss and consequently increase thermal stress. Furthermore, to maximize the drive efficiency of SRMs, we need to minimize the copper loss in coils. Therefore, we constrain the RMS value of the phase current. Without the current constraint, the optimized SRMs could result in high copper loss which leads to low efficiency and high temperature rise.

The design problem consists of two different disciplinary fields (*i.e.,* the design of multidisciplinary systems): (1) optimizing the rotor and the stator as the geometric design domain in which the magnetostatic analysis is performed, and (2) optimizing the voltage on-off angles as the electric design domain, in which the voltage equation is solved. In this work, we formulate a single design optimization problem for treating those two disciplines, that is, a simultaneous optimization. In the context of multidisciplinary design optimization (MDO), there could be various strategies to formulate the design problem of SRMs in order to treat more physical disciplines, such as vibration quality and thermal characteristic of SRMs; they are left for further research.

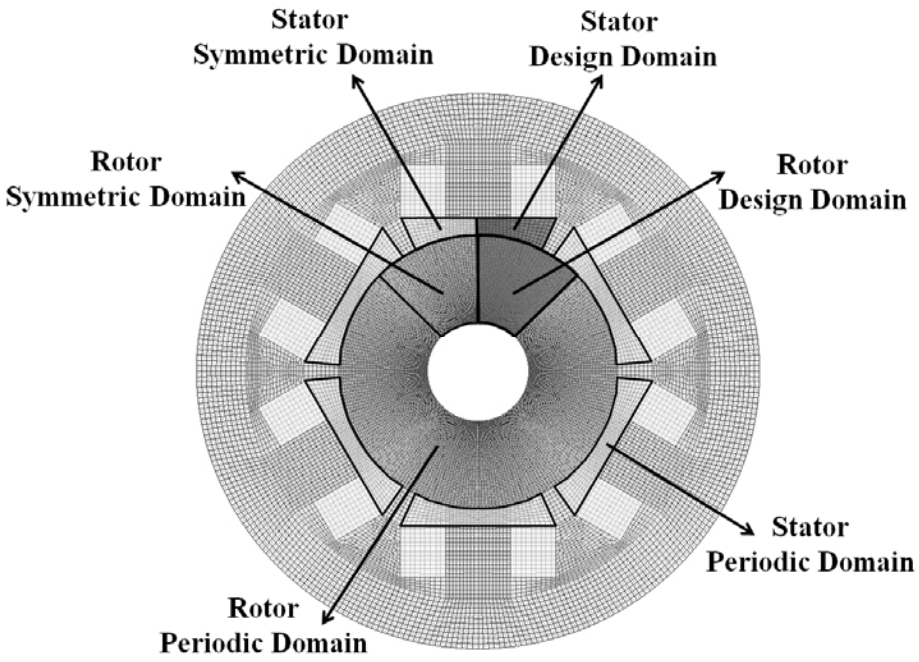

Figure 5.3.1. Geometric design domain in rotor and stator

5.3.2. Formulation of the optimization problem

The design objectives are to match the total torque profile with the target average torque and to minimize the mass of the rotor. To achieve those objectives under the current constraint, the optimal design problem can be formulated as

$$\text{Minimize } f = \left[\sum_{j=1}^{\text{n}} \left(\frac{T_{tot,j}}{T^*} - 1.0 \right)^2 + \alpha \cdot f_c(\boldsymbol{\rho}) + \beta \cdot V(\boldsymbol{\rho}) \right] \tag{5.3.2}$$

$$\text{subject to} \quad 0 < \rho_{\min} \le \rho_k \le \rho_{\max} \qquad (k = 1,..,ND) \tag{5.3.3}$$

$$i_{rms} \le i_{rms}^* \tag{5.3.4}$$

$$f_c(\boldsymbol{\rho}) = \sum_{k=1}^{ND} \frac{\rho_k (1 - \rho_k)}{ND} \tag{5.3.5}$$

$$V(\boldsymbol{\rho}) = \sum_{\text{k}} \rho_k a_k \; / \sum_{\text{k}} a_k \tag{5.3.6}$$

where $T_{tot,j}$ is the total torque value at j^{th} rotor angle θ_j ($j = 1, \cdots, n$), n is the number of discrete rotor angles, T^* is the target average torque, a_k is the area of k^{th} element, α and β are the weighting values for the density convergence function $f_c(\boldsymbol{\rho})$ and the normalized rotor mass function $V(\boldsymbol{\rho})$ respectively, and ND is the number of design variables.

With this formulation, we manipulate the torque values at given rotor angles and consequently reduce the torque ripple. The additional objectives are introduced to penalize the density convergence and to minimize the mass of the rotor. In [144], the penalty function was used to enforce the convergence of intermediate densities. In [145], the same function was used to measure the discreteness of the optimized density distribution. We use the same penalty function normalized by the number of design variables. Unlike the conventional topology optimization, we add the normalized mass function to the objective in order to minimize the mass of the rotor.

As suggested in [146], we need to gradually increase the non-convex term in the optimization process. Since the density convergence function $f_c(\boldsymbol{\rho})$ is non-convex, we adaptively increase its weighting value based on the satisfaction of the desired torque profile. Thus, the weightings α and β are controlled by the reciprocal value of the difference between the total torque and the target average torque.

$$\alpha = \frac{\alpha_0}{\sum_{j=1}^{\mathrm{n}} \left(\frac{\left(T_{tot}\right)_j}{T^*} - 1.0 \right)^2}, \quad \beta = \frac{\beta_0}{\sum_{j=1}^{\mathrm{n}} \left(\frac{\left(T_{tot}\right)_j}{T^*} - 1.0 \right)^2} \tag{5.3.7}$$

where α_0 and β_0 are prescribed constants and determined empirically. We assume that the difference between the total torque profile and the target average torque is large at the beginning of the optimization process and it decreases as the iteration goes on. Thus, the weighting values are magnified as much as the torque objective is satisfied. Furthermore, by using this adaptive strategy, the optimization is focused more on the density penalization and the mass minimization as the design evolves. We note that these weightings are ignored in the design sensitivity analysis of the objective function.

In Eq. (5.3.4), the RMS value of the phase current is given by

$$i_{rms} = \sqrt{\frac{1}{T_e}\int_0^{T_e} i^2 dt} \approx \sqrt{\frac{1}{2\pi / P_r}\sum_{j=1}^{n} {i_j}^2 \cdot \frac{2\pi / P_r}{n}} \tag{5.3.8}$$

where T_e is the period of each phase, i_j is the phase current at j^{th} discrete rotor angle θ_j ($j=1,...,n$), and P_r is the number of rotor poles. Using the constraint on the RMS value of the phase current, we can confine the copper loss which is one of main heat sources and is written as

$$W_{copper} = R \cdot i_{rms}{}^2 \tag{5.3.9}$$

where R is the resistance of one phase of the motor.

5.3.3. Sensitivity analysis and verification

In section 5.2, we obtained the explicit representation of the torque and the phase current using Fourier series expansion. Now, we calculate the analytical sensitivity of the objective (5.3.2) and constraint (5.3.4) using the direct differentiation and the chain rule. The derivative of (5.3.2) with respect to density design variables can be written as

$$\frac{df}{d\rho_k} = \sum_{j=1}^{n} 2\left(\frac{(T_{tot})_j}{T^*} - 1.0\right)\frac{\partial(T_{tot})_j}{\partial\rho_k} + \alpha\frac{1-2\rho_k}{ND} + \beta \cdot a_k \tag{5.3.10}$$

This result requires the evaluation of $\partial(T_{tot})_j / \partial\rho_k$. From Eq. (5.2.23), the derivative of the total torque $\partial(T_{tot})_j / \partial\rho_k$ is written as

$$\frac{\partial\left(T_{tot}\right)_j}{\partial\rho_k}=\sum_{m=1}^{2\pi/P_r}\frac{\partial\left(T\left(\theta_j+\left(m-1\right)P_{torque}\right)\right)}{\partial\rho_k} \tag{5.3.11}$$

Next, we calculate the derivative of the torque $\partial T/\partial\rho_k$ from Eq. (5.2.21). Since the rotor angle θ in Eq. (5.2.21) is not a function of ρ_k, the derivative of the torque can be easily obtained by applying the direct differentiation and the chain rule. The derivations are easy, but lengthy. For brevity, we describe $\partial T/\partial\rho_k$ when $\theta_{on}\le\theta<\theta_{mid}$ and m=1:

$$\begin{aligned}\frac{\partial T\left(\theta\right)}{\partial\rho_k}=&\frac{1}{2}\left(\frac{V\left(\theta-\theta_{on}\right)}{\omega\left(L_0+\sum_{n=1}^{NF}L_n\cos\left(nP_r\theta\right)\right)}\right)^2\left(-nP_r\sum_{n=1}^{NF}\frac{\partial L_n}{\partial\rho_k}\sin\left(nP_r\theta\right)\right)\\&-\left(\frac{V\left(\theta-\theta_{on}\right)}{\omega}\right)^2\left(L_0+\sum_{n=1}^{NF}L_n\cos\left(nP_r\theta\right)\right)^{-3}\\&\times\left(\frac{\partial L_0}{\partial\rho_k}+\sum_{n=1}^{NF}\frac{\partial L_n}{\partial\rho_k}\cos\left(nP_r\theta\right)\right)\left(-nP_r\sum_{n=1}^{NF}L_n\sin\left(nP_r\theta\right)\right)\end{aligned} \tag{5.3.12}$$

All terms in Eq. (5.3.12) are explicitly calculated except $\partial L_n/\partial\rho_k$ and $\partial L_0/\partial\rho_k$. From Eq. (5.2.12) and Eq. (5.2.13), $\partial L_0/\partial\rho_k$ and $\partial L_n/\partial\rho_k$ can be written as

$$\frac{\partial L_0}{\partial\rho_k}=\frac{1}{2\pi/P_r}\sum_{j=1}^{m}\left(\left(\frac{\partial l_{j+1}}{\partial\rho_k}+\frac{\partial l_j}{\partial\rho_k}\right)\left(\theta_{j+1}-\theta_j\right)\right) \tag{5.3.13}$$

$$\frac{\partial L_n}{\partial \rho_k} = \frac{2}{n\pi}\sum_{j=1}^{m}\left[\left(\frac{\partial l_{j+1}}{\partial \rho_k}\right)\cdot\left(\sin\left(nP_r\theta_{j+1}\right)+\frac{\cos\left(nP_r\theta_{j+1}\right)-\cos\left(nP_r\theta_j\right)}{nP_r\left(\theta_{j+1}-\theta_j\right)}\right)\right.$$
$$\left.-\left(\frac{\partial l_j}{\partial \rho_k}\right)\cdot\left(\sin\left(nP_r\theta_j\right)+\frac{\cos\left(nP_r\theta_{j+1}\right)-\cos\left(nP_r\theta_j\right)}{nP_r\left(\theta_{j+1}-\theta_j\right)}\right)\right] \tag{5.3.14}$$

where l_j is the inductance at rotor angle θ_j obtained in Eq. (5.2.9). The derivative of the inductance $\partial l_j / \partial \rho_k$ requires the derivative of the magnetostatic energy $\partial W_m / \partial \rho_k$. Using the adjoint method [9], the derivative of the magnetostatic energy can be written as

$$\frac{\partial W_m}{\partial \rho_k} = \int_{\text{all space}} \frac{\partial \nu}{\partial \rho_k} B^2 dA \tag{5.3.15}$$

From Eq. (5.3.1) and Eq. (5.3.15), the derivative of the inductance $\partial l_j / \partial \rho_k$ is

$$\frac{\partial l_j}{\partial \rho_k} = \frac{1}{i^2}\int_{k^{\text{th}}\ \text{element}} \left[p\left(\nu_{steel}-\nu_{air}\right)\rho_k{}^{p-1}\right] B^2 dA \tag{5.3.16}$$

In summary, the analytical sensitivity of the objective function can be calculated by using Eq. (5.3.10)-(5.3.16).

Next, the analytical sensitivity of the current constraint (5.3.4) is described. In a similar way, we directly differentiate the constraint function (5.3.8) using the chain rule. Then, we obtain

$$\frac{\partial i_{rms}}{\partial \rho_k} \cong \left(\frac{1}{n} \sum_{j=1}^{n} i_j \cdot \frac{\partial i_j}{\partial \rho_k} \right) / \sqrt{\frac{1}{n} \sum_{j=1}^{n} i_j^{\,2}} \tag{5.3.17}$$

From Eq. (5.2.17), $\partial i_j / \partial \rho_k$ can be written as

$$\frac{\partial i_j}{\partial \rho_k} = \begin{cases} -\dfrac{V\left(\theta_j - \theta_{\text{on}}\right)\left(\dfrac{\partial L_0}{\partial \rho_k} + \displaystyle\sum_{n=1}^{NF} \frac{\partial L_n}{\partial \rho_k} \cos\left(n \, \text{P}_\text{r} \, \theta\right) \right)}{\omega \left(L_0 + \displaystyle\sum_{n=1}^{NF} L_n \cos\left(n \, \text{P}_\text{r} \, \theta_j\right) \right)^2} & \left(\theta_{\text{on}} \le \theta < \theta_{\text{mid}}\right) \\ -\dfrac{V\left(\theta_{\text{off}} - \theta_j\right)\left(\dfrac{\partial L_0}{\partial \rho_k} + \displaystyle\sum_{n=1}^{NF} \frac{\partial L_n}{\partial \rho_k} \cos\left(n \, \text{P}_\text{r} \, \theta\right) \right)}{\omega \left(L_0 + \displaystyle\sum_{n=1}^{NF} L_n \cos\left(n \, \text{P}_\text{r} \, \theta_j\right) \right)^2} & \left(\theta_{\text{mid}} \le \theta < \theta_{\text{off}}\right) \\ 0 & \left(\theta < \theta_{on}, \, \theta \ge \theta_{off}\right) \end{cases} \tag{5.3.18}$$

The analytical sensitivity of the objective and the current constraint is compared to the finite-difference sensitivity [147], and verified. The finite-difference sensitivity of $F(\boldsymbol{\rho})$ can be written as

$$\frac{\partial F(\boldsymbol{\rho})}{\partial \rho_i} \cong \frac{F(\boldsymbol{\rho})\big|_{\rho_i + \Delta\rho_i} - F(\boldsymbol{\rho})\big|_{\rho_i}}{\Delta \rho_i} \tag{5.3.19}$$

In order to calculate the finite-difference sensitivity, we need to carry out the performance analysis twice per every design variable. Due to a large number of design variables in topology optimization, the cost of calculating the finite- difference sensitivity is too expensive to employ. In this work, the finite-difference sensitivity is used only to verify the analytical sensitivity. Figure 5.3.2 shows the analytical and finite-difference sensitivity of the torque objective (a) and the current constraint (b). As shown in Figure 5.3.2, the analytical sensitivity is in good agreement with the finite-difference sensitivity.

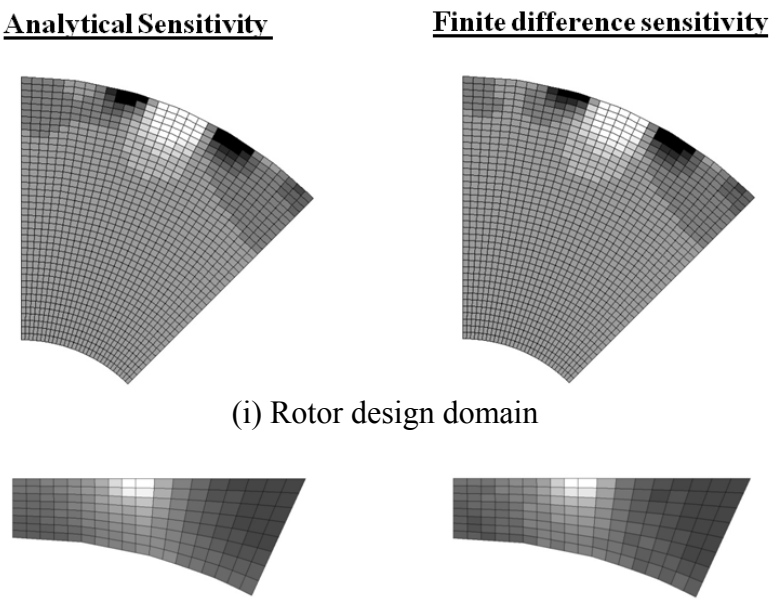

(i) Rotor design domain

(ii) Stator design domain

(a)

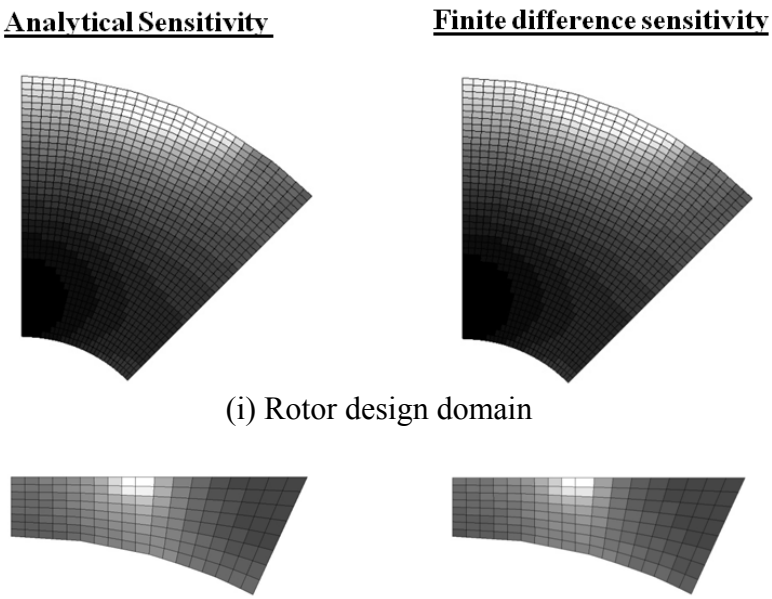

(i) Rotor design domain

(ii) Stator design domain

(b)

Figure 5.3.2. Comparison of the analytical sensitivity and finite different sensitivity (a) objective (total torque T_{tot}), (b) constraint (phase current i)

5.4. Design examples

The proposed design optimization method is applied to two/three dimensional 6/4 SRMs. Table 5.4.1 shows the basic specification of the SRM model used here. The target average torque T^* is the same as the average torque of the initial design. The RMS value of the phase current is constrained by the RMS value of the initial design. The angular velocity ω is set to 104.72 rad/s (*i.e.,* 1000 rpm). As shown in Eq. (5.2.21), the overall torque profile is inversely proportional to the squared angular velocity ω^2. Thus, the optimized designs are also effective in minimizing ripples in case of different angular velocity in a steady rotation, although we perform the design optimization under a specific angular velocity (*i.e.,* 1000 rpm).

The initial densities in the geometric design domain (*i.e.,* rotor and stator) are uniformly given as 0.65. The voltage on-off angles are initially set to 5˚ and 50˚. The move limits of the SLP method are set to 0.004 for density design variables and 0.0004 for angle design variables.

Table 5.4.1. Basic Specification of SRM

Stator poles/rotor poles	6/4	Thickness (mm)	50
Stator outer diameter (mm)	150	The number of phase	3
Stator inner diameter (mm)	123.9	Airgap (mm)	0.5
Rotor outer diameter (mm)	74.2	The number of windings	15
Rotor inner diameter (mm)	27.1	DC Voltage (V)	300

5.4.1. Two dimensional SRM design result

The initial shape and the optimized shape are shown in Figure 5.4.1 (a) and (b). As shown in Figure 5.4.1 (b), the density design variables are clearly converged to zero (void) or one (steel) by Eq. (5.3.5). The optimized rotor has holes which hinder the flowing of magnetic flux through the rotor and consequently decrease the inductance profile as the rotor approaches to its aligned position. Additionally, the created holes contribute to reducing the mass of rotor from 71.3% (initial model) to 46.4% (optimized model). Note that topology optimization of the rotor for the desired magnetic energy profile has developed the smoothly rounded shape in [76]. Unlike the result in [76], the notched pole near the airgap is designed to satisfy the torque requirements. This notched shape is in good agreement with the shape design result of torque ripple minimization (see [70, 148]). Thin members could cause vibration noise and fail with external loadings. To avoid these structural weaknesses, minimum compliance design or minimum member-size control could be employed in further research.

Table 5.4.2 shows the design parameters (*i.e.,* arc lengths of poles and voltage on-off angles) of the initial and optimized SRM model, and also compares the average torques and the RMS values of the phase current. As shown in Table 5.4.2, the optimized shape has the increased arc lengths of both the rotor and the stator poles in order to minimize torque ripples. As reported in [139], increasing the arc lengths of poles in SRMs is the solution to minimizing torque ripples. This feature is well observed in the optimized design. As electric design variables, the voltage-on angle falls while the voltage-off angle

rises; the range of the voltage on-off angles is widened and thus the overlapped period of each phase is increased in the optimized model.

In Figure 5.4.1 (c)-(e), the inductance, the phase current and the total torque profile of the initial design (dashed lines) are compared to those of the optimized design (solid lines). As shown in Figure 5.4.1 (c), the inductance curve of the optimized model slowly elevates and ends with a slightly decreased value, compared to the initial model. In Figure 5.4.1 (d), the operating range of the phase current increases in accordance with the widened voltage waveform. By satisfying the current constraint, the narrow current profile in the initial model gets spread and disappears in the optimized model. The maximum value of the phase current is notably decreased after optimization. As shown in Figure 5.4.1 (e), the total torque profile of the optimized design is nearly matched with the target torque, and the torque ripple is remarkably attenuated.

From the author's experiences, the design optimization with the current constraint hardly satisfies the higher average torque than that of the initial design. It seems that the design space is quite reduced by constraining the RMS value of the phase current. Possibly, the input power is also confined in a relaxed way because it is estimated by the integration of the phase current multiplied by the voltage profile, which is a fixed single-pulse waveform in this work.

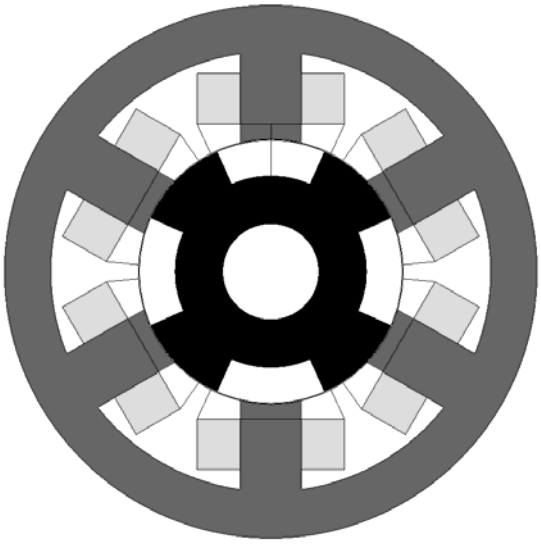

(a)

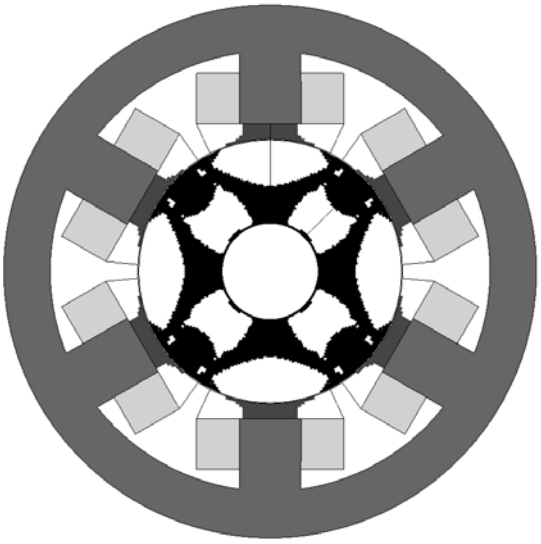

(b)

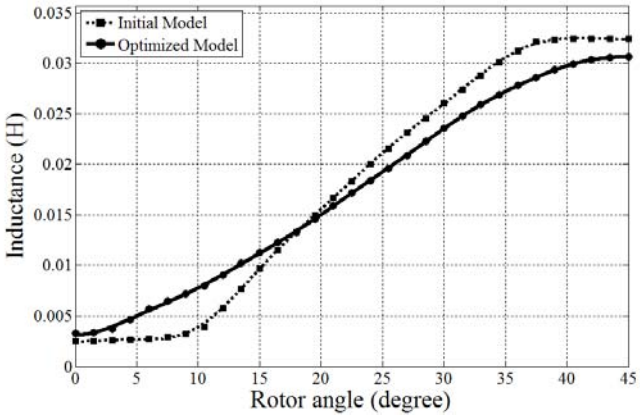

(c)

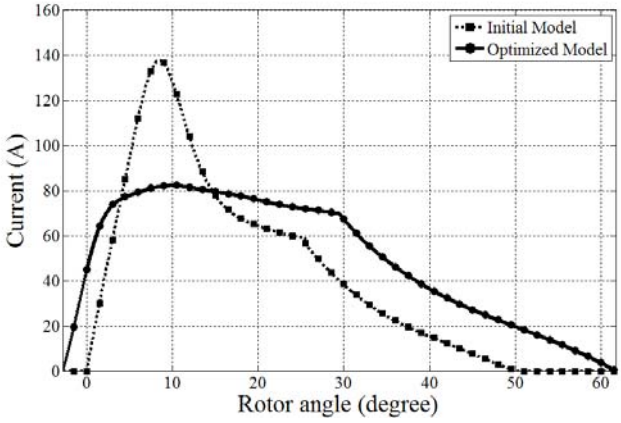

(d)

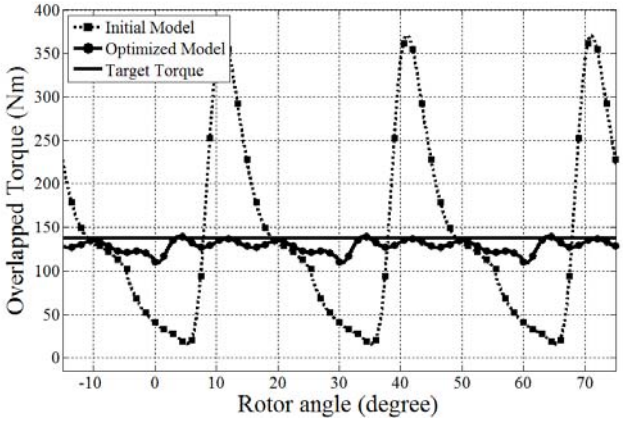

(e)

Figure 5.4.1. Rotor design result

(a) initial shape, (b) optimized shape,

(b) inductance curve, (d) phase current curve (e) total torque curve

Table 5.4.2. Design parameters and performance analysis result

Initial model		Optimized model	
Stator pole arc (degree)	27	Stator pole arc(degree)	39
Rotor pole arc (degree)	42	Rotor pole arc(degree)	45
Voltage-on angle θ_{on} (degree)	0	Voltage-on angle θ_{on} (degree)	-2.8
Voltage-off angle θ_{off} (degree)	50	Voltage-off angle θ_{off} (degree)	61.7
Average torque (Nm)	138.5	Average torque (Nm)	128.5
RMS value of phase current (A)	48.1	RMS value of phase current (A)	48.1

5.4.2. Mechanical analysis of two dimensional SRM design result

In order to investigate the mechanical characteristics of the optimized SRM, modal analysis [50, 149, 150] and thermal analysis [50, 151, 152] by MSC/NASTRAN are presented.

The vibration of a stator in SRMs is known as the main source of the acoustic noise [150]. Using the normal mode analysis (*i.e.,* SOL 103 in MSC/NASTRAN), two dimensional modal analysis of the initial and optimized stator is performed with the following material properties: Young's modulus E=2.07×10^{11} N/m^2, Poisson's ratio

v=0.31, and density ρ=7650 kg/m^3. As for boundary conditions, three bolting points are fixed as described in [150] and all nodes are constrained in the z-direction.

Table 5.4.3 shows the first 6 eigenvalues of the initial and optimized design. The mode shapes of optimized design are shown in Figure 5.4.2. The mode shapes of the initial SRM are the same as that of the optimized SRM. The eigenvalues of the optimized model are nearly the same as those of the initial model; new modes or mode changes do not occur in the optimized design.

In accordance with [50], steady-state thermal analysis (*i.e.,* SOL 153 in MSC/NASTRAN) is carried out for the stator and the coil of SRMs. Thermal conductivity of the stator is set to 445W/mK and that of the coil is set to 489W/mK. The resistivity of the coil is set to 1.72×10^{-8} Ωm. As for heat boundary conditions, the free convection is applied to the outside boundaries of the stator, and the forced convection is applied to all boundaries inside the SRMs. For simplicity, we adopt the following assumptions. The copper loss in the coil is considered the heat source and core loss is neglected. The convection coefficient h_{out} at the outside boundaries of the stator is uniformly given by 8.5W/m^{2}K, and the temperature of outside air is assumed to be 15 ºC. The convection coefficient h_{in} at all inside boundaries is given by 50W/m^2 K, and the temperature of inside air is assumed to be 35ºC. Using these assumptions and the symmetric condition, the 1/12 part of the stator is analyzed.

The heat analysis result is shown in Figure 5.4.3. Since the RMS value of the phase current is unchanged as shown in Table 2, the copper loss in the optimized model (*i.e.,* heat source) is the same as that in the initial model. Although the mass of the optimized stator is slightly increased, the inside surface area is increased by the notched shape at the

pole tips of the optimized stator. Consequently, the overall temperature values are slightly dropped in the optimized model.

Table 5.4.3. Eigenvalues of optimized stator

Initial model		Optimized model	
Number	Eigenvalues (Hz)	Number	Eigenvalues (Hz)
1	112.5	1	111.8
2	169.7	2	168.8
3	169.9	3	168.9
4	312.6	4	311.3
5	312.9	5	311.5
6	489.8	6	489.1

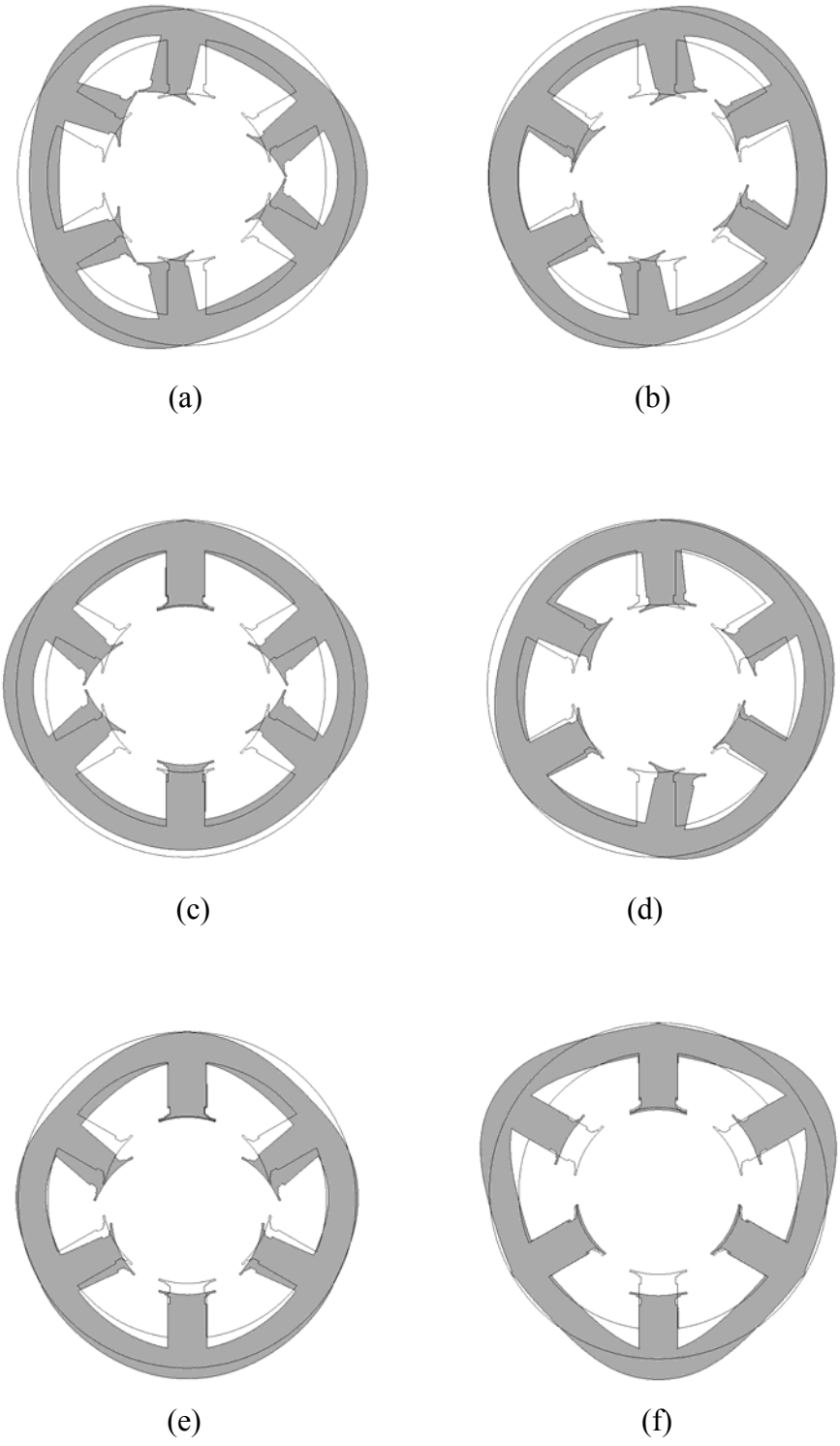

Figure 5.4.2. Mode shapes of optimized stator,
(a) 1st, (b) 2nd, (c) 3rd, (d) 4th, (e) 5th, (f) 6th

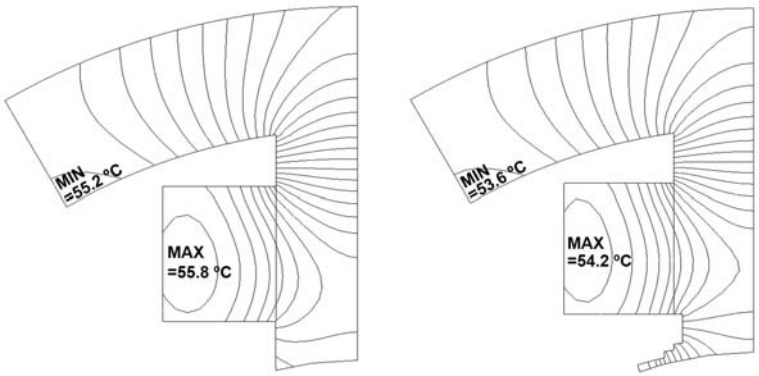

(a) (b)

Figure 5.4.3. Min/max temperature and isotherms of stator,
(a) initial model, (b) optimized model

5.4.3. Three dimensional SRM design result

The proposed approaches are applied to three dimensional design as well. All the analysis and optimization procedure except the finite element analysis, are identical in the two and three dimensional SRM models. In the three dimensional model, not Eq. (5.2.6) but Eq. (5.2.5) is solved using three dimensional nodal or edge finite element method. Figure 5.4.4 shows the design domain in the rotor. The analytical and finite different sensitivities at the one slice of rotor design domain are compared in Figure 5.4.5. As shown in Figure 5.4.5, the analytical sensitivity is in good agreement with the finite-difference sensitivity.

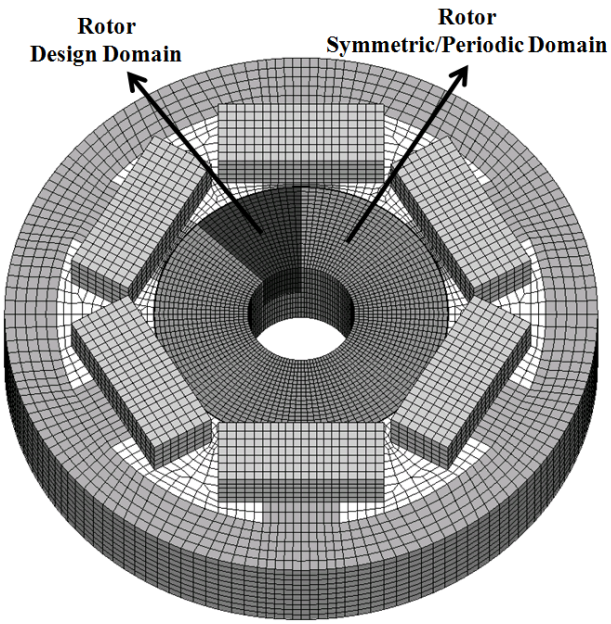

Figure 5.4.4. Design domain of three dimensional SRM

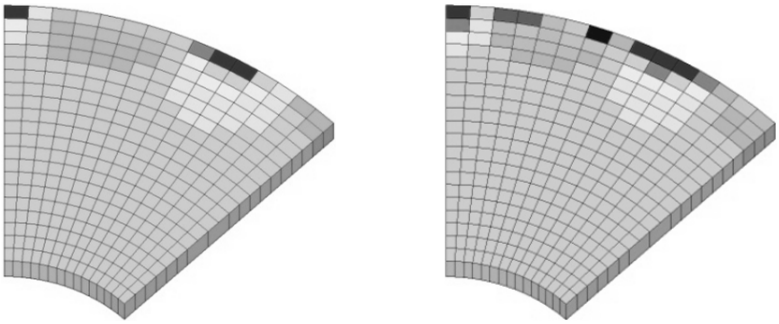

(a)

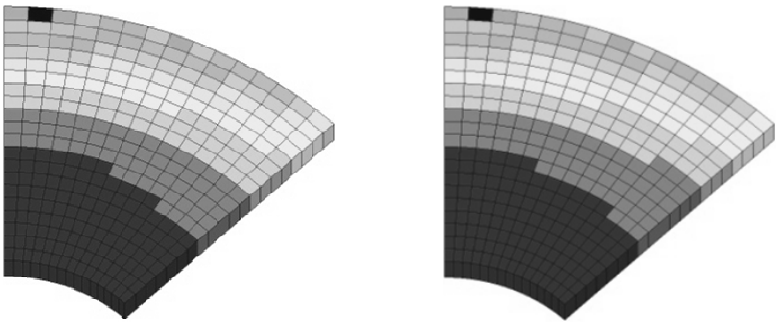

(b)

Figure 5.4.5. Comparison of the analytical sensitivity and finite different sensitivity (a) objective (total torque T_{tot}), (b) constraint (phase current i)

The initial shape and the optimized shape using the nodal or edge element are shown in Figure 5.4.6(a), (b) and (c). The optimized rotor has the holes as well in three dimensional cases. The notched rotor pole shape near the airgap appears in both optimization results using the nodal and edge element.

In Figure 5.4.7(a)-(c) and Figure 5.4.8(a)-(c), the inductance, the phase current and the total torque profile of the initial design (dashed lines) are compared to those of the optimized design using the nodal element or edge element (solid lines). The total torque profile in both results is almost matched with the target torque profile, and the torque ripple is successfully eliminated. The characteristics of the inductance and current curve are not different in two and three dimensional models. It is confirmed that the proposed design approaches can be applied to both two and three dimensional SRM models.

Although it is known that the nodal element has a large error in the magnetic field at the interface of different materials, the performance analysis and optimization result using the nodal element does not show any considerable error. This might be because the performance analysis in SRM starts from the magnetic energy, which is calculated at the Gaussian point over the element. The magnetic field at the Gaussian point might be accurate even when using the nodal element. Therefore, both nodal and edge elements can be used for three dimensional SRM design using the proposed approach.

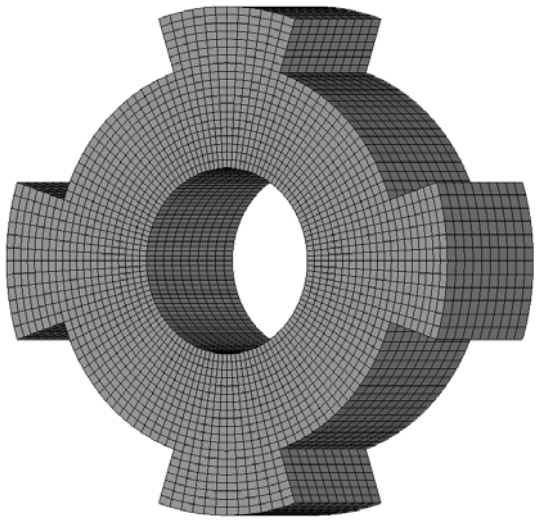

(a)

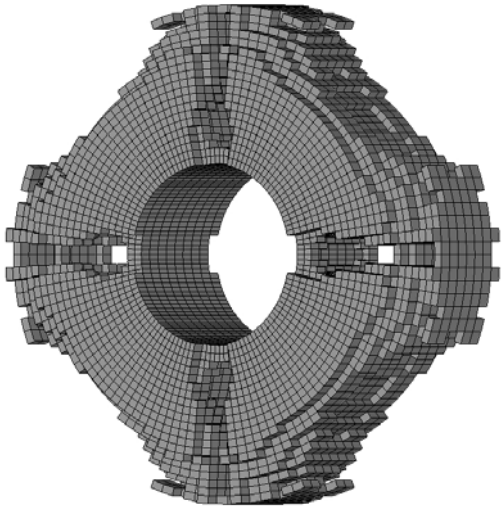

(b)

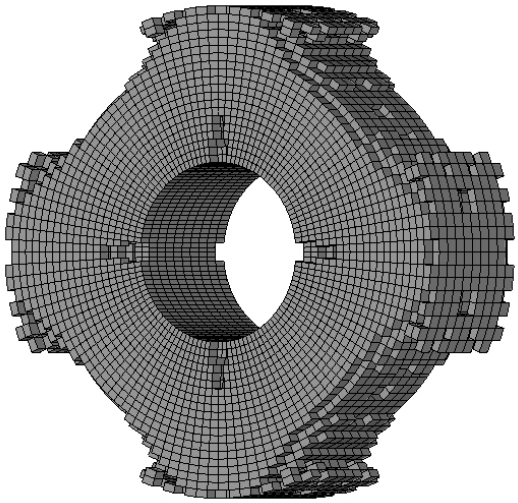

(c)

Figure 5.4.6. Rotor design result

(a) initial shape, (b) optimized shape using nodal element, (c) optimized shape using edge element

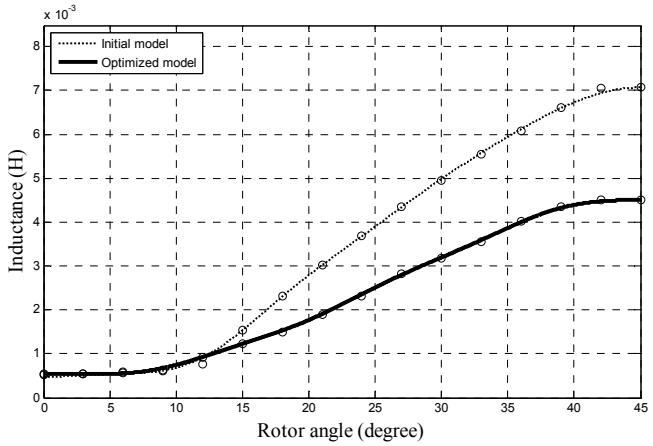

(a)

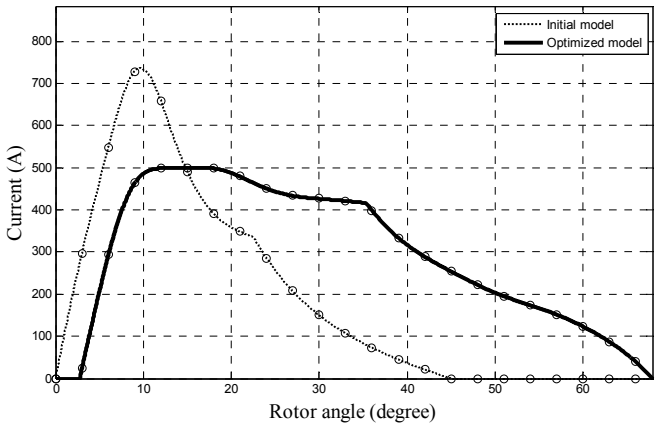

(c)

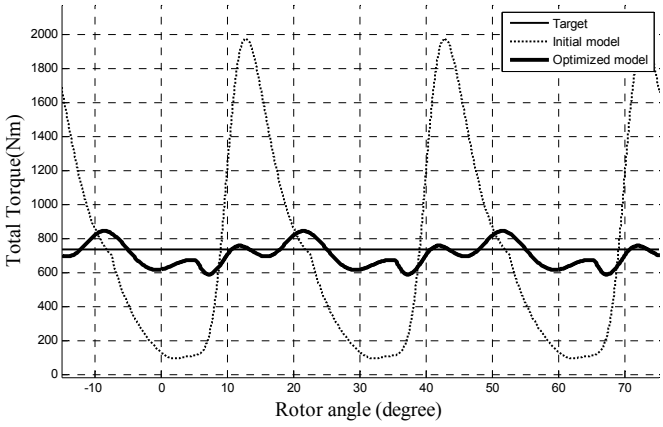

(e)

Figure 5.4.7. Performance analysis result (nodal element)

(a) inductance curve, (b) phase current curve, (c) total torque curve

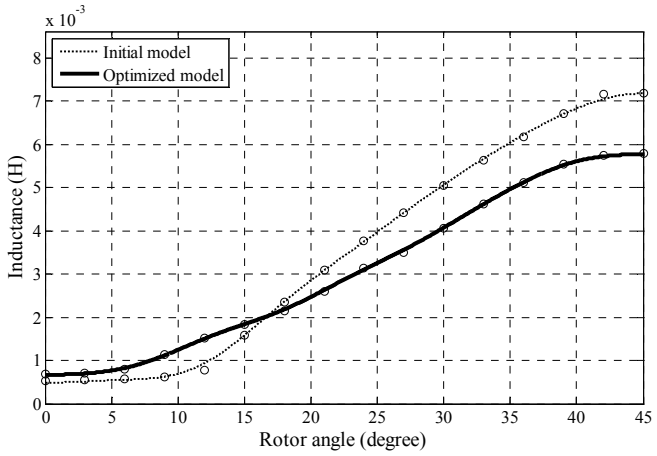

(a)

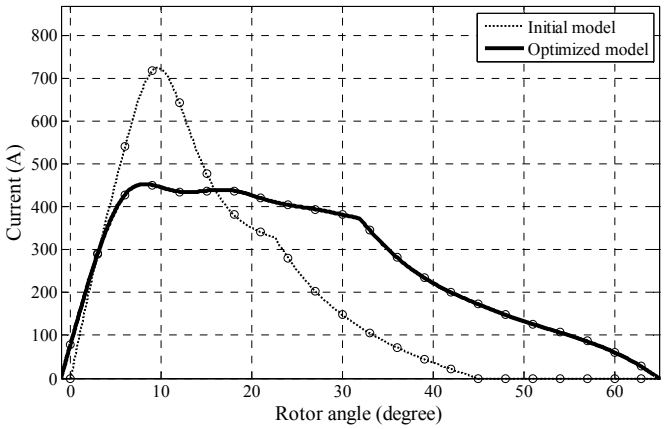

(b)

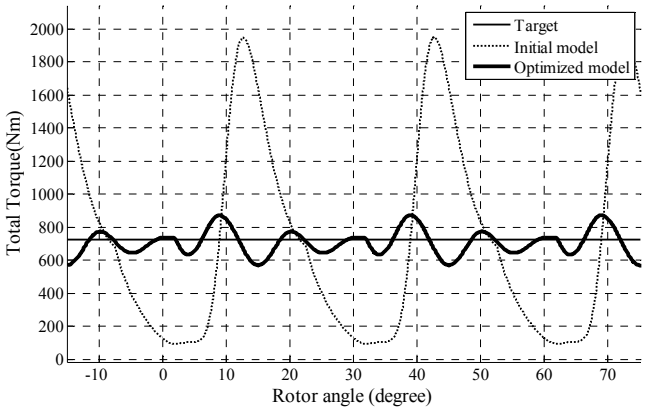

(c)

Figure 5.4.8. Performance analysis result (edge element)

(a) inductance curve, (b) phase current curve, (c) total torque curve

5.5. Conclusion

The design optimization of SRMs is carried out in both the geometric and electric domain: the rotor/stator of SRMs and the voltage on-off angles respectively. The performance analysis of SRMs is given in great detail. Using Fourier series, the analytical sensitivity analysis is derived and verified using the finite-difference sensitivity. As design objectives, the target torque profile is well satisfied and thus torque ripples are minimized with low rotor mass. Copper loss is controlled by constraining the RMS value of the phase current. The geometry of the rotor and the stator are clearly shaped by topology optimization. The proposed multiobjective design problem is successfully solved by the SLP algorithm and the adaptive control of weightings. In addition, the mechanical characteristics of the optimized SRM are discussed using the vibration and thermal analysis by MSC/NASTRAN.

CHAPTER 6
TOPOLOGY OPTIMIZATION OF SWITCHED RELUCTANCE MOTORS IN NON-LINEAR B-H RELATION

6.1. Introduction

Switched reluctance motors (SRMs) are attractive machines for a variety of industrial applications. Their structure is simple and robust, and the motors operate at high efficiency. Moreover, their operation is reliable even at very high speeds. Despite these advantages, however, they also have limitations. They suffer from inherent high torque ripples, which induce noise and vibration problems. Moreover, the highly nonlinear nature of SRMs causes difficulties in their analysis and design.

The main goal in the design of SRMs, therefore, has been to minimize torque ripples. It is well known that torque performance is largely influenced by the geometry of the stator and rotor poles. Therefore, both the size and shape of the poles have been designed to improve torque performance [68, 70, 72]. The effect of rotor and stator pole sizes on torque ripples has been investigated, and optimal sizes have been obtained using the augmented Lagrangian method [68]. The shape of the poles has been designed as well by

optimizing the geometric parameters of initial shapes such as non-uniform stator poles and a rotor pole with a shoe [70], or a rotor pole with a notched tooth [72]. These approaches, however, have the following limitations. First, deciding on the proper parameters requires knowledge of an initial shape, which must be determined by the intuition or experience of a researcher. The wrong decision may not improve the performance of the design result. The second limitation is that the improvement might be restricted because the initial shape is fixed and thus only parameters can vary. If, however, the design method does not require an initial shape, and any shape can be represented as the design result, considerable improvement in SRM performance can be expected. These features are the main advantages of structural topology optimization

To apply structural topology optimization to the design of SRMs, the sensitivity of the SRM performance, such as torque profile and phase current, should be derived analytically. The sensitivity analysis requires the explicit expression of objectives and constraints, which are chosen as functions of the SRM performance. In chapter 5, the explicit expression of SRM performance has been analytically derived using Fourier series expansion of the inductance curve. However, this study ignored the magnetic saturation effect by assuming the linear material property. The magnetic saturation causes the nonlinear characteristic in the magnetization with respect to the current input. Therefore, the inductance curve is not sufficient to describe the magnetization because it does not include the effect of the current input. Instead of the inductance curve, the flux linkage surface, including the effect of the current input, should be obtained to predict SRM performance under magnetic saturation. In order to model the flux linkage surfaces, various performance analysis methods have been proposed using different kinds of

approximation methods [34, 36, 41]. None of these studies, however, derive the explicit expression of SRM performance that is required to apply structural topology optimization.

This chapter proposes a new performance analysis model, which can provide the explicit expressions of torque profile and phase current taking the magnetic saturation effect into account. This model uses Fourier series expansion and piecewise quadratic polynomials to approximate the flux linkage surface. Quadratic polynomials allow us to derive the explicit expression of phase current, which was not available in the previous analysis models [34, 36, 41]. Then, sensitivity analysis of the torque profile and phase current becomes available, and topology optimization can be applied to the design of SRMs.

Based on the proposed performance analysis model, structural topology optimization of SRMs is carried out to find the optimal shape of the rotor and stator minimizing torque ripple. For this design goal, the voltage on-off angles in single-pulse voltage waveform are also optimized. The constraint is applied to the root-mean square (RMS) value of phase current to confine the copper loss. This constraint might ensure the high efficiency of SRMs. As a design example, the two dimensional model of 6/4 SRMs (6 stator poles and 4 rotor poles) is chosen and optimized using the Sequential Linear Programming (SLP) method. In addition, the effects of magnetic saturation on the design result of SRMs are investigated by comparing results with and without magnetic saturation.

The outline of the paper is as follows. Section 6.2 describes the proposed analysis model of SRMs to represent the operating performance of SRMs, and Section 6.3 presents the optimization problem and sensitivity analysis. Next, Section 6.4 gives the optimization results, and Section 6.5 summarizes the paper.

6.2. Non-linear analysis model of SRMs

The motor performance is explicitly represented using the mathematical approximation method. First, the flux linkage λ is approximated based on Fourier series expansions and piecewise quadratic polynomials. Next, the current curve is obtained by solving the voltage equation, and the torque profile is determined using the global virtual work method.

6.2.1. Flux linkage model

The flux linkage model represents the relation between the flux linkage λ, the current of the stator coil i, and the rotor position θ. First, the magnetic energy W_{mag} at discrete currents and rotor positions are calculated by solving the magnetostatic equation using the finite element method with Newton-Raphson iteration. The nonlinear magnetostatic equation can be simply written as

$$\mathbf{K}(\mathbf{A})\mathbf{A} = \mathbf{Q} \tag{6.2.1}$$

where **A** is the magnetic vector potential, **K** is the magnetic stiffness matrix, and **Q** is the load vector. The magnetic reluctivity model proposed in [142], is used to represent the magnetic saturation effect and can be written as

$$\nu\left(B^2\right) = k_1 e^{k_2 B^2} + k_3 \tag{6.2.2}$$

where B is the magnitude of magnetic flux density. After solving Eq. (6.2.1) by using the finite element method with Newton-Raphson iteration, the magnetic energy W_{mag} can be obtained as

$$W_{mag} = \int_{\text{all space}} \left(\int_0^B \mathbf{H} \cdot d\mathbf{B} \right) dv = \int_{\text{all space}} \left(\int_0^B \nu \left(B^2 \right) B \, dB \right) dv \tag{6.2.3}$$

where **H** is magnetic field intensity and **B** is magnetic flux density. This process is performed at many different phase current values and rotor positions, and magnetic energy $(W_{mag})_{jk}$ at discrete the jth phase currents and the kth rotor position is calculated.

The next step is to find the flux linkage curves with respect to the phase current i axis at fixed rotor position θ. From the approximation using piecewise quadratic polynomials, the flux linkage λ_{km} at fixed kth rotor position and mth piecewise interval is written as

$$\lambda_{km}(i) = C_{1km} i^2 + C_{2km} i + C_{3km} \tag{6.2.4}$$

where i is the phase current of the stator coil. The reason why the piecewise quadratic polynomials are chosen is as follows. First, any piecewise function may represent both the line and curve well. The second order polynomial gives the analytical solution of the voltage equation. Finally, the derivative of the flux linkage λ is not required for the performance analysis. Therefore, the C^1 continuity that can be considered in the cubic polynomials does not need to be satisfied. Figure 6.2.1 shows the flux linkage curve with respect to the phase current at a fixed rotor angle. To find the three coefficients C_{1km},

C_{2km}, and C_{3km}, three conditions are required at every mth interval. Two conditions are obtained from the relation between the magnetic energy $(W_{mag})_{jk}$ and flux linkage λ_{km}, which can be represented as

$$\left(W_{mag}\right)_{jk} = i_j \cdot \lambda_{km}\left(i_j\right) - \int_0^{i_j} \lambda_{km}\left(i\right) di \tag{6.2.5}$$

In the above equation, the discrete current position j is set as $2m$-1, and $2m$. The last condition is the continuous condition at the current position j=$2m$+1. From these three conditions, the system of equations to find the coefficients is derived as

$$\begin{pmatrix} \frac{2}{3}i_{2m}{}^3 + \frac{1}{3}i_{2m-1}{}^3 & \frac{1}{2}i_{2m}{}^2 + \frac{1}{2}i_{2m-1}{}^2 & i_{2m-1} \\ \frac{2}{3}i_{2m+1}{}^3 + \frac{1}{3}i_{2m-1}{}^3 & \frac{1}{2}i_{2m+1}{}^2 + \frac{1}{2}i_{2m-1}{}^2 & i_{2m-1} \\ i_{2m-1}{}^2 & i_{2m-1} & 1 \end{pmatrix} \begin{pmatrix} C_{1jm} \\ C_{2jm} \\ C_{3jm} \end{pmatrix}$$

$$= \begin{pmatrix} \left(W_{mag}\right)_{j(2m)} + \sum_{k=1}^{m-1}\left(\frac{1}{3}C_{1jk}\left(i_{2k+1}{}^3 - i_{2k-1}{}^3\right) + \frac{1}{2}C_{2jk}\left(i_{2k+1}{}^2 - i_{2k-1}{}^2\right) + C_{2jk}\left(i_{2k+1} - i_{2k+1}\right)\right) \\ \left(W_{mag}\right)_{j(2m-1)} + \sum_{k=1}^{m-1}\left(\frac{1}{3}C_{1jk}\left(i_{2k+1}{}^3 - i_{2k-1}{}^3\right) + \frac{1}{2}C_{2jk}\left(i_{2k+1}{}^2 - i_{2k-1}{}^2\right) + C_{2jk}\left(i_{2k+1} - i_{2k+1}\right)\right) \\ C_{1j(m-1)}i_{2m-1}{}^2 + C_{2jm}i_{2m-1} + C_{3jm} \end{pmatrix} \tag{6.2.6}$$

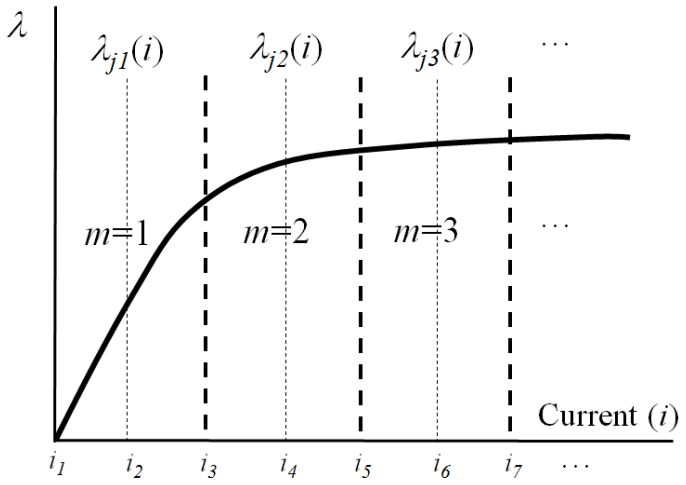

Figure 6.2.1. Flux linkage curve with respect to the phase current

Next, the Fourier series expansion is applied to Eq. (6.2.4) for the approximation with respect to the rotor position θ axis. Then the model representing flux linkage λ with respect to phase current i and rotor angle θ is represented as

$$\Phi_m(i,\theta) = \left(F_{1m,0}i^2 + F_{2m,0}i + F_{3m,0}\right) + \sum_{n=1}^{NF}\left(F_{1m,n}i^2 + F_{2m,n}i + F_{3m,n}\right)\cos(n\,\mathrm{P_r}\,\theta) \tag{6.2.7}$$

where NF is the number of Fourier series expansions, $\mathrm{P_r}$ is the number of rotor poles, and $F_{qm,n}$ are the coefficients of Fourier series expansions, which can be written as

$$F_{qm,0} = \frac{1}{2\pi / \mathrm{P_r}}\sum_{j=1}^{m}\left(\left(C_{q(j+1)m} + C_{q(j)m}\right)\left(\theta_{j+1} - \theta_j\right)\right) \tag{6.2.8}$$

$$F_{qm,n} = \frac{2}{n\pi}\sum_{j=1}^{m}\left[\left(C_{q(j+1)m}\right)\cdot\left(\sin\left(n\,\mathrm{P_r}\,\theta_{j+1}\right)+\frac{\cos\left(n\,\mathrm{P_r}\,\theta_{j+1}\right)-\cos\left(n\,\mathrm{P_r}\,\theta_{j}\right)}{n\,\mathrm{P_r}\left(\theta_{j+1}-\theta_{j}\right)}\right)\right.$$
$$\left.-\left(C_{q(j)m}\right)\cdot\left(\sin\left(n\,\mathrm{P_r}\,\theta_{j}\right)+\frac{\cos\left(n\,\mathrm{P_r}\,\theta_{j+1}\right)-\cos\left(n\,\mathrm{P_r}\,\theta_{j}\right)}{n\,\mathrm{P_r}\left(\theta_{j+1}-\theta_{j}\right)}\right)\right] \tag{6.2.9}$$

Figure 6.2.2 shows the attained flux linkage model. The filled circular marks represent the flux linkage at discrete current and rotor angle positions where the finite element analysis is carried out. As shown in Figure 6.2.2, the flux linkage is smoothly approximated using the proposed method for the analytical representation.

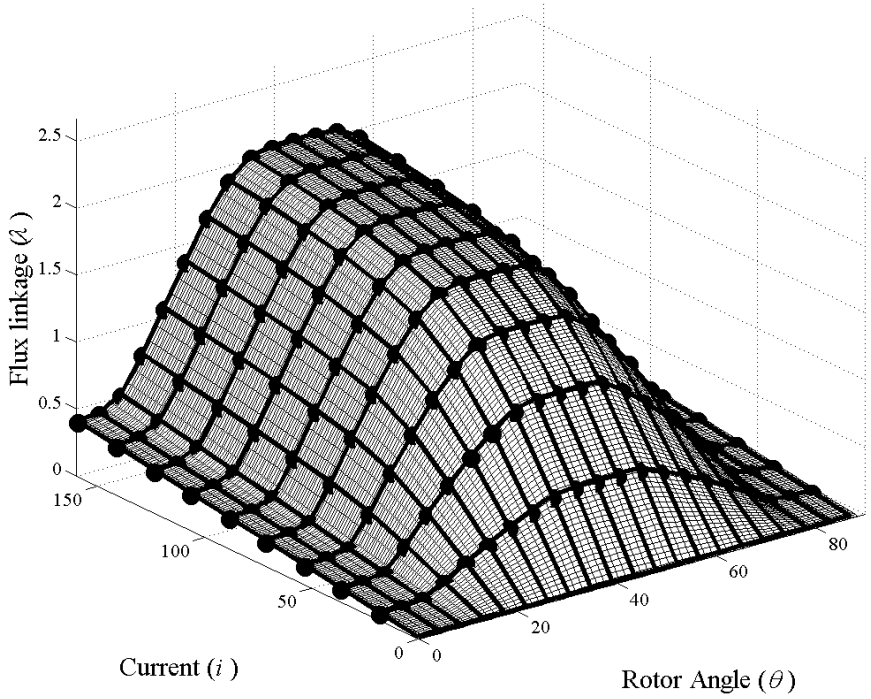

Figure 6.2.2. Flux linkage model

6.2.2. Phase current curve

After calculating the flux linkage, the current curve is obtained by solving the voltage equation. The voltage equation of SRMs is given by

$$V = Ri + \frac{d\left(\Phi\left(i,\theta\right)\right)}{dt} \tag{6.2.10}$$

where V is the source voltage, and R is the stator coil resistance. In order to solve the voltage equation analytically, the voltage drop due to the stator coil resistance is neglected. Thus, Eq. (6.2.10) yields

$$V = \frac{d\left(\Phi\left(i,\theta\right)\right)}{dt} \tag{6.2.11}$$

We assume steady-state rotation and zero phase current at the voltage-on angle. The voltage waveform used in this work is shown in Figure 6.2.3. By solving Eq. (6.2.11) with the assumptions, the explicit expression of phase current curve is obtained as

$$i\left(\theta\right) = \frac{-X_2 \pm \sqrt{{X_2}^2 - 4X_1\left(X_3 - \Phi_0 - \frac{V_0}{\omega}\left(\theta - \theta_0\right)\right)}}{2X_1} \tag{6.2.12}$$

where

$$X_i = \sum_{n=0}^{NF} F_{im,n} \cos\left(n \mathrm{P_r}\, \theta\right) \tag{6.2.13}$$

, θ_0 is the voltage-on angle, Φ_0 is the flux linkage at θ_0, and ω is the constant angular velocity. Figure 6.2.4 shows the phase current profiles of typical 6/4 SRMs with nonlinearly saturated material and linear material assumption. In this example, typical rotor and stator shapes are used, and the voltage on-off angles are set to 0° and 50° respectively. As shown in Figure 2, phase current with saturated material (solid line) is higher than that with the linear material assumption (dashed line).

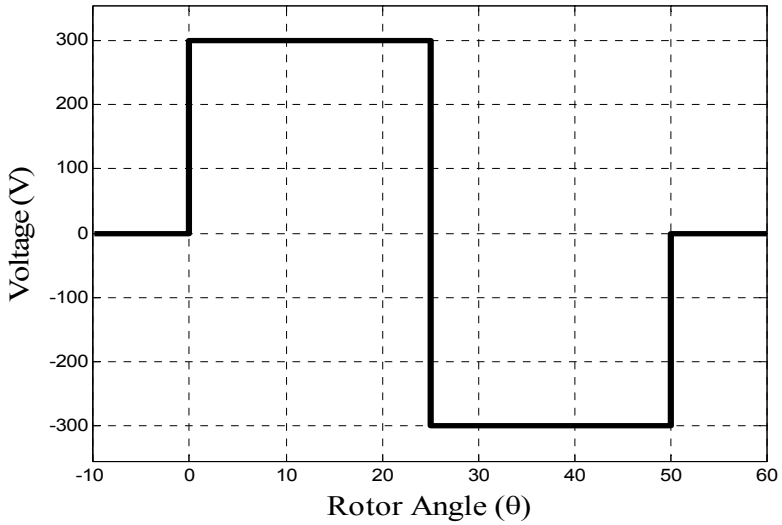

Figure 6.2.3. Single pulse voltage waveform

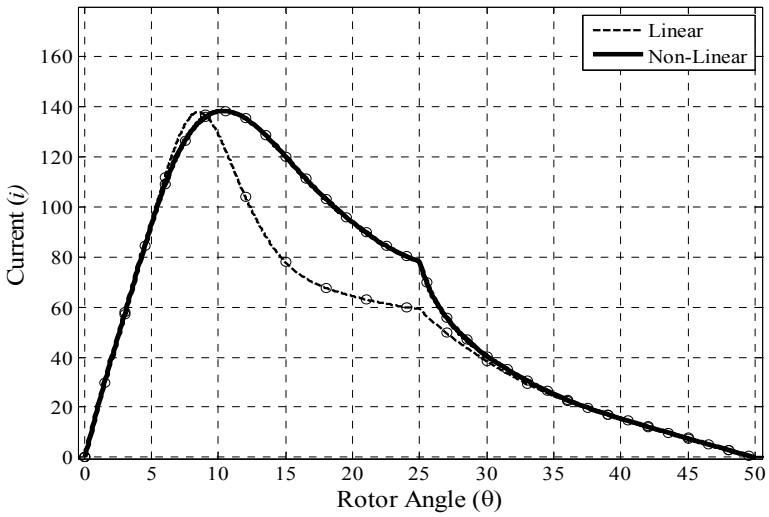

Figure 6.2.4. Current curve in both linear and non-linear **B-H** relation

6.2.3. Torque Curve

The torque profile of SRMs is calculated using the global virtual work method [138]. The global virtual work method is based on the principle of conservation of energy and virtual displacement. This method uses the coenergy at a set of closely spaced rotor positions. The coenergy W_{co} is defined as

$$W_{\mathrm{co}} = \int_0^i \lambda \, d\tilde{i} \Big|_{\theta=\text{constant}} \tag{6.2.14}$$

By taking the derivative of the total coenergy with respect to the rotor angle θ, the torque profile is obtained as

$$T(i,\theta) = \frac{\partial W_{\mathrm{co}}}{\partial \theta}\Big|_{i=\text{constant}} \tag{6.2.15}$$

Substituting Eq. (6.2.7) and Eq. (6.2.14) into Eq. (6.2.15), the torque profile is explicitly given by

$$\begin{aligned}\mathbf{T}\left(\theta, i(\theta)\right) = &-\sum_{n=0}^{NF}\left(\frac{1}{3}F_{1m,n}\left(i^3 - {i_{2m-1}}^3\right) + \frac{1}{2}F_{2m,n}\left(i^2 - {i_{2m-1}}^2\right) + F_{3m,n}\left(i - i_{2m-1}\right)\right) n\,\mathrm{P_r}\sin(n\,\mathrm{P_r}\,\theta) \\ &-\sum_{k=1}^{m-1}\sum_{n=0}^{NF}\left(\frac{1}{3}F_{1k,n}\left({i_{2k+1}}^3 - {i_{2k-1}}^3\right) + \frac{1}{2}F_{2k,n}\left({i_{2k+1}}^2 - {i_{2k-1}}^2\right) + F_{3k,n}\left(i_{2k+1} - i_{2k-1}\right)\right) n\,\mathrm{P_r}\sin(n\,\mathrm{P_r}\,\theta)\end{aligned} \tag{6.2.16}$$

It is noted that the function of the current i is obtained from Eq. (6.2.12). Figure 6.2.5 shows the torque profile of the typical SRM model. As expected, the torque with the

saturated material property (solid line) is much higher than that with the linear material assumption (dashed line). This higher torque reveals the reason why SRMs usually operate under the saturated condition.

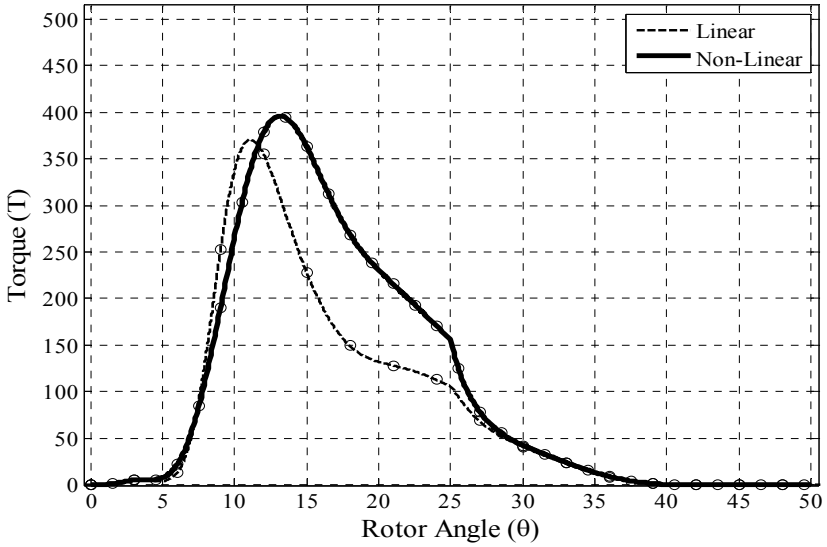

Figure 6.2.5. Torque profile in both linear and non-linear **B-H** relation

6.3. Design optimization

The structural topology optimization method finds the optimal arrangement of a structure by setting material densities as design variables. The material densities are relaxed as a continuous variable to use a mathematical programming method such as SLP. The material becomes air when the density is zero, and it becomes steel when the density is one. The material properties of the intermediate densities are interpolated using the density method proposed in [10]

6.3.1. Optimization problem formulation

The design strategy and design domains are identical to those of the previous study with the linear material assumption. The geometric design domains are both the rotor and stator. The electric design domain, such as voltage turn-on and off angles, is added to the optimization. The optimization problem, which is also identical to that of the previous study, is formulated as

$$\text{Minimize } f = \left[\sum_{j=1}^{\text{n}} \left(\frac{T_k}{T^*} - 1.0 \right)^2 + \alpha \cdot f_c(\boldsymbol{\rho}) + \beta \cdot V(\boldsymbol{\rho}) \right] \tag{6.3.1}$$

$$\text{subject to} \quad 0 < \rho_{\min} \le \rho_u \le \rho_{\max} \qquad (k = 1, .., ND) \tag{6.3.2}$$

$$i_{rms} \le i_{rms}^* \tag{6.3.3}$$

$$f_c(\boldsymbol{\rho}) = \sum_{u=1}^{ND} \frac{\rho_u (1 - \rho_u)}{ND} \tag{6.3.4}$$

$$V(\boldsymbol{\rho}) = \sum_{\text{u}} \rho_u a_u \Big/ \sum_{\text{u}} a_u \tag{6.3.5}$$

where T_k is the torque value at kth rotor angle θ_k (j=1,…,n), n is the number of discrete rotor angles, T^* is the target average torque, i_{rms} is the RMS value of phase current, a_u is the area of uth element, α and β are the weighting values for the density convergence function $f_c(\boldsymbol{\rho})$ and the normalized rotor mass function $V(\boldsymbol{\rho})$ respectively, and ND is the number of design variables.

To minimize the torque ripple, the torque values T_k at given rotor angles θ_k is handled to become the constant target average torque T^*. The density convergence function $f_c(\boldsymbol{\rho})$ is added to the objective function for enforcing the convergence of intermediate densities, and the normalized rotor mass function $V(\boldsymbol{\rho})$ is also added to minimize the mass of the rotor.

The constraint is applied to the RMS value of phase current i_{rms}, which is given by

$$i_{rms} = \sqrt{\frac{1}{T_e}\int_0^{T_e} i^2 dt} \approx \sqrt{\frac{1}{n}\sum_{k=1}^{n} {i_k}^2} \tag{6.3.6}$$

This constraint confines the copper loss, which is one of main heat sources and can be written as

$$W_{copper} = R \cdot {i_{rms}}^2 \tag{6.3.7}$$

The formulated optimization problem is solved using the SLP method, which is one of the mathematical programming methods that require the sensitivity of objective and constraint functions. The proposed performance analysis model gives the analytical representation of the current curve and torque profile. Therefore, the analytical sensitivity of objective and constraint functions is available.

6.3.2. Sensitivity analysis

The analytical sensitivity of objective (*i.e.*, Eq.(6.3.1)) and constraint (*i.e.*, Eq. (6.3.3)) functions is derived using the direct differentiation and chain rule. The derivative of objective function with respect to density design variables ρ_u is given as

$$\frac{df}{d\rho_u} = \sum_{j=1}^{\mathrm{n}} 2\left(\frac{T_k}{T*} - 1.0\right)\frac{\partial T_k}{\partial \rho_u} + \alpha \frac{1-2\rho_u}{ND} + \beta \cdot a_u \tag{6.3.8}$$

From Eq. (6.2.16), the derivative of torque $\partial T_k / \partial \rho_u$ can be obtained as

$$\begin{aligned}
&\frac{\partial T_k(\theta, i)}{\partial \rho_u} \\
&= -\sum_{n=0}^{NF}\left(\frac{1}{3}\frac{\partial F_{1m,n}}{\partial \rho_u}\left(i_o^{\,3} - i_{2m-1}^{\,3}\right) + \frac{1}{2}\frac{\partial F_{2m,n}}{\partial \rho_u}\left(i_o^{\,2} - i_{2m-1}^{\,2}\right) + \frac{\partial F_{3m,n}}{\partial \rho_u}\left(i_o - i_{2m-1}\right)\right) n\,\mathrm{P_r}\sin(n\,\mathrm{P_r}\,\theta_k) \\
&-\sum_{p=1}^{m-1}\sum_{n=0}^{NF}\left(\frac{1}{3}\frac{\partial F_{1p,n}}{\partial \rho_u}\left(i_{2p+1}^{\,3} - i_{2p-1}^{\,3}\right) + \frac{1}{2}\frac{\partial F_{2p,n}}{\partial \rho_u}\left(i_{2p+1}^{\,2} - i_{2p-1}^{\,2}\right) + \frac{\partial F_{3p,n}}{\partial \rho_u}\left(i_{2p+1} - i_{2p-1}\right)\right) n\,\mathrm{P_r}\sin(n\,\mathrm{P_r}\,\theta_k) \\
&-\sum_{n=0}^{NF}\left(\frac{1}{3}F_{1m,n}\left(3i^{\,2}\frac{\partial i}{\partial \rho_u} - i_{2m-1}^{\,3}\right) + \frac{1}{2}F_{2m,n}\left(2i\,\frac{\partial i}{\partial \rho_u} - i_{2m-1}^{\,2}\right) + F_{3m,n}\left(\frac{\partial i}{\partial \rho_u} - i_{2m-1}\right)\right) n\,\mathrm{P_r}\sin(n\,\mathrm{P_r}\,\theta_k)
\end{aligned} \tag{6.3.9}$$

All terms in (6.3.9) are explicitly calculated except $\partial F_{qm,n} / \partial \rho_u$ and $\partial i / \partial \rho_u$. From Eq. (6.2.12), the derivative of the current $\partial i / \partial \rho_u$ is derived as

$$\frac{\partial i}{\partial \rho} = -\frac{1}{2X_1}\frac{\partial X_2}{\partial \rho} - \frac{1}{2}\frac{\left(2X_2\frac{\partial X_2}{\partial \rho} - 4\frac{\partial X_1}{\partial \rho}\left(X_3 - \Phi_o - \frac{V_0}{\omega}(\theta - \theta_o)\right) - 4X_1\left(\frac{\partial X_3}{\partial \rho} - \frac{\Phi_o}{\partial \rho}\right)\right)}{2X_1\left({X_2}^2 - 4X_1\left(X_3 - \Phi_o - \frac{V_0}{\omega}(\theta - \theta_o)\right)\right)^{\frac{1}{2}}}$$
$$-\frac{-X_2 \pm \sqrt{{X_2}^2 - 4X_1\left(X_3 - \Phi_o - \frac{V_0}{\omega}(\theta - \theta_o)\right)}}{2{X_1}^2}\frac{\partial X_1}{\partial \rho} \tag{6.3.10}$$

where

$$\frac{\partial X_i}{\partial \rho} = \left(\sum_{n=0}^{NF}\frac{\partial F_{im(p),n}}{\partial \rho}\cos(n\,\mathrm{P_r}\,\theta)\right) \tag{6.3.11}$$

From Eq. (6.2.8) and (6.2.9), the derivative of Fourier series expansion coefficients $\partial F_{qm,n}/\partial \rho_u$ can be written as

$$\frac{\partial F_{qm,0}}{\partial \rho} = \frac{1}{2\pi / \mathrm{P_r}}\sum_{j=1}^{m}\left(\left(\frac{\partial C_{q(j+1)m}}{\partial \rho} + \frac{\partial C_{q(j)m}}{\partial \rho}\right)\left(\theta_{j+1} - \theta_j\right)\right) \tag{6.3.12}$$

$$\frac{\partial F_{qm,n}}{\partial \rho} = \frac{2}{n\pi}\sum_{j=1}^{m}\left[\left(\frac{\partial C_{q(j+1)m}}{\partial \rho}\right)\cdot\left(\sin\left(n\,\mathrm{P_r}\,\theta_{j+1}\right) + \frac{\cos\left(n\,\mathrm{P_r}\,\theta_{j+1}\right) - \cos\left(n\,\mathrm{P_r}\,\theta_j\right)}{n\,\mathrm{P_r}\left(\theta_{j+1} - \theta_j\right)}\right)\right.$$
$$\left. -\left(\frac{\partial C_{q(j)m}}{\partial \rho}\right)\cdot\left(\sin\left(n\,\mathrm{P_r}\,\theta_j\right) + \frac{\cos\left(n\,\mathrm{P_r}\,\theta_{j+1}\right) - \cos\left(n\,\mathrm{P_r}\,\theta_j\right)}{n\,\mathrm{P_r}\left(\theta_{j+1} - \theta_j\right)}\right)\right] \tag{6.3.13}$$

The above derivative requires the derivative of the piecewise quadratic polynomial coefficients C_{rjm}. From Eq. (6.2.6), the derivative $\partial C_{rjm}/\partial \rho_u$ is given by

$$\begin{pmatrix} \frac{\partial C_{1jm}}{\partial \rho} \\ \frac{\partial C_{2jm}}{\partial \rho} \\ \frac{\partial C_{3jm}}{\partial \rho} \end{pmatrix} = \mathbf{A}^{-1} \begin{pmatrix} \frac{\partial \left(W_{mag}\right)_{j(2m)}}{\partial \rho} - \sum_{l=1}^{m-1} \left(\frac{1}{3} \frac{\partial C_{1jl}}{\partial \rho} \left({i_{2k+1}}^3 - {i_{2k-1}}^3 \right) + \frac{1}{2} \frac{\partial C_{2jl}}{\partial \rho} \left({i_{2k+1}}^2 - {i_{2k-1}}^2 \right) + \frac{\partial C_{2jl}}{\partial \rho} \left(i_{2k+1} - i_{2k+1} \right) \right) \\ \frac{\partial \left(W_{mag}\right)_{j(2m-1)}}{\partial \rho} - \sum_{l=1}^{m-1} \left(\frac{1}{3} \frac{\partial C_{1jl}}{\partial \rho} \left({i_{2k+1}}^3 - {i_{2k-1}}^3 \right) + \frac{1}{2} \frac{\partial C_{2jl}}{\partial \rho} \left({i_{2k+1}}^2 - {i_{2k-1}}^2 \right) + \frac{\partial C_{2jl}}{\partial \rho} \left(i_{2k+1} - i_{2k+1} \right) \right) \\ \frac{\partial C_{1j(m-1)}}{\partial \rho} {i_{2m-1}}^2 + \frac{\partial C_{2jm}}{\partial \rho} i_{2m-1} + \frac{\partial C_{3jm}}{\partial \rho} \end{pmatrix} \tag{6.3.14}$$

where

$$\mathbf{A} = \begin{pmatrix} \frac{2}{3} {i_{2m}}^3 - \frac{1}{3} {i_{2m-1}}^3 & \frac{1}{2} {i_{2m}}^2 - \frac{1}{2} {i_{2m-1}}^2 & -i_{2m-1} \\ \frac{2}{3} {i_{2m+1}}^3 - \frac{1}{3} {i_{2m-1}}^3 & \frac{1}{2} {i_{2m+1}}^2 - \frac{1}{2} {i_{2m-1}}^2 & -i_{2m-1} \\ {i_{2m-1}}^2 & i_{2m-1} & 1 \end{pmatrix} \tag{6.3.15}$$

The derivative of magnetic energy $\partial(W_{mag})/\partial\rho_u$ can be obtained using the adjoint method. From Eq. (6.2.1)-(6.2.3), it can be written as

$$\frac{d\left(W_{mag}\right)}{d\rho_u} = \int_e \int_0^{B_{jk}} \left(\left(k_1 e^{k_2 \vec{B}^2} + k_3 \right) \mathrm{p} {\rho_u}^{\mathrm{p-1}} + \nu_{air} \left(-\mathrm{p} {\rho_u}^{\mathrm{p-1}} \right) \right) \vec{B} \, d\vec{B} \, dV - \boldsymbol{\lambda}^T \frac{\partial \mathbf{K}(\mathbf{A})}{\partial \rho_u} \mathbf{A} \tag{6.3.16}$$

The adjoint variable λ is the solution of the adjoint equation:

$$\left(\mathbf{K}(\mathbf{A}) + \frac{\partial \mathbf{K}(\mathbf{A})}{\partial \mathbf{A}} \mathbf{A} \right) \boldsymbol{\lambda} = \mathbf{Q} \tag{6.3.17}$$

It is noted that **K** and **A** should be the final converged quantities. Therefore, the sensitivity analysis is carried out after the Newton-Raphson iteration is finished. Finally, the analytical sensitivity of the objective function can be calculated using Eq. (6.3.8)-(6.3.17).

Next, the derivative of the constraint function (*i.e.* the RMS value of phase current) is derived as

$$\frac{\partial i_{rms}}{\partial \rho_u} \cong \left(\frac{1}{n} \sum_{k=1}^{n} i_k \cdot \frac{\partial i_k}{\partial \rho_u} \right) / \sqrt{\frac{1}{n} \sum_{k=1}^{n} {i_k}^2} \tag{6.3.18}$$

The above derivative requires the derivative of the current $\partial i / \partial \rho_u$, which is already derived in Eq. (6.3.10).

The derived analytical sensitivity of the objective and constraints functions is verified by comparing with the finite-difference sensitivity. Figure 6.3.1 shows the analytical and finite-difference sensitivity of the rotor design domain for (a) the derivative of torque objective and (b) the derivative of current. As shown in Figure 6.3.1, the analytical sensitivity is in good agreement with the finite-difference sensitivity.

Analytical sensitivity **Finite-difference sensitivity**

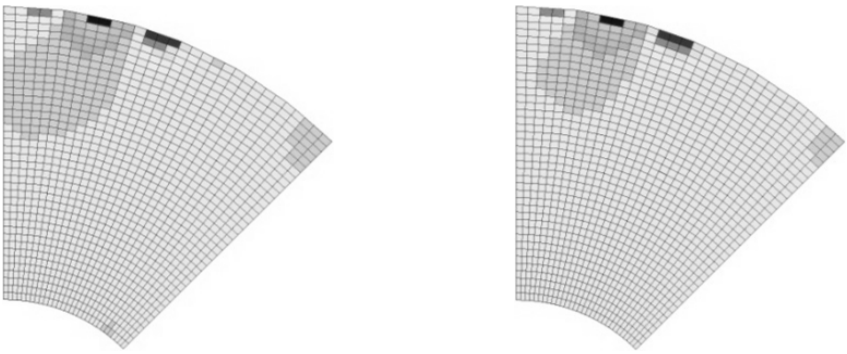

(i) Rotor design domain

(ii) Stator design domain

(a)

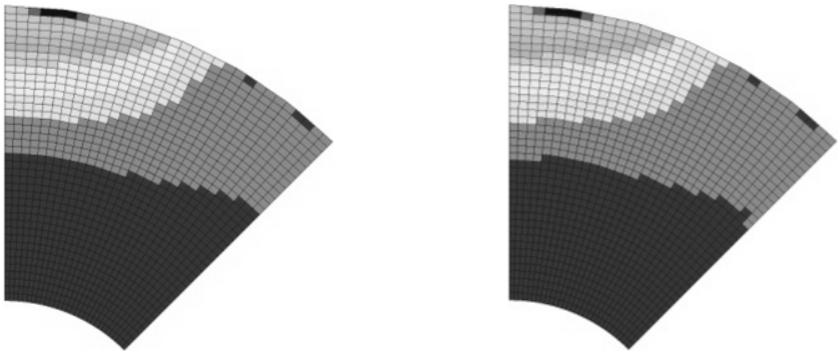

(i) Rotor design domain

(ii) Stator design domain

(b)

Figure 6.3.1. Comparison of the analytical and finite-difference sensitivity (a) Derivative of torque $\partial T_k / \partial \rho_u$, (b) derivative of current $\partial i / \partial \rho_u$

6.4. Design result and discussion

Two dimensional 6/4 SRM (6 stator poles and 4 rotor poles) is designed using the proposed method. The basic specification of SRM is the same as that of previous chapter for the linear problem. The target average torque T^* is set as the average torque of the typical design, which is shown in Figure 6.4.2(a). The constraint value i_{rms}^* on the RMS value of phase current is also set as the RMS current of typical designs. The initial densities are uniformly given as 0.65. The voltage on-off angles are set as 5° and 50° respectively. The move limits of the SLP method are 0.005 for density design variables and 0.0005 for angle design variables.

The gray-scale structures of SRM during the optimization iterations are presented in Figure 6.4.1. The black color in the design domain represents steel, and the white color represents air. This figure shows that the structural topology optimization method gives the optimal shape of the structure without any pre-fixed structural layout.

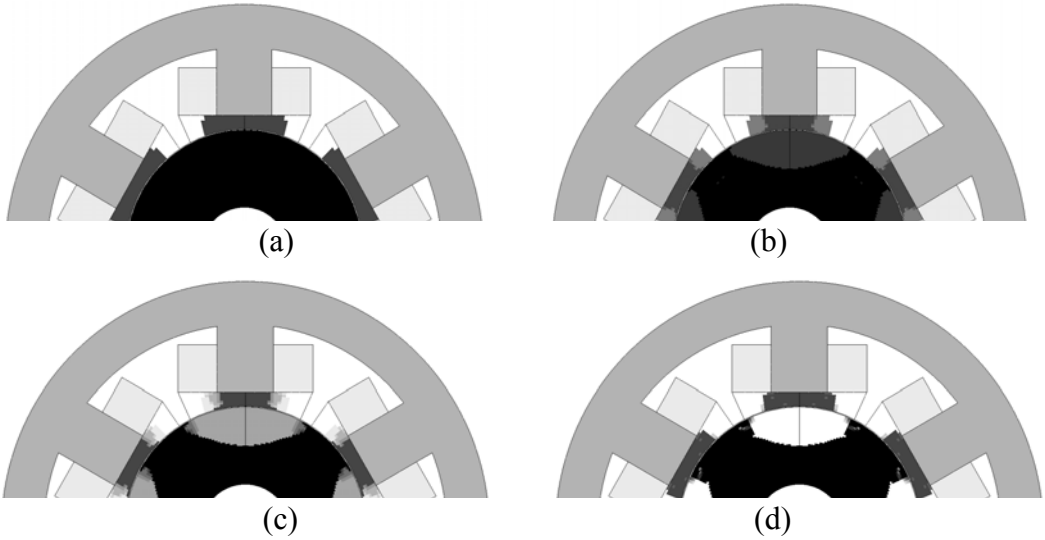

Figure 6.4.1. Shape of SRM during the optimization iteration
(a) 0 iterations, (b) 50 iterations, (c) 120 iterations, (d) 300 iterations

The optimized shape with linear material assumption is shown in Figure 6.4.2(b). In this result, holes are created inside the rotor to reduce the mass of rotor. Figure 6.4.2(c) shows the optimized shape when the magnetic saturation effect is considered. Here, holes are not created although mass minimization is added in the objective functions. The reason for this difference might be the different characteristics of magnetic flux when the flowing path becomes narrow (*i.e.*, when holes are created). In linear material, the magnetic flux density increase inverses proportionally to the area of the flowing path, and consequently an identical amount of magnetic flux can flow even in the narrowed path. In saturated material, the flow of magnetic flux is interrupted when the area of the flowing path is narrowed. Higher phase current input is required to produce the same amount of flux density as that flowing in a wide path. This characteristic in saturated material prevents the creation of holes in the designed shape. The results for both linear and non-linear problems are designed to have a notched rotor pole shape near the airgap. The notched shape has been already used as the fixed shape of the linear SRM optimization problem to minimize torque ripple [70, 72]. Without the linear material assumption and pre-fixed shape, the notched rotor pole shape is obtained as the optimization result. This confirms that the notched rotor pole is the optimal shape to minimize torque ripple for both linear and non-linear problems.

Table 6.4.1 shows the design parameters of the typical and optimized SRM, and also compares the average torques and the RMS values of phase current. As shown in Table 6.4.1, the arc lengths of both the rotor and the stator poles are increased in order to minimize torque ripples. As electronic design variables, the voltage-on angle falls while the voltage-off angle rises; the range of the voltage on-off angles is widened. Average

torque of the designed motor successfully satisfies the target average torque (6% lower than target average torque). The RMS value of phase current in the designed motor is well constrained.

In Figure 6.4.3, phase current and the torque profile of the optimized design (solid lines) are compared to those of the typical design (dashed lines). As shown in Figure 6.4.3(a), the operating ranges of phase current increase with the widened voltage waveform. The narrow current profile in the typical model gets spread in the optimized model while satisfying the current constraint. The maximum value of phase current is notably decreased after optimization. As shown in Figure 6.4.3(b), the total torque profile of the optimized design is nearly matched with the target torque, and the torque ripple is remarkably reduced.

Table 6.4.1. Design parameters and performance analysis result

Typical design		Optimized design	
Stator pole arc(degree)	27	Stator pole arc(degree)	39
Rotor pole arc(degree)	42	Rotor pole arc(degree)	45
Voltage-on angle θ_{on} (degree)	0	Voltage-on angle θ_{on} (degree)	-4.43
Voltage-off angle θ_{off} (degree)	50	Voltage-off angle θ_{off} (degree)	63.50
Average torque (Nm)	184.7	Average torque (Nm)	172.9
RMS value of current (A)	57.2	RMS value of current (A)	56.4

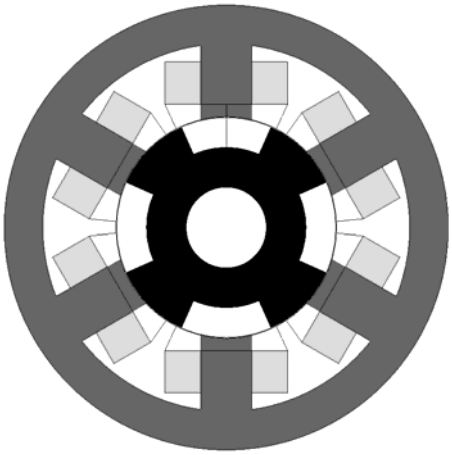

(a)

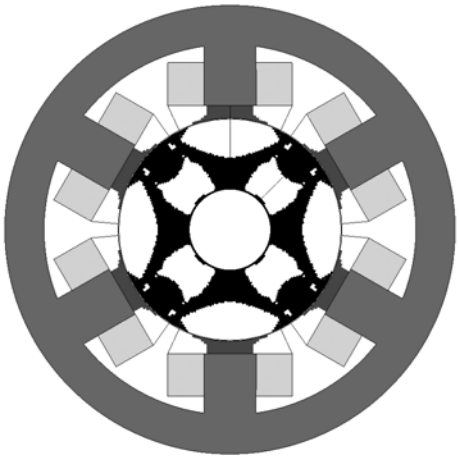

(b)

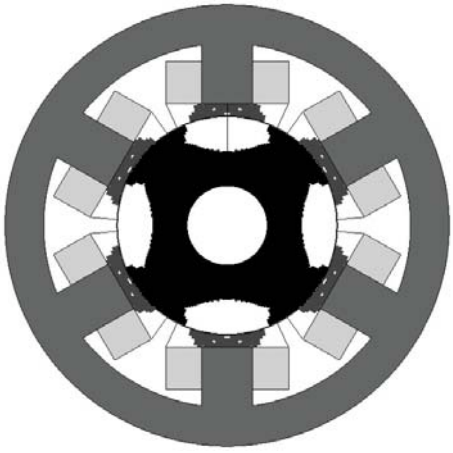

(c)

Figure 6.4.2. SRM Design Result

(a) typical shape, (b) optimized shape with linear material assumption, (c) optimized shape with saturated material

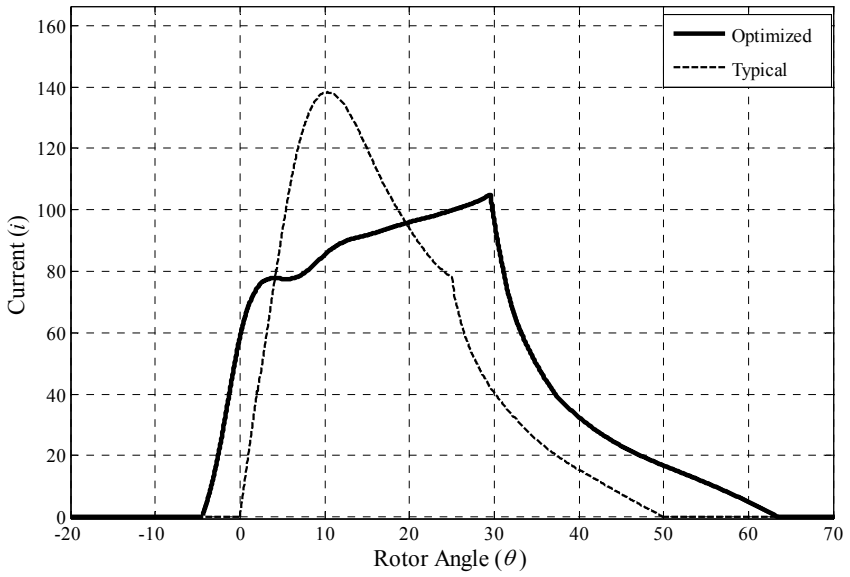

(a)

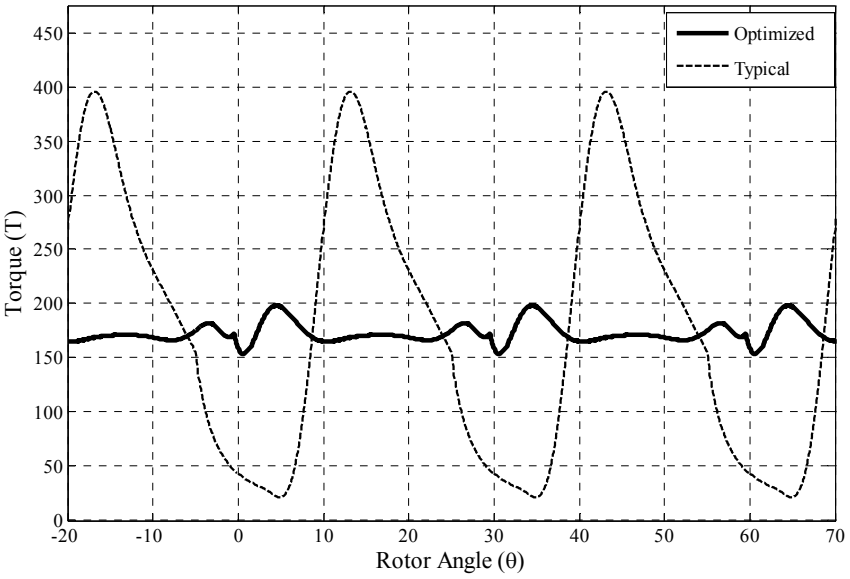

(b)

Figure 6.4.3. SRM performance of optimized and typical design
(a) Current curve, (b) Torque profile

6.5. Conclusion

Structural topology optimization of SRMs is presented in this paper. To perform the sensitivity analysis, the SRM performance analysis model using Fourier series expansions and piecewise quadratic polynomials is proposed. Based on this model, structural topology optimization of SRMs is carried out to minimize torque ripples with the constraints on the RMS value of the phase current. The optimized SRMs successfully satisfy the optimization objectives and constraints. The geometries of optimized nonlinear SRMs are compared with those of linear SRMs. In the future, an effort will be made to optimize three dimensional SRMs, and three dimensional effects in the analysis and design of SRMs also will be investigated.

CHAPTER 7
CONCLUSIONS AND FUTURE WORKS

7.1. Concluding remarks

In this dissertation, structural topology optimization in magnetic field is extensively investigated to improve the force/torque performance of magnetic devices. First, the finite element method for the magnetostatic analysis is presented to calculate magnetic field in a structure including complex geometries. From the obtained magnetic field, the magnetic force/torque can be calculated using various kinds of magnetic force calculation methods. Based on the analysis to obtain the magnetic field and magnetic force, the structural topology optimization is applied for the design of magnetic devices. First, the magnetic actuator is designed to investigate the characteristics of magnetic circuit parameters. Then the structural topology optimization in the coupled magneto-structural problem is presented. Finally, switched reluctance motors are designed to improve the torque performance in a steady-state operation.

Finite element method for magnetostatic analysis

The magnetostatic equation is derived from the Maxwell's equation and solved using the finite element method with vector potential. A gauge condition to solve the uniqueness problem is investigated, and it is concluded that a gauge condition is automatically satisfied in two dimensional problems and it is unnecessary to impose a gauge condition in three dimensional problems if the magnetic flux density **B** is the quantity of primary interest. The characteristics of nodal and edge elements in three dimensional problems are explained in the aspect of two boundary conditions at the interface of different materials. The Newton-Raphson iteration method to solve the non-linear problem considering the magnetic saturation is described in detail. A finite element program is developed to solve the 2D/3D linear/non-linear magnetostatic problems. The developed program is verified by comparing the analysis results with those using COMSOL and ANSYS. The results confirm that the finite element method gives reasonable magnetic fields over the whole domain, but the nodal element may fail to calculate accurate magnetic fields at the interface of different materials.

Magnetic force calculation

Various magnetic force calculation methods are comprehensively investigated. The methods can be classified into convectional method and body force calculation methods. Conventional methods such as the Maxwell stress tensor method, virtual work method, and equivalent source method, give the surface force distribution. In contrast, a rather new method, that is, the body force calculation method, provides the force distribution on the whole body. The derivation of each method is briefly described for both linear and

non-linear problems, and all methods are applied to the magnetic force calculation acting on the armature of the magnetic actuator. The calculation results show that global magnetic force is unique regardless of the force calculation methods although the equivalent current method fails to give a unique global force. The body force calculation methods provide exactly identical global forces as those using corresponding conventional methods. The conventional methods fail to provide the unique force distribution, while the body force calculation methods give a unique force distribution. These results definitely shows the validity of body force calculation methods, although we cannot conclude the debate about true magnetic force distribution.

Design of magnetic actuator and effect of magnetic circuit parameters

The structural topology optimization of a magnetic actuator is carried out for both linear and non-linear problems. The design goal is to maximize the magnetic force applied on the armature, and the magnetic force is calculated using the Maxwell stress tensor method and the local virtual work method. Optimization results with three different permeability models and different volumes are presented, and then the effect of permeability and design domain volume is investigated. In the results, the nonlinearity makes the optimized structure concentrated and simple because this structure can weaken the magnetic saturation effect which deteriorates the magnetic force. The effect of volume appears differently in linear and non-linear cases. In the linear case, the decreased volume slightly affects the magnetic force. In contrast, decreased volume in the non-linear case largely deteriorates the magnetic force because the magnetic saturation becomes strong in a small volume.

Structural topology optimization in coupled magneto-structural problem

The structural topology optimization is applied to the coupled magneto-structural problem. The design goals are to maximize total magnetic force and to minimize the mechanical deformation caused by the distributed magnetic force. The magnetic force is calculated as the distributed body force using the virtual air-gap scheme. As a design example, the armature of the solenoid actuator is optimized using the proposed approach. For the comparison, the same optimization is carried out using the Coulomb virtual work method for the calculation of magnetic force distribution. The optimization result using the proposed approach contains rather complex structures, while that using the Coulomb virtual work method is composed of simple and concentrated structures. The total forces of the two results are almost identical, and both results seem to maximize the total force successfully. However, the compliances of the two results are entirely different due to different force distributions. The proposed approach is more appropriate than that using the Coulomb virtual work method for structural topology optimization. It is known that the Coulomb virtual work method gives an inaccurate force distribution where the different materials are in contact. The design domain during optimization can be considered as a composition of different materials. Therefore, the compliance minimization using the Coulomb virtual work method might use an inaccurate force distribution. In contrast, the body force calculation method is proposed to calculate the accurate magnetic force calculation at the interface of different materials, and consequently, the compliance minimization can be performed using accurate force distribution.

Design of switched reluctance motors

Switched reluctance motors are designed using the structural topology optimization. The design goal is to minimize torque ripple, which is one of main issues with this motor. The copper loss is controlled as well by constraining the RMS value of the phase current. The design domains are chosen as both the geometric and electric domain: the rotor/stator of the motor and the voltage on-off angles respectively. To perform optimization using the mathematical programming method, the explicit representation of torque and current curve is obtained by the mathematical model of magnetic characteristics. In the linear problem, the inductance curve is approximated using Fourier series. In the non-linear problem, the flux linkage surface is approximated using Fourier series expansions and piecewise quadratic polynomials. Then, the current curve is calculated by solving the circuit equation, and the torque profile is obtained from the global virtual work method. Finally, analytical sensitivity analysis of the torque and current curve is performed, and the sequential linear programming method is used to solve the optimization problem. In the optimization result of the linear problem, holes are created to minimize the mass, while holes are not created in the result of the non-linear problem. Holes in the non-linear problem deteriorate the torque performance because magnetic saturation interrupts the flow of magnetic field around a narrowed path due to holes. The optimization results show that a notched rotor pole near airgap is the optimal shape to minimize torque ripple in both linear and non-linear problems.

7.2. Future works

This dissertation first reviewed the magnetostatic finite element analysis and magnetic calculation methods for accurate calculation of magnetic fields and magnetic forces. Then, the solenoid actuator and switched reluctance motors were designed using structural topology optimization to improve their force/torque performance. In addition to the above works, the author would like to suggest the following future works

Finite element analysis for eddy current and hysteresis

The dissertation did not treat the effects of eddy current and hysteresis. These effects can influence motor performance, particularly in induction motors. Therefore, study on these two effects might be critical for analyzing electric motors.

In order to take the eddy current effect into consideration, the Maxwell's equations with the vector potential method becomes

$$\nabla \times \left(\frac{1}{\mu} \nabla \times \mathbf{A} \right) = \mathbf{J} - \sigma \frac{\partial \mathbf{A}}{\partial t} \tag{7.2.1}$$

If current density **J** represents time harmonic excitation with frequency ω, Eq. (7.2.1) can be modified into the frequency domain equation:

$$\nabla \times \left(\frac{1}{\mu} \nabla \times \tilde{\mathbf{A}} \right) = \tilde{\mathbf{J}} - j\omega\sigma \tilde{\mathbf{A}} \tag{7.2.2}$$

The finite element method can be applied to solve Eq. (7.2.1) or (7.2.2), and then we can obtain the magnetic field taking the eddy current effect into consideration.

The hysteresis effect appears in most magnetic materials. This effect is a kind of 'memory' effect; some magnetic field remains even after external input is removed. Figure 7.2.1 shows the **B-H** relation when hysteresis is considered. The **B-H** relation should show the irreversible behavior and frequency dependency. Many **B-H** relation models such as Preisach model and Jiles-Atherton model, have been developed to represent the hysteresis effect. Studying the characteristics of each model with finite element analysis will be a valuable contribution to electric motor analysis.

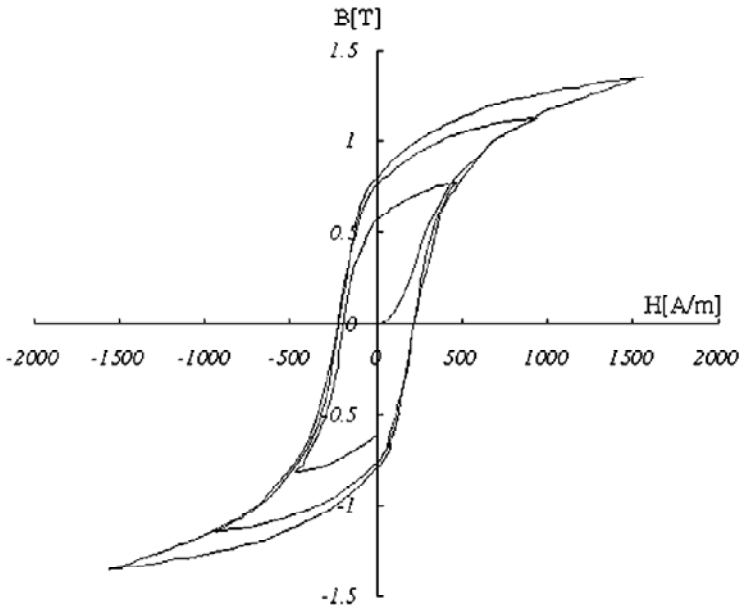

Figure 7.2.1. Hysteresis loop [153]

Topology optimization for experiment to validate body force calculation method

This dissertation investigates both surface and body local force calculation methods. Two methods give completely different local force distributions, but only one of them can be a true force distribution. The debate about which is true might be concluded by experimental validation. In [115], an experiment was performed to compare the deformation of four different force formulations using only the surface force method. This experiment can be extended to compare the deformation of surface and body force methods. Because the global force of two methods is exactly the same, the deformation of two methods can be nearly the same. To maximize the difference in the deformation of the two methods, we can use a shape designed using topology optimization. The optimization problem is briefly described in Figure 7.2.2. From this proposed experiment using the optimal shape, we might clearly resolve the debate about a true local force.

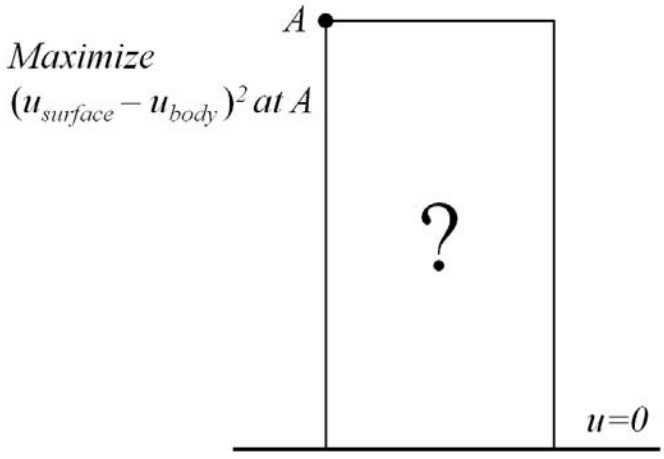

Figure 7.2.2. Topology optimization to design a experiment to find a true local force distribution between surface and body force method

Topology optimization to minimize the core loss of electric motors

In electric motors, losses create not only thermal problems but also inefficiencies. Two main losses in electric motors are core and copper loss. Copper loss is treated in this dissertation; core loss is not considered here. Topology optimization to minimize core loss can be a meaningful future work. Core loss is composed of eddy current loss and hysteresis loss. When the flux density **B** is sinusoidal, core loss is commonly expressed as

$$W_{core} = \sum_i k_e f_i^2 B_i^2 + k_h f_i B_i^{a+bB} \tag{7.2.3}$$

where f is the frequency of the flux density. k_e, k_h a, and b are the material constants [154]. The first term of Eq. (7.2.3) represents the hysteresis loss, and the second term represents the eddy current loss. To minimize core loss, optimization might seek to find a shape that minimizes the frequency f of magnetic flux density variation. The flux density itself might not be decreased for the force/torque performance.

BIBLIOGRAPHY

[1] D. Zobas, *Electric machines: principles, applications, and control*. St. Paul, MN: West publishing company, 1989.

[2] D. Carney, "Motors play important EV roles," in *automotive engineering*. vol. 116 SAE international, 2008, pp. 20-23.

[3] G. Yimin, M. Ehsani, and J. M. Miller, "Hybrid Electric Vehicle: Overview and State of the Art," in *Industrial Electronics, 2005. ISIE 2005. Proceedings of the IEEE International Symposium on*, 2005, pp. 307-316.

[4] M. P. Bendsoe and N. Kikuchi, "Generating optimal topologies in structural design using a homogenization method," *Computer Methods in Applied Mechanics and Engineering,* vol. 71, p. 197, 1988.

[5] J. Yoo, "Structural optimization in magnetic fields using the homogenization design method," in *Mechanical engineering*. vol. Ph. D. Ann Arbor: University of Michigan, 1999, p. 168.

[6] G. Kiziltas, "Dielectric material optimization of filters and antennas using SIMP," in *Mechanical engineering*. vol. Ph. D. Ann Arbor: Univerisity of Michigan, 2003, p. 205.

[7] Y. Jeonghoon and K. Noboru, "Topology optimization in magnetic fields using the homogenization design method," *International Journal for Numerical Methods in Engineering,* vol. 48, pp. 1463-1479, 2000.

[8] Y. Jeonghoon and N. Kikuchi, "Topology optimization for reduction of vibration caused by magnetic harmonic excitation," *Magnetics, IEEE Transactions on,* vol. 38, pp. 3643-3649, 2002.

[9] J. Yoo and H. Hong, "A modified density approach for topology optimization in magnetic fields," *International Journal of Solids and Structures,* vol. 41, p. 2461, 2004.

[10] J. S. Choi and J. Yoo, "Structural optimization of ferromagnetic materials based on the magnetic reluctivity for magnetic field problems," *Computer Methods in Applied Mechanics and Engineering,* vol. 197, pp. 4193-4206, 2008.

[11] J. Yoo and H. J. Soh, "An optimal design of magnetic actuators using topology optimization and the response surface method," *Microsystem Technologies,* vol. 11, pp. 1252-1261, 2005.

[12] P. Sang-In and M. Seungjae, "Magnetic Actuator Design for Maximizing Force Using Level Set Based Topology Optimization," *Magnetics, IEEE Transactions on,* vol. 45, pp. 2336-2339, 2009.

[13] C. Jae Seok and Y. Jeonghoon, "Structural Topology Optimization of Magnetic Actuators Using Genetic Algorithms and ON/OFF Sensitivity," *Magnetics, IEEE Transactions on,* vol. 45, pp. 2276-2279, 2009.

[14] P. Soonok, Y. Jeonghoon, and C. Jae Seok, "Optimal Shape Design of the Perpendicular Magnetic Recording Head," *Magnetics, IEEE Transactions on,* vol. 45, pp. 2272-2275, 2009.

[15] P. Soonok, Y. Jeonghoon, and C. Jae Seok, "Simultaneous Optimal Design of the Yoke and the Coil in the Perpendicular Magnetic Recording Head," *Magnetics, IEEE Transactions on,* vol. 45, pp. 3668-3671, 2009.

[16] S. Wang and J. Kang, "Topology optimization of nonlinear magnetostatics," *Magnetics, IEEE Transactions on,* vol. 38, pp. 1029-1032, 2002.

[17] S. Hokyung, M. Heegon, W. Semyung, and K. Hameyer, "Topology Optimization for Compliance Reduction of Magnetomechanical Systems," *Magnetics, IEEE Transactions on,* vol. 44, p. 346, 2008.

[18] H. Shim, S. Wang, and K. Hameyer, "Topology Optimization of Magnetothermal Systems Considering Eddy Current as Joule Heat," *Magnetics, IEEE Transactions on,* vol. 43, p. 1617, 2007.

[19] S. Hokyung, H. Vinh Thuy Tran, W. Semyung, and D. A. Tortorelli, "Level Set-Based Topology Optimization for Electromagnetic Systems," *Magnetics, IEEE Transactions on,* vol. 45, pp. 1582-1585, 2009.

[20] W. Semyung, K. Jenam, and N. Jeongchae, "Topology optimization of a single-phase induction motor for rotary compressor," *Magnetics, IEEE Transactions on,* vol. 40, pp. 1591-1596, 2004.

[21] S. Hokyung, W. Semyung, and L. Kwansoo, "3-D Optimal Design of Induction Motor Used in High-Pressure Scroll Compressor," *Magnetics, IEEE Transactions on,* vol. 45, pp. 2076-2084, 2009.

[22] O. Yoshifumi and T. Norio, "Investigation of topology optimization of magnetic circuit using density method," *Electrical Engineering in Japan,* vol. 155, pp. 53-63, 2006.

[23] K. Woochul and K. Yoon Young, "Stacked-Element Connectivity Parameterization for Topology Optimization of Nonlinear Magnetic Systems," *Magnetics, IEEE Transactions on,* vol. 44, pp. 4754-4763, 2008.

[24] W. Kim, J. E. Kim, and Y. Y. Kim, "Coil configuration design for the Lorentz force maximization by the topology optimization method: applications to optical pickup coil design," *Sensors and Actuators A: Physical,* vol. 121, pp. 221-229, 2005.

[25] K. Woochul and K. Yoon Young, "Design of a bias magnetic system of a magnetostrictive sensor for flexural wave measurement," *Magnetics, IEEE Transactions on,* vol. 40, pp. 3331-3338, 2004.

[26] W. Kim and Y. Kim, "Magnetic circuit design by topology optimization for Lorentz force maximization in a microspeaker," *Journal of Mechanical Science and Technology,* vol. 22, pp. 1699-1706, 2008.

[27] Y. Okamoto, M. Ohtake, and N. Takahashi, "Magnetic shield design of perpendicular magnetic recording head by using topology optimization technique," *Magnetics, IEEE Transactions on,* vol. 41, pp. 1788-1791, 2005.

[28] Y. Okamoto, K. Akiyama, and N. Takahashi, "3-D topology optimization of single-pole-type head by using design sensitivity analysis," *Magnetics, IEEE Transactions on,* vol. 42, pp. 1087-1090, 2006.

[29] P. J. Lawrenson, J. M. Stephenson, N. N. Fulton, P. T. Blenkinsop, and J. Corda, "Variable-speed switched reluctance motors," *Electric Power Applications, IEE Proceedings B,* vol. 127, pp. 253-265, 1980.

[30] R. Arumugam, D. Lowther, R. Krishnan, and J. Lindsay, "Magnetic field analysis of a switched reluctance motor using a two dimensional finite element model," *Magnetics, IEEE Transactions on,* vol. 21, pp. 1883-1885, 1985.

[31] J. F. Lindsay, R. Arumugam, and R. Krishnan, "Finite-element analysis characterisation of a switched reluctance motor with multitooth per stator pole," *Electric Power Applications, IEE Proceedings B,* vol. 133, pp. 347-353, 1986.

[32] B. Parreira, S. Rafael, A. J. Pires, and P. J. C. Branco, "Obtaining the magnetic characteristics of an 8/6 switched reluctance machine: from FEM analysis to the experimental tests," *Industrial Electronics, IEEE Transactions on,* vol. 52, pp. 1635-1643, 2005.

[33] J. C. Moreira, "Torque ripple minimization in switched reluctance motors via bi-cubic spline interpolation," in *Power Electronics Specialists Conference, 1992. PESC '92 Record., 23rd Annual IEEE*, 1992, pp. 851-856 vol.2.

[34] S. Khotpanya, S. Kittiratsatcha, and I. Kazuhisa, "A Magnetic Model of a Three-Phase Switched-Reluctance Machine using Cubic Spline Interpolation Technique," in *Power Electronics and Drives Systems, 2005. PEDS 2005. International Conference on*, 2005, pp. 1167-1170.

[35] S. Cao and K. J. Tseng, "A new method for accurate analytical modeling of switched reluctance motor," in *Power Electronic Drives and Energy Systems for Industrial Growth, 1998. Proceedings. 1998 International Conference on*, 1998, pp. 540-545 Vol. 2.

[36] H. P. Chi, R. L. Lin, and J. F. Chen, "Simplified flux-linkage model for switched-reluctance motors," *Electric Power Applications, IEE Proceedings -,* vol. 152, pp. 577-583, 2005.

[37] Z. Huijun, D. Wen, and Y. Zhenmin, "A nonlinear model for the switched reluctance motor," in *Electrical Machines and Systems, 2005. ICEMS 2005. Proceedings of the Eighth International Conference on*, 2005, pp. 568-571 Vol. 1.

[38] B. Fahimi, G. Suresh, J. Mahdavi, and M. Ehsami, "A new approach to model switched reluctance motor drive application to dynamic performance prediction,

control and design," in *Power Electronics Specialists Conference, 1998. PESC 98 Record. 29th Annual IEEE*, 1998, pp. 2097-2102 vol.2.

[39] D. A. Andrade and R. Krishnan, "Characterization of switched reluctance machines using Fourier series approach," in *Industry Applications Conference, 2001. Thirty-Sixth IAS Annual Meeting. Conference Record of the 2001 IEEE*, 2001, pp. 48-54 vol.1.

[40] A. Khalil and I. Husain, "A Fourier Series Generalized Geometry-Based Analytical Model of Switched Reluctance Machines," *Industry Applications, IEEE Transactions on,* vol. 43, pp. 673-684, 2007.

[41] X. D. Xue, K. W. E. Cheng, S. L. Ho, and K. F. Kwok, "Trigonometry-Based Numerical Method to Compute Nonlinear Magnetic Characteristics in Switched Reluctance Motors," *Magnetics, IEEE Transactions on,* vol. 43, pp. 1845-1848, 2007.

[42] V. Tkachuk and M. Klytta, "Switched Reluctance Motor and its Mathematical Model," in *Compatibility in Power Electronics, 2007. CPE '07*, 2007, pp. 1-5.

[43] P. N. Materu and R. Krishnan, "Steady-state analysis of the variable-speed switched-reluctance motor drive," *Industrial Electronics, IEEE Transactions on,* vol. 36, pp. 523-529, 1989.

[44] M. Cundev and L. Petkovska, "Transient analysis of a switched reluctance motor based on 3D finite element method," in *Electrical Machines and Systems, 2003. ICEMS 2003. Sixth International Conference on*, 2003, pp. 765-768 vol.2.

[45] K. N. Srinivas and R. Arumugam, "Analysis and characterization of switched reluctance motors: Part I /sub y/namic, static, and frequency spectrum analyses," *Magnetics, IEEE Transactions on,* vol. 41, p. 1306, 2005.

[46] M. Semsudin, C. Jasmin, and S. Senad, "Computation of static, steady-state and dynamic characteristics of the switched reluctance motor," *Automatika* vol. 43, pp. 109-117, 2002.

[47] D. E. Cameron, J. H. Lang, and S. D. Umans, "The origin and reduction of acoustic noise in doubly salient variable-reluctance motors," *Industry Applications, IEEE Transactions on,* vol. 28, pp. 1250-1255, 1992.

[48] C. Y. Wu and C. Pollock, "Analysis and reduction of vibration and acoustic noise in the switched reluctance drive," in *Industry Applications Society Annual Meeting, 1993., Conference Record of the 1993 IEEE*, 1993, pp. 106-113 vol.1.

[49] L. Joon-Ho, L. Young-Hwan, K. Dong-Hun, L. Ki-Sik, and P. Il-Han, "Dynamic vibration analysis of switched reluctance motor using magnetic charge force density and mechanical analysis," *Applied Superconductivity, IEEE Transactions on,* vol. 12, pp. 1511-1514, 2002.

[50] K. N. Srinivas and R. Arumugam, "Analysis and characterization of switched reluctance motors: Part II. Flow, thermal, and vibration analyses," *Magnetics, IEEE Transactions on,* vol. 41, p. 1321, 2005.

[51] S. Jianbo, Z. Qionghua, W. Shuanghong, and M. Zhiyuan, "A Novel Radiating Rib Structure in Switched Reluctance Motors for Low Acoustic Noise," *Magnetics, IEEE Transactions on,* vol. 43, pp. 3630-3637, 2007.

[52] P. N. Materu and R. Krishnan, "Estimation of switched reluctance motor losses," *Industry Applications, IEEE Transactions on,* vol. 28, pp. 668-679, 1992.

[53] J. Boivie, "Iron loss model and measurements of the losses in a switched reluctance motor," in *Electrical Machines and Drives, 1993. Sixth International Conference on (Conf. Publ. No. 376)*, 1993, pp. 219-222.

[54] J. Faiz, B. Ganji, C. E. Carstensen, and R. W. D. Doncker, "Loss prediction in switched reluctance motors using finite element method," *European Transactions on Electrical Power,* vol. 19, pp. 731-748, 2009.

[55] V. Raulin, A. Radun, and I. Husain, "Modeling of losses in switched reluctance machines," *Industry Applications, IEEE Transactions on,* vol. 40, pp. 1560-1569, 2004.

[56] J. T. Charton, J. Corda, A. Hughes, J. M. Stephenson, and M. L. McClelland, "Modelling and prediction of iron loss with complex flux waveforms," *Electric Power Applications, IEE Proceedings -,* vol. 152, pp. 862-870, 2005.

[57] I. Shingo, T. Sakai, and K. Sawa, "A temperature rise analysis of switched reluctance motor due to the core and copper loss by FEM," *Magnetics, IEEE Transactions on,* vol. 39, pp. 1554-1557, 2003.

[58] J. Faiz, B. Ganji, C. E. Carstensen, K. A. Kasper, and R. W. De Doncker, "Temperature Rise Analysis of Switched Reluctance Motors Due to Electromagnetic Losses," *Magnetics, IEEE Transactions on,* vol. 45, pp. 2927-2934, 2009.

[59] K. Ohyama, M. N. F. Nashed, K. Aso, H. Fujii, and H. Uehara, "Design using Finite Element Analysis of Switched Reluctance Motor for Electric Vehicle," in *Information and Communication Technologies, 2006. ICTTA '06. 2nd*, 2006, p. 727.

[60] W. Wu, H. C. Lovatt, and J. B. Dunlop, "Optimisation of switched reluctance motors for hybrid electric vehicles," in *Power Electronics, Machines and Drives, 2002. International Conference on (Conf. Publ. No. 487)*, 2002, pp. 177-182.

[61] K. M. Rahman and S. E. Schulz, "Design of high efficiency and high density switched reluctance motor for vehicle propulsion," in *Industry Applications Conference, 2001. Thirty-Sixth IAS Annual Meeting. Conference Record of the 2001 IEEE*, 2001, pp. 2104-2110 vol.3.

[62] K. Nakamura, Y. Suzuki, H. Goto, and O. Ichinokura, "Design of outer-rotor type multipolar SR motor for electric vehicle," *Journal of Magnetism and Magnetic Materials,* vol. 290-291, pp. 1334-1337, 2005.

[63] K. Koibuchi, T. Ohno, and K. Sawa, "A basic study for optimal design of switched reluctance motor by finite element method," *Magnetics, IEEE Transactions on,* vol. 33, pp. 2077-2080, 1997.

[64] R. Arumugam, J. F. Lindsay, and R. Krishnan, "Sensitivity of pole arc/pole pitch ratio on switched reluctance motor performance," in *Industry Applications Society Annual Meeting, 1988., Conference Record of the 1988 IEEE*, 1988, pp. 50-54 vol.1.

[65] Y. Ohdachi, Y. Kawase, Y. Miura, and Y. Hayashi, "Optimum design of switched reluctance motors using dynamic finite element analysis," *Magnetics, IEEE Transactions on,* vol. 33, pp. 2033-2036, 1997.

[66] W. Wei, J. B. Dunlop, S. J. Collocott, and B. A. Kalan, "Design optimization of a switched reluctance motor by electromagnetic and thermal finite-element analysis," *Magnetics, IEEE Transactions on,* vol. 39, pp. 3334-3336, 2003.

[67] C. Jae-Hak, K. Sol, S. Jeong-Min, L. Ju, and K. Suk-Tae, "The multi-object optimization of switched reluctance motor," in *Electrical Machines and Systems, 2003. ICEMS 2003. Sixth International Conference on*, 2003, pp. 195-198 vol.1.

[68] F. Sahin, H. B. Ertan, and K. Leblebicioglu, "Optimum geometry for torque ripple minimization of switched reluctance motors," *Energy Conversion, IEEE Transaction on,* vol. 15, p. 30, 2000.

[69] S. Brisset and P. Brochet, "Optimization of switched reluctance motors using deterministic methods with static and dynamic finite element simulations," *Magnetics, IEEE Transactions on,* vol. 34, pp. 2853-2856, 1998.

[70] Y. K. Choi, H. S. Yoon, and C. S. Koh, "Pole-Shape Optimization of a Switched-Reluctance Motor for Torque Ripple Reduction," *Magnetics, IEEE Transactions on,* vol. 43, p. 1797, 2007.

[71] S. I. Nabeta, I. E. Chabu, L. Lebensztajn, D. A. P. Correa, W. M. da Silva, and K. Hameyer, "Mitigation of the Torque Ripple of a Switched Reluctance Motor Through a Multiobjective Optimization," *Magnetics, IEEE Transactions on,* vol. 44, p. 1018, 2008.

[72] L. Jin Woo, K. Hong Seok, K. Byung Il, and K. Byung Taek, "New rotor shape design for minimum torque ripple of SRM using FEM," *Magnetics, IEEE Transactions on,* vol. 40, pp. 754-757, 2004.

[73] M. T. Khor and R. Sotudeh, "A 3-phase 12/10 asymmetrical switched reluctance motor," in *Power Electronics and Applications, 2005 European Conference on*, 2005, pp. 9 pp.-P.9.

[74] C. Sei and M. N. Hamid, "Finite-element study on a two-phase switched-reluctance motor with split rotor poles," in *Power Electronics and Drives Systems, 2005. PEDS 2005. International Conference on*, 2005, pp. 1156-1160.

[75] N. Vattikuti, V. Rallabandi, and B. G. Fernandes, "A novel high torque and low weight segmented switched reluctance motor," in *Power Electronics Specialists Conference, 2008. PESC 2008. IEEE*, 2008, pp. 1223-1228.

[76] J. K. Byun and S. Y. Hahn, "Topology optimization of switched reluctance motor using mutual energy method," *International Journal Of Applied Electromagnetics And Mechanics,* vol. 13, pp. 421-426, 2001.

[77] J. Yoo, "Reduction of vibration caused by magnetic force in a switched reluctance motor by topology optimization," *Journal Of Applied Mechanics-Transactions Of The Asme,* vol. 69, pp. 380-387, May 2002.

[78] J. P. A. Bastros and N. Sadowski, *Electromagnetic modeling by finite element ethods*: Marcel Dekker, 2003.

[79] M. V. K. Chari and S. J. Salon, *Numerical methods in electromagnetism*: Academic Press, 2000.

[80] D. J. Griffiths, *Introduction to electrodynamics*, 3rd ed.: Prentice_hall, 1999.

[81] S. Ratnajeevan and H. Hoole, *Finite elements, electromagnetics and design*: Elsevier, 1995.

[82] N. Bianchi, *Electrical machine analysis using finite elements*: CRC Press, 2005.

[83] J. Jin, *The finite element method in electromagnetics*: John Wiley & Sons, 2002.

[84] J. L. Volakis, A. Chatterjee, and L. C. Kempel, *Finite element method for electromagnetics*: IEEE Press, Oxford University Press, 1998.

[85] "ANSYS, Inc. Theory Reference," ANSYS Release 9.0, 2004.

[86] O. Biro, K. Preis, G. Vrisk, K. R. Richter, and I. Ticar, "Computation of 3-D magnetostatic fields using a reduced scalar potential," *Magnetics, IEEE Transactions on,* vol. 29, pp. 1329-1332, 1993.

[87] J. P. Webb and B. Forghani, "A single scalar potential method for 3D magnetostatics using edge elements," *Magnetics, IEEE Transactions on,* vol. 25, pp. 4126-4128, 1989.

[88] K. Preis, I. Bardi, O. Biro, C. Magele, W. Renhart, K. R. Richter, and G. Vrisk, "Numerical analysis of 3D magnetostatic fields," *Magnetics, IEEE Transactions on,* vol. 27, pp. 3798-3803, 1991.

[89] M. Gyimesi and J. D. Lavers, "Generalized potential formulation for 3-D magnetostatic problems," *Magnetics, IEEE Transactions on,* vol. 28, pp. 1924-1929, 1992.

[90] G. Bedrosian, M. V. K. Chari, and J. Joseph, "Comparison of full and reduced potential formulations for low-frequency applications," *Magnetics, IEEE Transactions on,* vol. 29, pp. 1321-1324, 1993.

[91] I. Mayergoyz, M. Chari, and J. D'Angelo, "A new scalar potential formulation for three-dimensional magnetostatic problems," *Magnetics, IEEE Transactions on,* vol. 23, pp. 3889-3894, 1987.

[92] C. Magele, H. Stogner, and K. Preis, "Comparison of different finite element formulations for 3D magnetostatic problems," *Magnetics, IEEE Transactions on,* vol. 24, pp. 31-34, 1988.

[93] A. B. J. Reece and T. W. Preston, *Finite element methods in electrical power engineering*: Oxford University Press, 2000.

[94] J. Yoo, "Structural optimization in magnetic fields using the homogenization design method," in *Mechanical engineering*. vol. Ph. D. Ann Arbor: University of Michigan, 1999.

[95] O. C. Zienkiewicz and R. L. Taylor, *The finite element method*, 5th ed.: Butterworth-Heinemann, 2000.

[96] N. A. Demerdash and R. Wang, "Theoretical and numerical difficulties in 3D-Vector potential methods in finite element magnetostatic computations," in *Magnetics Conference, 1990. 1990 Digests of INTERMAG '90. International*, 1990, pp. BQ-09-BQ-09.

[97] O. Biro, K. Preis, and K. R. Richter, "On the use of the magnetic vector potential in the nodal and edge finite element analysis of 3D magnetostatic problems," *Magnetics, IEEE Transactions on,* vol. 32, pp. 651-654, 1996.

[98] P. O. Silvester and R. L. Ferrari, *Finite elements for electrical engineers*, 3rd ed.: Cambridge University Press, 1996.

[99] S. J. Salon, *Finite element analysis of electrical machines*: Kluwer Academic Publishers, 1995.

[100] J. B. Manges and Z. J. Cendes, "A generalized tree-cotree gauge for magnetic field computation," *Magnetics, IEEE Transactions on,* vol. 31, pp. 1342-1347, 1995.

[101] M. L. Barton and Z. J. Cendes, "New vector finite elements for three-dimensional magnetic field computation," *Journal of Applied Physics,* vol. 61, pp. 3919-3921, 1987.

[102] K. Preis, I. Bardi, O. Biro, C. Magele, G. Vrisk, and K. R. Richter, "Different finite element formulations of 3D magnetostatic fields," *Magnetics, IEEE Transactions on,* vol. 28, pp. 1056-1059, 1992.

[103] J. Brauer, "Simple equations for the magnetization and reluctivity curves of steel," *Magnetics, IEEE Transactions on,* vol. 11, pp. 81-81, 1975.

[104] K. Fujiwara, T. Nakata, N. Takahashi, and H. Ohashi, "On the continuity of the magnetizing current density in 3-D magnetic field analysis with edge element," *Magnetics, IEEE Transactions on,* vol. 31, pp. 1364-1367, 1995.

[105] E. A. Aronson and J. R. Brauer, "Magnetic torque or force calculation by direct differentiation of finite element coenergy," *Magnetics, IEEE Transactions on,* vol. 25, pp. 3578-3580, 1989.

[106] A. Benhama, A. C. Williamson, and A. B. J. Reece, "Force and torque computation from 2-D and 3-D finite element field solutions," *Electric Power Applications, IEE Proceedings -,* vol. 146, pp. 25-31, 1999.

[107] K. Komeza, A. Pelikant, J. Tegopoulos, and S. Wiak, "Comparative computation of forces and torques of electromagnetic devices by means of different formulae," *Magnetics, IEEE Transactions on,* vol. 30, pp. 3475-3478, 1994.

[108] M. Ito, F. Tajima, and H. Kanazawa, "Evaluation of force calculating methods," *Magnetics, IEEE Transactions on,* vol. 26, pp. 1035-1038, 1990.

[109] T. Tarnhuvud and K. Reichert, "Accuracy problems of force and torque calculation in FE-systems," *Magnetics, IEEE Transactions on,* vol. 24, pp. 443-446, 1988.

[110] Z. Ren, "Comparison of different force calculation methods in 3D finite element modelling," *Magnetics, IEEE Transactions on,* vol. 30, pp. 3471-3474, 1994.

[111] A. N. Wignall, A. J. Gilbert, and S. J. Yang, "Calculation of forces on magnetised ferrous cores using the Maxwell stress method," *Magnetics, IEEE Transactions on,* vol. 24, pp. 459-462, 1988.

[112] A. Hamler, B. Kreca, and B. Hribernik, "Investigation of the torque calculation of a DC PM motor," *Magnetics, IEEE Transactions on,* vol. 28, pp. 2271-2273, 1992.

[113] S. McFee and D. Lowther, "Towards accurate and consistent force calculation in finite element based computational magnetostatics," *Magnetics, IEEE Transactions on,* vol. 23, pp. 3771-3773, 1987.

[114] M. Moallem and C. M. Ong, "Predicting the torque of a switched reluctance machine from its finite element field solution," *Energy Conversion, IEEE Transactions on,* vol. 5, pp. 733-739, 1990.

[115] O. Barre, P. Brochet, and M. Hecquet, "Experimental validation of magnetic and electric local force formulations associated to energy principle," *Magnetics, IEEE Transactions on,* vol. 42, pp. 1475-1478, 2006.

[116] L. H. de Medeiros, G. Reyne, and G. Meunier, "A unique distribution of forces in permanent magnets using scalar and vector potential formulations," *Magnetics, IEEE Transactions on,* vol. 36, pp. 3345-3348, 2000.

[117] W. N. Fu, P. Zhou, D. Lin, S. Stanton, and Z. J. Cendes, "Magnetic force computation in permanent magnets using a local energy coordinate derivative method," *Magnetics, IEEE Transactions on,* vol. 40, pp. 683-686, 2004.

[118] A. Benhama, A. C. Williamson, and A. B. J. Reece, "Virtual work approach to the computation of magnetic force distribution from finite element field solutions," *Electric Power Applications, IEE Proceedings -,* vol. 147, pp. 437-442, 2000.

[119] I. Nishiguchi, A. Kameari, and K. Haseyama, "On the local force computation of deformable bodies in magnetic field," *Magnetics, IEEE Transactions on,* vol. 35, pp. 1650-1653, 1999.

[120] H.-s. Choi, I.-h. Park, and S.-H. Lee, "Electromagnetic body force calculation based on virtual air gap," 2006, pp. 08H903-3.

[121] C. Hong Soon, P. Il Han, and L. Se Hee, "Concept of virtual air gap and its applications for force calculation," *Magnetics, IEEE Transactions on,* vol. 42, pp. 663-666, 2006.

[122] C. Hong Soon, L. Se Hee, K. Young Sun, K. Kwang Tae, and P. Il Han, "Implementation of Virtual Work Principle in Virtual Air Gap," *Magnetics, IEEE Transactions on,* vol. 44, pp. 1286-1289, 2008.

[123] C. Hong Soon, P. Il Han, and L. Se Hee, "Generalized equivalent magnetizing current method for total force calculation of magnetized bodies in contact," *Magnetics, IEEE Transactions on,* vol. 42, pp. 531-534, 2006.

[124] C. Hong Soon, L. Se Hee, and P. Il Han, "General formulation of equivalent magnetic charge method for force density distribution on interface of different materials," *Magnetics, IEEE Transactions on,* vol. 41, pp. 1420-1423, 2005.

[125] C. Hong Soon, K. Young Sun, L. Joon Ho, and P. Il Han, "An Observation of Body Force Distributions in Electric Machines," *Magnetics, IEEE Transactions on,* vol. 43, pp. 1861-1864, 2007.

[126] J. Coulomb, "A methodology for the determination of global electromechanical quantities from a finite element analysis and its application to the evaluation of magnetic forces, torques and stiffness," *Magnetics, IEEE Transactions on,* vol. 19, pp. 2514-2519, 1983.

[127] N. Takahashi, S. Nakazaki, and D. Miyagi, "Examination of Optimal Design Method of Electromagnetic Shield Using ON/OFF Method," *Magnetics, IEEE Transactions on,* vol. 45, pp. 1546-1549, 2009.

[128] Y. Jeonghoon, Y. Seunjin, and C. Jae Seok, "Optimal Design of an Electromagnetic Coupler to Maximize Force to a Specific Direction," *Magnetics, IEEE Transactions on,* vol. 44, pp. 1737-1742, 2008.

[129] J. H. Seo, "Optimal design of material microstructure for convective heat transfer in a solid-fluid mixture," in *Mechanical Engineering*. vol. Doctor of Philosophy Ann Arbor: University of Michigan, 2009, p. 252.

[130] C. Jae-Hak, K. Tae Heoung, K. B. Jang, and L. Ju, "Geometric and electrical optimization design of SR motor based on progressive quadratic response surface method," *Magnetics, IEEE Transactions on,* vol. 39, p. 3241, 2003.

[131] M. P. Bendsøe and O. Sigmund, *Topology Optimization: Theory, Methods and Applications*: Springer, 2003.

[132] Y. Okamoto, M. Ohtake, and N. Takahashi, "Magnetic shield design of perpendicular magnetic recording head by using topology optimization technique," *Magnetics, IEEE Transactions on,* vol. 41, p. 1788, 2005.

[133] J. K. Byun and I. H. Park, "Design of Dielectric Waveguide Filters Using Topology Optimization Technique," *Magnetics, IEEE Transactions on,* vol. 43, p. 1573, 2007.

[134] Y. Jeonghoon, Y. Seunjin, and C. Jae Seok, "Optimal Design of an Electromagnetic Coupler to Maximize Force to a Specific Direction," *Magnetics, IEEE Transactions on,* vol. 44, p. 1737, 2008.

[135] S. Kyung Ho, C. Seung Hyun, and K. Yoon Young, "Topology Design Optimization of a Magnetostrictive Patch for Maximizing Elastic Wave Transduction in Waveguides," *Magnetics, IEEE Transactions on,* vol. 44, p. 2373, 2008.

[136] J. S. Arora, *Introduction to optimum design,* 2nd ed. Elsevier, 2004.

[137] D. A. Andrade and R. Krishnan, "Characterization of switched reluctance machines using Fourier series approach," in *Industry Applications Conference, 2001. Thirty-Sixth IAS Annual Meeting. Conference Record of the 2001 IEEE*, 2001, p. 48.

[138] A. Benhama, A. C. Williamson, and A. B. J. Reece, "Force and torque computation from 2-D and 3-D finite element field solutions," *Electric Power Applications, IEE Proceedings -,* vol. 146, p. 25, 1999.

[139] T. J. E. Miller, *Switched Reluctance Motors and Their Control,* Published jointly by Hillsboro, OH : Magna Physics Div., Tridelta Industries and New York:Oxford University press, 1993.

[140] B. Parreira, S. Rafael, A. J. Pires, and P. J. C. Branco, "Obtaining the magnetic characteristics of an 8/6 switched reluctance machine: from FEM analysis to the experimental tests," *Industrial Electronics, IEEE Transactions on,* vol. 52, p. 1635, 2005.

[141] R. Arumugam, D. Lowther, R. Krishnan, and J. Lindsay, "Magnetic field analysis of a switched reluctance motor using a two dimensional finite element model," *Magnetics, IEEE Transactions on,* vol. 21, p. 1883, 1985.

[142] J. S. Choi and J. Yoo, "Structural Optimization of a Magnetic Actuator Using a New Interpolation Scheme Based on Magnetic Reluctivity," *7th World Congress on Structural and Multidisciplinary Optimization,* Seoul, 2007.

[143] B. Jin-Kyu, H. Song-Yop, and P. Il-Han, "Topology optimization of electrical devices using mutual energy and sensitivity," *Magnetics, IEEE Transactions on,* vol. 35, p. 3718, 1999.

[144] T. Borrvall and J. Petersson, "Topology optimization using regularized intermediate density control," *Computer Methods in Applied Mechanics and Engineering,* vol. 190, p. 4911, 2001.

[145] O. Sigmund, "Morphology-based black and white filters for topology optimization," *Structural And Multidisciplinary Optimization,* vol. 33, pp. 401-424, Apr 2007.

[146] J. Petersson, "Some convergence results in perimeter-controlled topology optimization," *Computer Methods in Applied Mechanics and Engineering,* vol. 171, p. 123, 1999.

[147] K. K. Choi and N. H. Kim, *Structural Sensitivity Analysis and Optimization 1,* Springer, 2005.

[148] L. Jin Woo, K. Hong Seok, K. Byung Il, and K. Byung Taek, "New rotor shape design for minimum torque ripple of SRM using FEM," *Magnetics, IEEE Transactions on,* vol. 40, p. 754, 2004.

[149] P. Pillay and W. Cai, "An investigation into vibration in switched reluctance motors," *Industry Applications, IEEE Transactions on,* vol. 35, p. 589, 1999.

[150] L. Joon-Ho, L. Young-Hwan, K. Dong-Hun, L. Ki-Sik, and P. Il-Han, "Dynamic vibration analysis of switched reluctance motor using magnetic charge force density and mechanical analysis," *Applied Superconductivity, IEEE Transactions on,* vol. 12, p. 1511, 2002.

[151] Y. Tang, "Characterization, numerical analysis, and design of switched reluctance motors," *Industry Applications, IEEE Transactions on,* vol. 33, p. 1544, 1997.

[152] I. Shingo, T. Sakai, and K. Sawa, "A temperature rise analysis of switched reluctance motor due to the core and copper loss by FEM," *Magnetics, IEEE Transactions on,* vol. 39, p. 1554, 2003.

[153] K. Hong-Kyu, H. Sun-Ki, and J. Hyun-Kyo, "An improved finite element analysis of magnetic system considering magnetic hysteresis," *Magnetics, IEEE Transactions on,* vol. 36, pp. 689-692, 2000.

[154] N. Hyuk, H. Kyung-Ho, L. Jeong-Jong, H. Jung-Pyo, and K. Gyu-Hong, "A study on iron loss analysis method considering the harmonics of the flux density waveform using iron loss curves tested on Epstein samples," *Magnetics, IEEE Transactions on,* vol. 39, pp. 1472-1475, 2003.